Mechanical design of soft viscoelastic adhesive interfaces via physics-guided data-driven modeling

The doctoral scholarship was supported by the European Union (ERC-2021-STG, "Towards Future Interfaces With Tuneable Adhesion By Dynamic Excitation" - SURFACE, Project ID: 101039198, CUP: D95F22000430006).

Department of Mechanics, Mathematics and Management
MECHANICAL AND MANAGEMENT ENGINEERING

Ph.D. Program

SSD: IIND-03/A Mechanical Design and Machine Construction

Final Dissertation

Mechanical Design of Soft Viscoelastic Adhesive Interfaces via Physics-Guided Data-Driven Modeling

by

ALI MAGHAMI

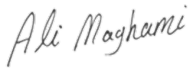

Referees:

Prof. Norbert Hoffmann

Prof. Francesc Pérez -Ràfols

Supervisors:

Prof. Antonio Papangelo

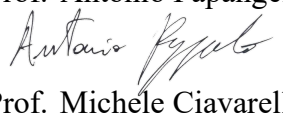

Prof. Michele Ciavarella

Prof. Merten Stender

Coordinator of Ph.D Program
Prof. Giuseppe Casalino

Course no. 38, 01/04/2023-31/03/2026

LIBERATORIA PER L'ARCHIVIAZIONE DELLA TESI DI DOTTORATO

Al Magnifico Rettore
del Politecnico di Bari

Il sottoscritto ALI MAGHAMI nato a MASHHAD, IRAN il 11.02.1988.
residente a Giovinazzo in via Papa Giovanni XXIII, 71/2 e-mail: a.maghami@phd.poliba.it
iscritto al 3° anno di Corso di Dottorato di Ricerca in Mechanical and Management Engineering ciclo 38
ed essendo stato ammesso a sostenere l'esame finale con la prevista discussione della tesi dal titolo:
Mechanical Design of Soft Viscoelastic Adhesive Interfaces via Physics-Guided Data-Driven Modeling

DICHIARA

1) di essere consapevole che, ai sensi del D.P.R. n. 445 del 28.12.2000, le dichiarazioni mendaci, la falsità negli atti e l'uso di atti falsi sono puniti ai sensi del codice penale e delle Leggi speciali in materia, e che nel caso ricorressero dette ipotesi, decade fin dall'inizio e senza necessità di nessuna formalità dai benefici conseguenti al provvedimento emanato sulla base di tali dichiarazioni;
2) di essere iscritto al Corso di Dottorato di ricerca Mechanical and Management Engineering ciclo 38, corso attivato ai sensi del "*Regolamento dei Corsi di Dottorato di ricerca del Politecnico di Bari"*, emanato con D.R. n.286 del 01.07.2013;
3) di essere pienamente a conoscenza delle disposizioni contenute nel predetto Regolamento in merito alla procedura di deposito, pubblicazione e autoarchiviazione della tesi di dottorato nell'Archivio Istituzionale ad accesso aperto alla letteratura scientifica;
4) di essere consapevole che attraverso l'autoarchiviazione delle tesi nell'Archivio Istituzionale ad accesso aperto alla letteratura scientifica del Politecnico di Bari (IRIS-POLIBA), l'Ateneo archivierà e renderà consultabile in rete (nel rispetto della Policy di Ateneo di cui al D.R. 642 del 13.11.2015) il testo completo della tesi di dottorato, fatta salva la possibilità di sottoscrizione di apposite licenze per le relative condizioni di utilizzo (di cui al sito http://www.creativecommons.it/Licenze), e fatte salve, altresì, le eventuali esigenze di "embargo", legate a strette considerazioni sulla tutelabilità e sfruttamento industriale/commerciale dei contenuti della tesi, da rappresentarsi mediante compilazione e sottoscrizione del modulo in calce (Richiesta di embargo);
5) che la tesi da depositare in IRIS-POLIBA, in formato digitale (PDF/A) sarà del tutto identica a quelle **consegnate**/inviate/da inviarsi ai componenti della commissione per l'esame finale e a qualsiasi altra copia depositata presso gli Uffici del Politecnico di Bari in forma cartacea o digitale, ovvero a quella da discutere in sede di esame finale, a quella da depositare, a cura dell'Ateneo, presso le Biblioteche Nazionali Centrali di Roma e Firenze e presso tutti gli Uffici competenti per legge al momento del deposito stesso, e che di conseguenza va esclusa qualsiasi responsabilità del Politecnico di Bari per quanto riguarda eventuali errori, imprecisioni o omissioni nei contenuti della tesi;
6) che il contenuto e l'organizzazione della tesi è opera originale realizzata dal sottoscritto e non compromette in alcun modo i diritti di terzi, ivi compresi quelli relativi alla sicurezza dei dati personali; che pertanto il Politecnico di Bari ed i suoi funzionari sono in ogni caso esenti da responsabilità di qualsivoglia natura: civile, amministrativa e penale e saranno dal sottoscritto tenuti indenni da qualsiasi richiesta o rivendicazione da parte di terzi;
7) che il contenuto della tesi non infrange in alcun modo il diritto d'Autore né gli obblighi connessi alla salvaguardia di diritti morali od economici di altri autori o di altri aventi diritto, sia per testi, immagini, foto, tabelle, o altre parti di cui la tesi è composta.

Luogo e data 15.05.2026 Bari

Ali Maghami

Il/La sottoscritto, con l'autoarchiviazione della propria tesi di dottorato nell'Archivio Istituzionale ad accesso aperto del Politecnico di Bari (POLIBA-IRIS), pur mantenendo su di essa tutti i diritti d'autore, morali ed economici, ai sensi della normativa vigente (Legge 633/1941 e ss.mm.ii.),

CONCEDE

- al Politecnico di Bari il permesso di trasferire l'opera su qualsiasi supporto e di convertirla in qualsiasi formato al fine di una corretta conservazione nel tempo. Il Politecnico di Bari garantisce che non verrà effettuata alcuna modifica al contenuto e alla struttura dell'opera.
- al Politecnico di Bari la possibilità di riprodurre l'opera in più di una copia per fini di sicurezza, back-up e conservazione.

Luogo e data 15.05.2026 Bari

Ali Maghami

Department of Mechanics, Mathematics and Management

PhD Program in Mechanical and Management Engineering
SSD: IIND-03/A
Mechanical Design and Machine Construction

Doctoral Thesis

Mechanical Design of Soft Viscoelastic Adhesive Interfaces via Physics-Guided Data-Driven Modeling

---

Ali Maghami

Supervisors

Prof. Antonio Papangelo
Prof. Michele Ciavarella
Prof. Merten Stender

PhD Cycle XXXVIII
Coordinator of the PhD Program: Prof. Giuseppe Casalino
Academic Years 2023–2026

To the lovers of freedom in Iran, who gave their lives for liberty.

It is said of that fellow, lifted high upon the gallows:
His only crime was making the hidden revealed.
If once more the Holy Spirit's grace helps
Others, too, would do what the Messiah once did.
Ghazal 143 of Hafez

Acknowledgements

I would like to express my deepest gratitude to my supervisors for their invaluable guidance and support throughout this research journey.

First and foremost, I am profoundly indebted to Professor Antonio Papangelo, my main supervisor, who has been like a brother to me throughout this journey. His unwavering mentorship, insightful feedback, and constant encouragement have greatly shaped the direction and quality of this work.

I am also deeply thankful to Professor Michele Ciavarella, whose extensive experience in this research area, along with his generous support and willingness to share ideas, has truly created a great spirit in the TriboDynamics Lab.

Special thanks go to Professor Merten Stender, who generously shared his expertise in machine learning. His guidance helped me navigate the complexities of data-driven approaches and supported my growth in this interdisciplinary field.

Their collective wisdom, patience, and dedication have been essential to the completion of this thesis. I am truly grateful for the opportunity to work under their supervision at the TriboDynamics Lab, and for the wonderful experience of living in Bari, surrounded by supportive friends and colleagues.

Last but not least, I would like to express my heartfelt appreciation to my spouse, Dr. Saba Askari Noghani, who first applied for a PhD at Politecnico di Bari and made it possible for me to become familiar with this wonderful research community. Her unwavering support, guidence and encouragement allowed me to focus entirely on my scientific pursuits.

Funding

This work is supported by the European Union (ERC-2021-STG, “Towards Future Interfaces With Tuneable Adhesion By Dynamic Excitation” - SURFACE, Project ID: 101039198, CUP: D95F22000430006). Views and opinions expressed are however those of the authors only and do not necessarily reflect those of the European Union or the European Research Council. Neither the European Union nor the granting authority can be held responsible for them.

Abstract

Designing adhesive interfaces in soft viscoelastic solids remains a significant challenge, as accurate prediction of surface forces requires a comprehensive understanding of bulk dissipation, loading rate, and contact geometry. At the same time, an open question is whether data-driven models can learn from high-fidelity simulations while preserving the physical structure imposed by mechanics and enabling real-time prediction. This thesis addresses both challenges by developing a predictive framework for the normal detachment of smooth rigid indenters from soft viscoelastic substrates, integrating analytical modeling, Boundary Element Method (BEM) simulations, and physics-guided machine learning.

Analytically, crack-propagation theory is extended to flat-punch detachment from finite viscoelastic layers, establishing three thickness-dependent regimes and showing that geometric confinement bounds adhesion amplification below the semi-infinite limit. For Hertzian contact, a four-parameter modified power-law constitutive model is introduced. Closed-form relations are derived in the time and frequency domains and coupled with Persson–Brener-type fracture mechanics to obtain an explicit scaling relation between unloading rate and crack speed at pull-off. These predictions are compared with adhesion experiments on PDMS at variable unloading rates to investigate the regime of validity of linear viscoelastic theory.

BEM simulations over a broad parameter space (Tabor parameter, material exponent, preload, viscoelastic spectrum, and layer thickness) confirm the analytical trends and identify a threshold contact radius below which finite-size effects suppress adhesion amplification. The results further show that the transition between DMT-like and JKR-like detachment depends jointly on the Tabor parameter and indentation depth.

Physics-augmented learning models trained on the simulation data predict pull-off force, effective surface energy, work to pull-off, and reduced descriptors of unloading trajectories. The use of learning models enables rapid prediction, reducing inference time from hours (required for numerical simulations) to milliseconds. Furthermore, embedding analytical descriptors as inputs improves physical consistency and reduces prediction error by 60% compared to purely data-driven models. The thesis establishes a predictive, mechanics-consistent hierarchy for fast and physically grounded analysis and design of soft adhesive interfaces.

Publications and Presentations

The results of this thesis have been published in three peer-reviewed journal articles and presented in five conference contributions in the field of mechanics. The author of this thesis is the first author of all the publications and presentations listed below, and all of them are based on the research conducted for this thesis.

All journal publications are available online in open-access form, and the corresponding links are provided below.

Journal Publications

- **A. Maghami**, M. Stender, and A. Papangelo (2025). "Pull-off force prediction in viscoelastic adhesive Hertzian contact by physics-augmented machine learning." *International Journal of Solids and Structures*, 322, 113584.
  doi: 10.1016/j.ijsolstr.2025.113584

- **A. Maghami**, Q. Wang, M. Tricarico, M. Ciavarella, Q. Li, and A. Papangelo (2024). "Bulk and fracture process zone contribution to the rate-dependent adhesion amplification in viscoelastic broad-band materials." *Journal of the Mechanics and Physics of Solids*, 193, 105844.
  doi: 10.1016/j.jmps.2024.105844

- **A. Maghami**, M. Tricarico, M. Ciavarella, and A. Papangelo (2024). "Viscoelastic amplification of the pull-off stress in the detachment of a rigid flat punch from an adhesive soft viscoelastic layer." *Engineering Fracture Mechanics*, 298, 109898.
  doi: 10.1016/j.engfracmech.2024.109898

Book Chapters

- A. Papangelo, M. Tricarico, and **A. Maghami** (2026). "Adhesive single and multi-asperity contacts." In: *Encyclopedia of Tribology and Lubrication.* Elsevier.

Conference Presentations

- **A. Maghami**, M. Stender, M. Ciavarella, and A. Papangelo, (2026) "Toward Multi-Scale Learning of Adhesive Contact Forces: From Single Asperities to Rough Surfaces" *Contact Mechanics International Symposium*, Lugano, Switzerland.

- **A. Maghami**, M. Stender, and A. Papangelo (2025). "Real-time insight into adhesion of a Hertzian indenter unloaded from a broadband viscoelastic substrate through a physics-augmented machine learning model." *12th European Solid Mechanics Conference*, Lyon, France.

- **A. Maghami**, M. Stender, and A. Papangelo (2025). "Toward prediction of time-resolved adhesive forces in viscoelastic Hertzian contacts through data-driven techniques." *Tribomechadynamics 2025 Conference*, August 25–27, Stuttgart, Germany.

- **A. Maghami**, Q. Wang, M. Tricarico, M. Ciavarella, Q. Li, and A. Papangelo (2025). "Viscoelastic crack propagation: Is the fracture process zone contribution to dissipation rate-dependent?" *12th European Solid Mechanics Conference*, Lyon, France.

- **A. Maghami**, M. Stender, and A. Papangelo (2025). "Toward real-time prediction of adhesion in viscoelastic substrates with physics-augmented machine learning." *8th International Conference on Computational Contact Mechanics*, Munich, Germany.

- **A. Maghami**, A. Papangelo, and M. Ciavarella (2024). "Soft adhesive viscoelastic substrates: Exploring augmented detachment stress with a rigid punch." *Contact Mechanics International Symposium*, Lyon, France.

Data Availability Statement

The research data, figure-generation scripts, and machine-learning resources underlying this doctoral thesis are archived in public repositories with persistent identifiers. Chapters 1, 2, and 7 are introductory, review, and concluding chapters, respectively, and therefore do not report primary datasets generated by this study. The primary research outputs supporting the remaining chapters include processed datasets and source/code files in formats such as `.py`, `.mat`, and `.csv`, together with trained model files.

All figures were generated from archived datasets using version-controlled MATLAB or Python scripts. The associated public repositories contain ready-to-run code to: (a) reproduce figures, or (b) train the machine-learning models used in this study, and (c) run the trained models for inference. Each repository includes a `README` and environment/dependency information.

Unless otherwise noted, code and scripts are released under Creative Commons Attribution 4.0 International. The archived datasets and code for this thesis are available at the following locations:

- Chapter 3 dataset at Zenodo: https://doi.org/10.5281/zenodo.10533305
- Chapter 4 dataset at Zenodo: https://doi.org/10.5281/zenodo.13358696
- Chapter 5 (ML) at Zenodo: https://doi.org/10.5281/zenodo.15039239;
  GitHub (Python): https://github.com/alimaghamii/ML4Adhesion;
  GitHub (MATLAB): https://github.com/alimaghamii/ML4Adhesion4Matlab
  FFN at GitHub: https://github.com/alimaghamii/FFN4Adhesion

Contents

Acknowledgements v

Abstract vii

Publications and Presentations ix

Data Availability Statement xi

List of Figures xviii

List of Tables xix

Nomenclature xxi

1 Introduction 1
- 1.1 Background and Motivation . . . 2
- 1.2 Problem Statement and Scope . . . 4
  - 1.2.1 Central research question . . . 4
  - 1.2.2 Scope and limitations . . . 4
- 1.3 Modeling Approach . . . 5
- 1.4 Research Gap . . . 5
- 1.5 Thesis Objectives . . . 6
- 1.6 Main Contributions . . . 7
- 1.7 Thesis Organization . . . 8

2 Literature Review 9
- 2.1 Theoretical background . . . 10
- 2.2 JKR contact model and short range adhesion . . . 11
- 2.3 From short-range to long-range adhesion . . . 14
- 2.4 Adhesion enhancement via viscoelasticity . . . 15
  - 2.4.1 Constitutive framework . . . 16
  - 2.4.2 Cohesive-zone route . . . 17
  - 2.4.3 Energy-balance route . . . 18
  - 2.4.4 Comparison and thesis relevance . . . 18
  - 2.4.5 Empirical scaling and open questions . . . 19

2.5 Data driven modelling and Machine Learning in adhesion 20
2.6 Summary and positioning of the thesis 22

3 Pull-Off of a Flat Rigid Punch from Viscoelastic Layers 25
3.1 Introduction 26
3.2 Detachment from a halfplane 27
3.3 Detachment from a thin layer 28
3.3.1 Elastic layer 28
3.3.2 Limiting solutions for a viscoelastic layer 30
3.4 Numerical implementation of the adhesive viscoelastic contact problem 31
3.5 Results 34
3.5.1 History dependence 34
3.5.2 Dependence on the unloading rate 37
3.6 Summary of findings 44

4 Adhesion in Broad-Band Viscoelastic Hertzian Contacts 47
4.1 Introduction 48
4.2 Modified power law model 49
4.3 The numerical model 52
4.4 Numerical results 56
4.4.1 Dependence of the detachment force upon the loading details . 56
4.5 Persson and Brener theory for broad-band viscoelastic materials . . . 59
4.6 Experimental adhesion tests 63
4.6.1 Material characterization 63
4.6.2 Experimental setup and comparison 65
4.7 Discussion 66
4.7.1 On the possibility of reaching the maximum enhancement . . 66
4.7.2 Energy dissipation within the process zone 68
4.8 Summary of findings 70

5 Data-driven surrogate models for viscoelastic adhesion 74
5.1 Introduction 75
5.2 Physical background and simulation framework 76
5.3 Machine learning for generalization beyond analytical models 78
5.3.1 Range of exploration beyond analytical models 78
5.3.2 Machine learning framework for tabular data 79
5.4 Results 81
5.4.1 Results for effective surface energy prediction 81
5.4.2 Results for prediction of work to pull-off 88

5.5 Toward prediction of adhesion trajectories through neural networks . 91
5.5.1 Feed-forward neural network 92
5.5.2 Segmented trajectory estimation model 92
5.5.3 Data preprocessing 93
5.5.4 Results for trajectory prediction 94
5.6 Summary and conclusions 96

6 Summary, Conclusions and Future Perspectives 98
6.1 Closure of the Thesis Objectives 99
6.2 Original Contributions and Main Findings 100
6.2.1 Cross-cutting synthesis 100
6.2.2 Contribution 1 (Mechanical) 100
6.2.3 Contribution 2 (Constitutive and analytical) 101
6.2.4 Contribution 3 (Numerical) 101
6.2.5 Contribution 4 (Methodological) 101
6.2.6 Answer to the central scientific question 102
6.3 Positioning Within the Broader Field 102
6.4 Limitations, Validity Range, and Critical Reflection 103
6.4.1 Physical-model limitations 103
6.4.2 Data-driven-model limitations 103
6.4.3 Scope of experimental validation 103
6.5 Future Perspectives 104
6.6 Final Remarks 104

Bibliography 106

Appendices 126
Appendix-I. Perfectly bonded layer 126
Appendix-II. More comparison with viscoelastic crack propagation theories 126
Appendix-III. Modified power law material model 127
Appendix-IV. Details of the PB model for the effective surface energy . . . 130
Appendix-V. Details of the boundary element method implementation . . . 132
Appendix-VI. Machine Learning Methods 133
Appendix-VII. Descriptive Statistics of the Dataset 134
Appendix-VIII. Upper-bound approximation of Hertzian work to pull-off . 135
Appendix-IX. Lower-bound approximation of work to pull-off 137
Appendix-X. Hyperparameter tuning 138

List of Figures

1.1 Adhesive interfaces from nature to engineering applications 2

2.1 Hertzian and JKR contact comparison 13
2.2 Asperity contact adhesion map and model comparison 15

3.1 Practical engineering applications of thin polymeric layers 26
3.2 Flat punch geometry with viscoelastic layer model 29
3.3 Three detachment regimes vs. layer thickness 32
3.4 Unloading curves with different loading histories 36
3.5 Pull-off stress versus layer thickness effects 37
3.6 Pull-off stress versus unloading rate dependence 38
3.7 Gap function and stress distributions at detachment 39
3.8 Pull-off stress versus crack propagation speed 41
3.9 Effective surface energy rate effects and enhancement 42
3.10 Work of separation during unloading process 44

4.1 Geometrical model and loading protocol 49
4.2 Time evolution of relaxation and creep compliance functions 53
4.3 Dimensionless load vs contact radius for varying parameters 55
4.4 Pull-off force vs the normalized crack velocity for different pre-load . 57
4.5 Threshold contact radius vs unloading rate 58
4.6 Effective surface energy vs crack velocity for power law materials . . . 60
4.7 Effective surface energy: BEM simulations vs PB predictions 62
4.8 Complex elastic modulus real and imaginary parts 64
4.9 Experimental setup and normal force vs contact radius 66
4.10 Pull-off force and effective surface energy vs unloading rate 67

5.1 Schematic of viscoelastic Hertzian contact unloading 75
5.2 Load–indentation response under varying inputs 77
5.3 Parameter exploration space visualization 79
5.4 Data-processing and modeling workflow 80
5.5 ML vs PA-ML predictions for effective energy 84

5.6 Indentation depth effect on effective surface energy 85
5.7 PA-ML captures JKR–DMT transition 86
5.8 PA-ML normalized surface energy vs indentation 88
5.9 Comparison: ML vs PA-ML for work-to-pull-off 90
5.10 PA-ML normalized work-to-pull-off vs unloading rate 91
5.11 Key trajectory points for neural network prediction 93
5.12 Cross-validation MSE by FNN architecture 94
5.13 Sequential FNN predictions across varying parameters 95

A.1 Effective surface energy vs. crack velocity 127
A.2 Kelvin and Wiechert models for viscoelastic materials 129
A.3 Fit of surface energy enhancement using MPL model 131
A.4 ML model performance comparison 134
A.5 PA-ML model performance comparison 135
A.6 Comparison of PA-ML predictions and glassy behavior upper bound . 137
A.7 PA-ML prediction with bounds for work to pull-off 138
A.8 XGBoost learning curve 138
A.9 Random Forest learning curve 139

List of Tables

3.1 Loading protocol parameters for pull-off tests 35

5.1 ML performance for effective energy prediction 82
5.2 PA-ML performance for effective energy 85
5.3 ML performance for work-to-pull-off 89
5.4 PA-ML performance for work-to-pull-off 89

A.1 Descriptive statistics for dataset parameters 135

Nomenclature

Latin symbols

a	Contact half-width (Ch. 3) or contact radius (Ch. 4–6)
a_0	Process-zone size $a_0 = E_0\Delta\gamma_0/(2\pi\sigma_0^2)$
a_T	Williams–Landel–Ferry temperature shift factor
b	Layer thickness (Ch. 3) or cohesive-zone outer radius (Ch. 2)
$C(t)$	Creep compliance function
C_0	Relaxed (rubbery) compliance $C_0 = 1/E_0$
C_∞	Glassy compliance $C_\infty = 1/E_\infty$
$C'(\omega)$	Real part of complex compliance
$C''(\omega)$	Imaginary part of complex compliance
$\overline{C}(\omega)$	Complex compliance
E_0	Rubbery (long-time) modulus
E_∞	Glassy (short-time) modulus
E^*	Composite elastic modulus
$E'(\omega)$	Storage modulus (real part of complex modulus)
$E''(\omega)$	Loss modulus (imaginary part of complex modulus)
$\overline{E}(\omega)$	Complex modulus
$\mathbf{E}_n(z)$	Exponential integral of order n
f	Frequency (Hz)
G	Energy release rate
G_{ij}	BEM influence matrix element
h	Interfacial gap (separation distance)
h_0	Equilibrium separation of the LJ potential
$H(\tau)$	Relaxation spectrum
k	Modulus ratio $k = E_0/E_\infty$
K_I	Mode-I stress intensity factor
$\overline{\mathrm{K}}(k)$	Complete elliptic integral of the first kind with modulus k
$K_n(x)$	Modified Bessel function of the second kind
l_0	Process-zone characteristic length $l_0 = E_0^*\Delta\gamma_0/(\pi\sigma_c^2)$

$L(\tau)$	Retardation spectrum
n	Power-law exponent of the MPL material model
p	Contact pressure distribution
P	Normal force on the indenter
P_0	Preload force
P_{po}	Pull-off force (maximum tensile force at detachment)
${}_p\mathrm{F}_q[a;b;z]$	Generalized hypergeometric function
r	Radial coordinate
r_u	Unloading rate (retraction velocity)
R	Radius of the sphere
$R(t)$	Relaxation function
T_g	Glass transition temperature
u_z	Normal surface deflection
v	Crack propagation velocity (un-normalized)
v_c	Crack-tip velocity
w_{po}	Work to pull-off
w_{sep}	Work of separation
ω	Angular frequency ($\mathrm{rad\,s^{-1}}$)

Greek symbols

α	Process-zone constant; $\alpha = \sigma_c/\sigma_0 \approx \pi/9$
α_{LJ}	Lennard-Jones numerical constant $\alpha_{LJ} = 9\sqrt{3}/16$
β	Crack-propagation scaling parameter in PB model
ε	Strain
ζ	Poisson correction factor for perfectly bonded layer
$\boldsymbol{i}$	Imaginary unit
$\Gamma(n)$	Gamma function
$\widehat{\Gamma}_{eff}$	Normalized effective surface energy
$\Delta\gamma_0$	Thermodynamic (equilibrium) surface energy
$\Delta\gamma_{eff}$	Effective (rate-dependent) surface energy
δ	Indentation depth
λ	Learning rate (shrinkage parameter) in XGBoost
μ	Tabor parameter
ν	Poisson's ratio

σ	Interfacial stress (LJ traction)
$\overline{\sigma}_{po}$	Mean pull-off stress for perfectly bonded layer
σ_0	Theoretical (cohesive) strength of the interface
σ_c	Critical stress at peak of Lennard-Jones potential
$\tan\delta$	Loss tangent $= E''(\omega)/E'(\omega)$
τ	Relaxation/retardation time (integration variable)
τ_0	Characteristic relaxation time of viscoelasticity
θ	Neural network weight and bias parameter vector

Dimensionless quantities

$\widehat{a}$	Normalized contact radius
$\widehat{b}$	Dimensionless layer thickness
$\widehat{C}(t)$	Dimensionless creep compliance
$\widehat{P}$	Normalized force
$\widehat{P}_{po}$	Normalized pull-off force
$\widehat{r}_u$	Normalized unloading rate
$\widehat{r}_{PB}$	Normalized crack propagation rate (Persson–Brener scaling)
$\widehat{t}$	Dimensionless time $\widehat{t} = t/\tau_0$
$\widehat{v}$	Normalized crack velocity $\widehat{v} = v\tau_0/l_0$
$\widehat{w}_{po}$	Dimensionless work to pull-off
$\widehat{\delta}$	Normalized indentation
$\widehat{V}_c$	Normalized crack velocity (Persson–Brener scaling)
Σ_0	Dimensionless cohesive strength

Abbreviations

BEM	Boundary Element Method
DMA	Dynamic Mechanical Analysis
DMT	Derjaguin–Muller–Toporov (model)
FNN	Feed-Forward Neural Network
GMM	Generalized Maxwell Model (Wiechert model)
JKR	Johnson–Kendall–Roberts (model)
LEFM	Linear Elastic Fracture Mechanics
LJ	Lennard-Jones

ML	Machine Learning
MPL	Modified Power Law (material model)
MSE	Mean Squared Error
PA-ML	Physics-Augmented Machine Learning
PB	Persson–Brener (crack propagation theory)
PDMS	Polydimethylsiloxane
R^2	Coefficient of Determination
RF	Random Forest
RMSE	Root Mean Squared Error
SIF	Stress Intensity Factor
SLS	Standard Linear Solid
WLF	Williams–Landel–Ferry (time–temperature superposition)
XPB	Extended Persson–Brener (physics descriptor used in PA-ML)

Chapter 1

Introduction

This chapter introduces soft viscoelastic adhesion as the central mechanics problem of the thesis and defines the scope of the work. It states the main research question, outlines the analytical, numerical, and data-driven strategy adopted in the dissertation, and maps the role of the chapters that follow.

1.1 Background and Motivation

Soft adhesive interfaces made of elastomers, gels, and other compliant polymers play a central role in many modern engineering systems. Their ability to undergo large deformations, conform to counter-surfaces, and sustain significant interfacial forces makes them relevant to gripping technologies, switchable adhesion, tactile interfaces, soft robotics, biomechanics, and frictional applications [1–4]. In such systems, adhesion is not merely a small correction to classical contact mechanics. It is often one of the main physical mechanisms governing attachment, load transfer, detachment resistance, and functional reliability.

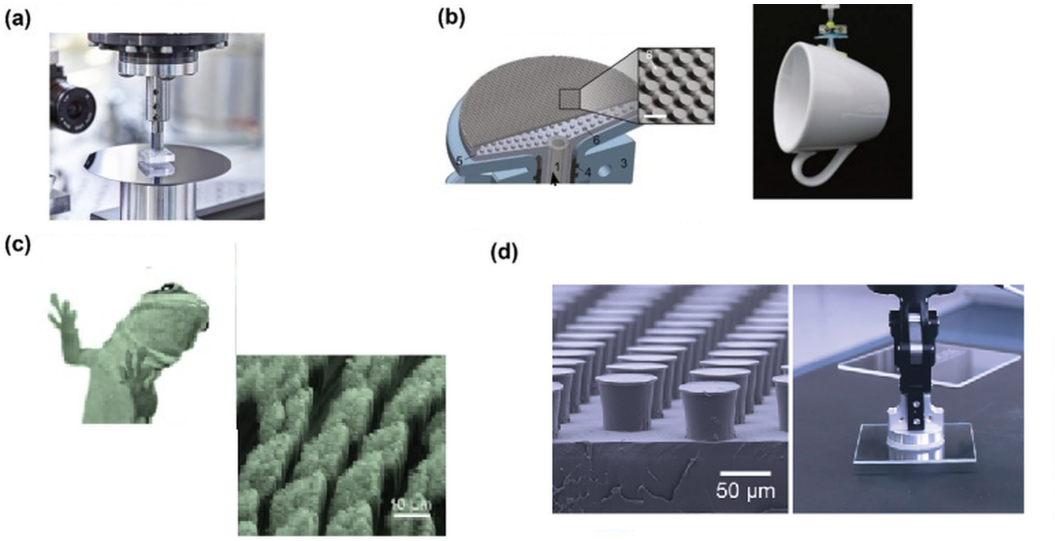

Figure 1.1: Adhesive interfaces from natural systems to engineering applications (adapted from [5] under a Creative Commons license): (a) Reversible handling of delicate items such as silicon wafers using buckling instability for release at INM. (b) Pick-and-place of curved objects via pneumatic actuation. (c) Gecko adhesion as a natural example, enabled by a hierarchy of keratinous, hair-like structures with submicron thickness. (d) Laboratory specimens of mushroom-shaped fibril arrays that mimic gecko adhesion and their use in a pick-and-place device.

Representative examples of these applications are shown in Figure 1.1, ranging from reversible handling of delicate technological components to bioinspired gripping strategies based on microstructures. These examples illustrate why adhesive contact in soft materials must be understood not only as a fundamental mechanics problem, but also as an enabling mechanism for controlled attachment and release in engineering systems.

The mechanical description of these interfaces begins with classical contact mechanics. In the absence of adhesion, the local interaction between smooth non-conforming elastic bodies can be approximated by the contact of an equivalent

paraboloid with an elastic half-space, as established by Hertz [6, 7]. At sufficiently small separations, the existence of adhesion is not in itself surprising; where intermolecular interactions generate attractive and repulsive tractions, commonly represented through force–separation laws associated with van der Waals interactions and, in many numerical formulations, approximated by Lennard-Jones-type relations [8]. In soft solids, these tractions interact strongly with bulk deformation, so that detachment resembles a fracture process rather than a purely geometric loss of contact. The balance between surface forces and elastic restoring stresses is commonly characterized by the Tabor parameter μ, which governs the transition from the so called DMT limit to the JKR limit. For the DMT-like behavior adhesion acts outside the contact zone on essentially undeformed profiles, while for the JKR limit, adhesion produces a crack-like singularity at the contact edge [9, 10].

The adhesion problem becomes more challenging when the substrate is viscoelastic. In that case, the response depends not only on geometry and work of adhesion, but also on the loading/unloading rate, the relaxation spectrum of the material, the loading history, and the finite size of the contacting bodies or layers [11–19]. The problem is, also multiscale: in geometrical terms, real contacting surfaces contain asperities spanning several orders of magnitude; in material terms, viscoelastic dissipation is distributed across a broad spectrum of relaxation times rather than concentrated at one characteristic time. These features make real-time predictive modeling and design of soft adhesive contacts particularly demanding [5]. Analytical models have limitations for identifying governing parameters, scaling laws, and limiting regimes, as they necessarily rely on simplifying assumptions. Numerical models can resolve the nonlinear, transient mechanics of detachment in much greater detail, yet they are computationally expensive. Data-driven models are therefore needed, not as replacements for mechanics-based approaches, but as efficient surrogates built upon them for design, rapid evaluation, and parametric exploration.

The present thesis is built around this hierarchy of models. The central idea is that analytical modeling, numerical simulation, and data-driven prediction should not be treated as disconnected methodologies, but combined into a coherent framework in which simplified mechanics provides interpretation, high-fidelity simulation provides reference data, and physics-guided machine learning delivers computationally efficient predictive capability. As will be shown in chapter 3 and chapter 4, unloading rate, constitutive broadness, and geometric confinement are the dominant drivers of detachment amplification. A central premise of the dissertation is therefore that the key challenge is not simply to include many physical ingredients, but to identify which of them control detachment in practice and how they can be retained in

predictive tools of progressively lower computational cost.

1.2 Problem Statement and Scope

The scientific problem addressed in this thesis is the prediction of adhesive detachment in soft viscoelastic interfaces when adhesion, bulk dissipation, unloading rate, and geometric confinement act simultaneously. The problem is not only mechanical but also methodological: analytical theories provide interpretation but remain restricted to simplified constitutive behavior, limiting geometries, or asymptotic regimes; high-fidelity numerical models can resolve the coupled problem, but at a computational cost too high for rapid parametric exploration, design, or control; and purely data-driven surrogates offer speed, yet do not automatically preserve the limiting structure imposed by contact mechanics and fracture-based interpretations of detachment.

1.2.1 Central research question

Can predictive models for soft viscoelastic adhesive contact be constructed that learn from high-fidelity simulations, retain the physical structure identified by analytical contact and fracture mechanics, and at the same time avoid the computational cost associated with multi-scale changes in material properties, loading conditions, and geometry?

1.2.2 Scope and limitations

The analysis is restricted to contacts between rigid indenters and soft viscoelastic substrates under normal loading and unloading, with particular emphasis on flat-punch and Hertzian geometries. The constitutive setting is linear viscoelasticity, and the experimental comparison is limited to a representative PDMS-based Hertzian contact system for which linear theory is shown to be sufficient up to unloading rates of approximately $100\,\mu$m/s [20, 21]. Roughness, multiasperity interactions, tangential loading, compliant counter-bodies, and fully nonlinear constitutive effects lie outside the present scope.

Within this setting, the main quantities of interest are the pull-off force, the average detachment stress, the effective surface energy, the work to pull-off, and finally a reduced but physically informative representation of the adhesive-force evolution during unloading.

1.3 Modeling Approach

Addressing the shortcomings of existing analytical and numerical models requires a unified predictive framework in which analytical, numerical, and data-driven models play distinct but complementary roles.

Analytically, the thesis builds on classical JKR and DMT theories and on Greenwood-type and Persson–Brener crack-propagation formulations [9, 12–15, 22, 23]. These approaches provide the interpretive structure of the problem: they identify governing parameters, clarify limiting regimes, and motivate reduced relations for finite-thickness detachment, broad-band viscoelastic scaling, and effective surface energy. Their value in the present work is therefore not only explanatory but also constructive, since the resulting descriptors are subsequently used as physical features to augment surrogate modeling.

Numerically, high-fidelity simulations based on the Boundary Element Method (BEM) are used to resolve the aspects that analytical theory cannot capture in sufficient detail, namely nonlinear traction–separation behavior, transient viscoelastic response, finite-size effects, and loading-history dependence [24, 25]. By discretizing only the contact interface through surface Green functions, the BEM provides a robust route to high-fidelity reference solutions and a systematic database for validation and parametric study. Its main limitation is computational cost, which remains substantial, typically ranging from $\sim 10^2$ to $\sim 10^4$ seconds per simulation for a single high fidelity contact model of an asperity.

Data-driven models are introduced to bridge this gap between mechanical fidelity and predictive speed [26]. Rather than treating machine learning as a replacement for mechanics, the thesis uses it as a surrogate layer built on top of the analytical and numerical framework. In particular, analytical descriptors derived from contact and fracture mechanics are embedded as guidance so that the learned models remain anchored to known scaling laws and limiting behaviors. The objective is therefore twofold: to achieve millisecond-level prediction and to determine whether physics augmentation genuinely improves robustness, extrapolation, and interpretability.

1.4 Research Gap

Despite the substantial progress, three specific gaps remain open. First, the finite-size limits on adhesion amplification in viscoelastic contacts, particularly for thin confined layers, have not been quantified systematically, and existing crack-propagation theories have not been extended to account for geometric confinement. Second,

most analytical and numerical studies of rate-dependent adhesion rely on single-relaxation-time constitutive models, whereas real engineering polymers display broad-band viscoelastic spectra that require a more general description. Third, although machine-learning surrogates have been applied to related contact-mechanics problems, they remain largely restricted to flat-to-flat configurations. Furthermore, their systematic combination with physics-augmented features derived from viscoelastic crack-propagation theory has not yet been established, and no surrogate framework has been proposed for predicting full unloading trajectories rather than scalar endpoints alone. These gaps are further substantiated through the detailed literature analysis presented in Chapter 2.

1.5 Thesis Objectives

The overall objective of the thesis is to develop a coherent predictive framework for soft viscoelastic adhesive interfaces that combines physical interpretability, numerical fidelity, and computational efficiency. More specifically, the dissertation pursues four objectives:

1. To clarify how fracture-mechanics scaling, unloading rate, layer thickness, and constitutive broadness govern adhesive detachment in soft viscoelastic systems, and to establish the analytical bounds on adhesion amplification.

2. To develop and validate a Boundary Element framework with Lennard-Jones interfacial tractions and viscoelastic response that resolves transient adhesive contact over the relevant ranges of Tabor parameter, preload, unloading rate, and broad-band constitutive spectrum, and to assess its consistency against analytical limits and representative Hertzian experiments within the linear-viscoelastic regime.

3. To quantify, through systematic parametric analysis, how contact geometry, preload, unloading rate, Tabor parameter, and constitutive spectrum control pull-off force, average detachment stress, effective surface energy, work to pull-off, and the evolution of the unloading curve, and to identify the conditions under which finite-size effects suppress the semi-infinite amplification limits.

4. To construct physics-augmented supervised-learning surrogates for both scalar detachment metrics and reduced-order unloading trajectories that retain the fidelity of high-fidelity BEM simulations while reducing prediction time by

orders of magnitude, and to determine whether analytical augmentation improves accuracy, extrapolation, and interpretability relative to non-augmented baselines.

1.6 Main Contributions

The thesis contributes new mechanical understanding, constitutive and analytical developments, numerical validation tools, and physics-augmented predictive models for soft viscoelastic adhesion:

- *Mechanical:* Identification of the finite-size limits of viscoelastic detachment, showing that geometric confinement governs the attainable adhesion amplification: in flat-punch contact through finite layer thickness, and in Hertzian contact through the threshold contact radius required to avoid finite-size effects.

- *Constitutive and analytical:* Introduction of a four-parameter modified power-law framework for broad-band viscoelasticity and its coupling with Persson–Brener crack-propagation theory, yielding reduced rate-dependent relations for effective surface energy, work to pull-off, and crack-speed scaling.

- *Numerical and validation:* Construction of a Boundary Element framework for adhesive viscoelastic contact with Lennard-Jones interfacial tractions and hereditary response, and use of that framework to assess analytical limits, explore the roles of preload and Tabor parameter, and validate the linear-viscoelastic predictions against representative PDMS-based Hertzian experiments.

- *Data-driven and methodological:* Development of physics-augmented supervised-learning surrogates for pull-off force, effective surface energy, and work to pull-off, together with a reduced-order neural-network representation of unloading trajectories based on a six-key-point description of the force–displacement curve, thereby extending the framework from scalar quantities to compact trajectory-level prediction.

The chapter-by-chapter results show how these contributions translate into specific mechanical findings, quantitative predictive performance, and experimentally delimited validity ranges; these outcomes are provided in Chapter 6.

1.7 Thesis Organization

The thesis is organized so the chapters follow a progressive development of models, both in physical complexity and in predictive scope:

- chapter 2 provides the literature review underlying the thesis, summarizing the main theories for adhesive contact and discussing the influence of viscoelasticity and recent data-driven approaches.
- chapter 3 addresses the detachment of a rigid flat punch from an adhesive viscoelastic layer of finite thickness, investigating the boundary element methodology against analytical limits and clarifying how layer thickness, unloading rate, and loading history influence the detachment stress and the effective adhesive energy.
- chapter 4 extends the analysis to Hertzian contact in broad-band viscoelastic materials, introducing the modified power-law constitutive framework, studying the respective roles of bulk dissipation and fracture-process-zone effects, and combining analytical, numerical, and experimental evidence to assess the validity and limitations of linear viscoelastic adhesion theories.
- chapter 5 develops physics-augmented machine-learning models for scalar quantities of engineering interest (pull-off force, effective surface energy, work to pull-off), clarifying the regimes in which analytical augmentation is effective, and then generalizes the data-driven framework to reduced-order prediction of unloading trajectories, moving from endpoint quantities to a compact representation of the adhesive-force evolution.
- chapter 6 summarizes the main findings and outlines directions for future work.

Chapter 2

Literature Review

This chapter supports the research problem stated in Chapter 1 by establishing the specific literature background needed for predictive modelling of soft viscoelastic adhesive detachment. Its task is to identify which parts of the field are structurally necessary for the thesis and which limitations in the existing literature motivate the developments of Chapters 3–5. Three foundations are required. First, an elastic adhesive reference model is needed to interpret detachment as an edge-controlled energetic problem; this role is played by JKR, DMT, and Maugis used to define the relevant asymptotic regimes. Second, viscoelastic crack-propagation theories are needed to explain rate-dependent enhancement of the effective surface energy and to clarify what remains unresolved for finite-size and broad-band materials. Third, because the numerical models required to resolve these effects are computationally demanding, the chapter reviews the state of data-driven and physics-guided surrogate modelling in adhesion and adjacent areas.

2.1 Theoretical background

This thesis concerns the normal approach and detachment of a single asperity in adhesive viscoelastic contact. The central theoretical problem is therefore not contact mechanics in general, but the selection of an elastic reference model that can be extended toward rate-dependent detachment in soft polymers and elastomers [1–4, 27–33].

For single-asperity contact, the natural elastic baseline is the Hertz solution for two smooth, non-adhesive bodies with locally quadratic geometry [6, 7]. The contact between two spheres of radii R_1 and R_2, characterized by Young's moduli $\{E_1, E_2\}$ and Poisson's ratios $\{\nu_1, \nu_2\}$, can be reduced to an equivalent problem involving a sphere of radius R, defined by $1/R = 1/R_1 + 1/R_2$, in contact with a rigid half-space with effective modulus E^* such that $1/E^* = (1-\nu_1^2)/E_1 + (1-\nu_2^2)/E_2$. In this framework, the contact response is governed entirely by compressive elasticity: Hertz provides the load–indentation relation, contact radius, and pressure field for a non-adhesive interface, and therefore serves as the reference problem against which adhesive effects must be assessed.

That reference is, however, fundamentally unable to describe the phenomena of interest in this thesis. A purely Hertzian contact cannot sustain tensile edge tractions, cannot predict a finite pull-off force, and cannot represent detachment instability during unloading. Once separation is no longer a negligible perturbation of a compressive contact, intermolecular forces must be incorporated explicitly. At nanometric separations these interactions are commonly represented through a force–separation law of van der Waals type, often idealized by a Lennard–Jones potential. For two nominally planar surfaces separated by a gap h, the corresponding normal stress can be written as follows [8]:

$$\sigma(h) = \frac{8\Delta\gamma_0}{3h_0}\left[\frac{h_0^3}{h^3} - \frac{h_0^9}{h^9}\right], \tag{2.1}$$

where $\Delta\gamma_0 = \int_{h_0}^{+\infty} \sigma(h)dh$ is the thermodynamic work of separation per unit area. The existence of a tensile branch in Eq. (2.1) is precisely what makes adhesion mechanically relevant: once the interface can support attraction outside the purely compressive Hertz regime, detachment must be described by a model that couples elastic deformation and surface forces.

For compliant solids with short-range adhesion, the most important such model is the theory developed by Johnson et al. [22]. The JKR framework incorporates elastic deformation and interfacial energy in a single asymptotic description, and it

can be reinterpreted through the Griffith energy balance as the propagation of an "external" crack at the edge of the contact [34, 35]. A useful complementary limit is the rigid Bradley result [36], for which the pull-off force is $2\pi R\Delta\gamma_0$, but for soft materials the relevant elastic adhesive reference is JKR rather than a rigid-body description.

The transition between adhesive regimes is commonly characterized by the Tabor parameter [37],

$$\mu = \sqrt[3]{\frac{R\Delta\gamma_0^2}{E^{*2}h_0^3}} \tag{2.2}$$

which measures the relative importance of elastic deformation at the contact edge compared with the interaction range h_0. Large values of μ correspond to short-range adhesion and strong deformation at the edge, which is the regime in which JKR becomes the appropriate elastic asymptote. Small values of μ instead lead toward DMT-like behavior. Other mechanisms such as roughness, shear, and externally induced vibrations may also affect adhesion [27, 38–58], but they are not the primary focus here.

2.2 JKR contact model and short range adhesion

In the present context, the JKR model is not introduced merely as a classical result, but as the elastic reference problem from which the later viscoelastic developments of the thesis depart. Its underlying assumptions should therefore be stated clearly: linear elasticity, small strains, smooth surfaces, short-range adhesion, and quasi-static loading of bodies that can be approximated locally as elastic half-spaces. Under these conditions, the contact between a rigid sphere of radius R and an elastic substrate can be determined by minimizing the total potential energy

$$\Pi = U + \Omega - \Gamma,$$

where U is the elastic strain energy, Ω is the potential of the external load, and $\Gamma = A\Delta\gamma_0$ is the interfacial energy associated with the contact area $A = \pi a^2$ [22].

The equilibrium condition is obtained from $\partial\Pi/\partial A = 0$. Under displacement control this gives

$$\frac{\partial U}{\partial A} = \frac{\partial \Gamma}{\partial A} = \Delta\gamma_0,$$

which reveals the essential content of the model: the adhesive contact edge is governed by an energy balance of Griffith type [34]. In other words, JKR turns the loss of contact into a crack-like event. That point is more important for this thesis than the

derivation itself, because it provides the conceptual bridge to viscoelastic detachment developed later.

By imposing $G = \Delta\gamma_0$, where $G = \partial U/\partial A$ is the energy release rate, one obtains the classical JKR relations between the external load P (positive in compression), the indentation δ, and the contact radius a [22]:

$$P = \frac{4E^* a^3}{3R} - \sqrt{8\pi E^* a^3 \Delta\gamma_0}\,, \tag{2.3}$$

$$\delta = \frac{a^2}{R} - \sqrt{\frac{2\pi a \Delta\gamma_0}{E^*}}\,, \tag{2.4}$$

Setting $\Delta\gamma_0 = 0$ recovers the non-adhesive Hertz solution, which makes explicit the role of JKR as its short-range adhesive extension. The same equilibrium condition may also be written in stress-intensity-factor form by using the Irwin relation between G and K_I [59]. The mode-I stress intensity factor is defined as

$$K_I = \lim_{\rho \to 0} \sigma_{yy}(x, 0)\sqrt{2\pi x}, \tag{2.5}$$

where y is normal to the crack plane and x is the distance from the crack tip. Using $G = K_I^2/(2E^*)$, equilibrium follows from $K_I = K_{Ic}$ with $K_{Ic} = \sqrt{2E^*\Delta\gamma_0}$.

For later use, it is convenient to introduce the dimensionless quantities

$$\widehat{P} = \frac{P}{\pi R \Delta\gamma_0}; \qquad \widehat{a} = \left(\frac{E^* R}{\Delta\gamma_0}\right)^{1/3} \frac{a}{R}; \qquad \widehat{\delta} = \left(\frac{E^* R}{\Delta\gamma_0}\right)^{2/3} \frac{\delta}{R}\,, \tag{2.6}$$

so that the JKR relations become

$$\widehat{P} = \frac{4\widehat{a}^3}{3\pi} - \frac{4\widehat{a}^{3/2}}{\sqrt{2\pi}}\,, \tag{2.7}$$

$$\widehat{\delta} = \widehat{a}^2 - \sqrt{2\pi\widehat{a}}\,. \tag{2.8}$$

The physical content of these relations is well known: compared with Hertz, adhesion enlarges the contact area at fixed load and permits tensile loads before detachment. Within JKR the contact pressure distribution $p(r)$ can be written as the superposition of the Hertzian pressure and a flat-punch contribution,

$$p\,(r) = p_1 + p_2 = \frac{2E^*\sqrt{a^2 - r^2}}{\pi R} - \sqrt{\frac{2E^* a \Delta\gamma_0}{\pi\,(a^2 - r^2)}}\,. \tag{2.9}$$

so that the stress becomes singular at the contact edge. This is precisely why

fracture-mechanics concepts become natural in adhesive detachment problems: the edge, rather than the interior of the contact, controls the loss of adhesion.

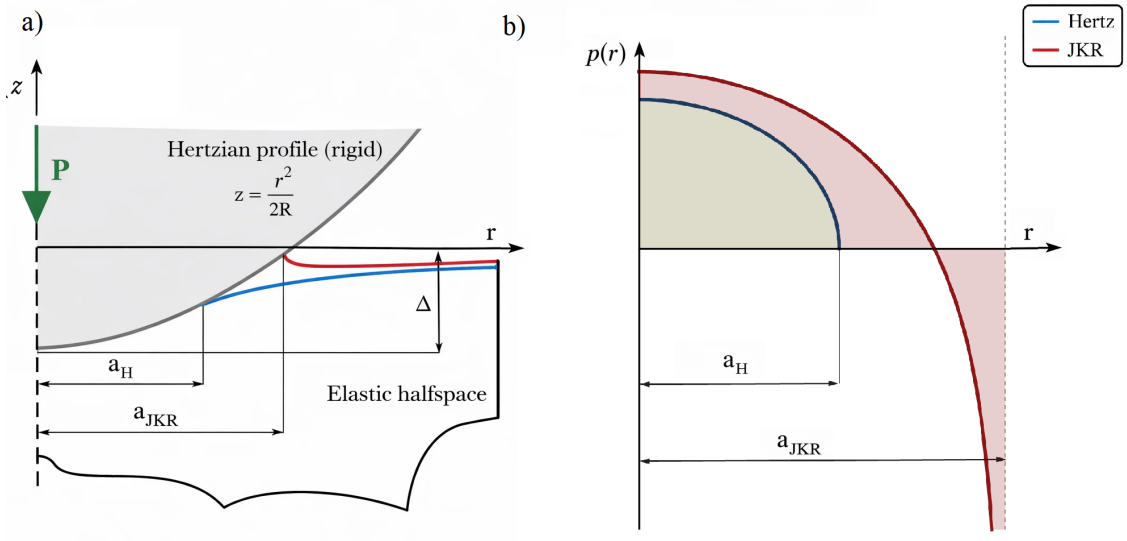

Figure 2.1: Schematic illustration comparing Hertzian and JKR contact models under identical indentation δ. (a) Vertical displacement fields and (b) pressure distributions are shown for both cases. For the same indentation, the resulting external load P differs between the two models. The contact radii a_H and a_{JKR} correspond to the Hertz and JKR solutions, respectively.

Figure 2.1 provides a schematic comparison between the Hertz and JKR solutions under the same imposed indentation. The key point is that adhesion modifies both the displacement field and the pressure distribution at the edge of the contact, producing a larger contact radius and allowing tensile loads before detachment. When the system is analyzed under load control, the maximum pull-off force occurs at $\widehat{P}_{po} = -3/2$, corresponding to $\widehat{a} = (9\pi/8)^{1/3}$ and $\widehat{\delta} = -\pi^{2/3}3^{1/3}/4$.

The importance of JKR extends beyond spherical contact. The same Griffith-type logic has been used to treat a variety of adhesive geometries, including sinusoidal contacts, dimpled surfaces, power-law indenters, and thin elastic layers [27, 60–65]. This breadth is relevant here only in a limited sense: it shows that JKR is not a narrow historical model, but a transferable energetic framework for short-range adhesive contacts. A particularly useful consequence is that, if the corresponding non-adhesive solution is known, the adhesive response can often be generated directly from it [64, 66]. In terms of the adhesiveless force–indentation relation $P(\delta)$ and

contact area $A(\delta)$, the generalized JKR correction takes the form

$$\delta_2 = \delta_1 - \sqrt{2\Delta\gamma_0 \frac{\partial A_1}{\partial \delta_1} \Big/ \frac{\partial^2 P_1}{\partial {\delta_1}^2}}\,, \tag{2.10}$$

$$P_2 = P_1 - \left(\frac{\partial P_1}{\partial \delta_1}\right) \sqrt{2\Delta\gamma_0 \frac{\partial A_1}{\partial \delta_1} \Big/ \frac{\partial^2 P_1}{\partial {\delta_1}^2}}\,, \tag{2.11}$$

where the subscript "2" denotes the adhesive solution to be determined, whereas the subscript "1" corresponds to the known adhesiveless solution.

It is useful to note that finite-size effects are already present in non-adhesive contact of elastic layers [7, 67]. When the contact size becomes comparable with the layer thickness, the substrate compliance and pressure distribution deviate from the half-space solution because the lower boundary participates in the load transfer. In adhesive viscoelastic detachment this bulk confinement effect interacts with, but is distinct from, the crack-tip or cohesive-zone length scale. The former modifies the elastic energy available during unloading, whereas the latter controls whether separation proceeds as edge crack propagation or as nearly uniform decohesion. This distinction motivates the finite-thickness analysis developed in Chapter 3.

2.3 From short-range to long-range adhesion

For the purposes of this thesis, DMT and Maugis are important mainly because they delimit the range of validity of JKR. The DMT family of models corresponds to the opposite asymptotic idea: adhesive interactions are treated as a perturbation of the non-adhesive Hertzian gap, and the deformation produced by adhesive tractions is neglected [23]. This description is appropriate when the interaction range is large compared with the elastic necking scale at the edge, that is, for small Tabor parameter. In that limit adhesion acts primarily outside the contact area and the interface remains close to the Hertz geometry.

For spherical contact it is common to use the simplified DMT-M approximation proposed by Maugis [9], in which the Hertzian compressive load is supplemented by a constant adhesive contribution equal to the rigid pull-off force $P_{po} = -2\pi R\Delta\gamma_0$. The corresponding dimensionless relations are

$$\widehat{P} = \frac{4\widehat{a}^3}{3\pi} - 2\,, \tag{2.12}$$

$$\widehat{\delta} = \widehat{a}^2\,. \tag{2.13}$$

The transition between the DMT and JKR limits is continuous rather than abrupt [10]. For this reason, Maugis [9] introduced a cohesive-zone model based on a Dugdale traction law, which regularizes the edge singularity and interpolates smoothly between the two asymptotic regimes. In practical terms, the Maugis framework introduces a finite cohesive region surrounding the true contact and shows how the response moves continuously from the long-range DMT side to the short-range JKR side as the Tabor parameter increases. Figure 2.2 summarizes this transition and compares the cohesive-zone prediction with numerical calculations based on Lennard–Jones interactions and BEM [8, 24, 68, 69].

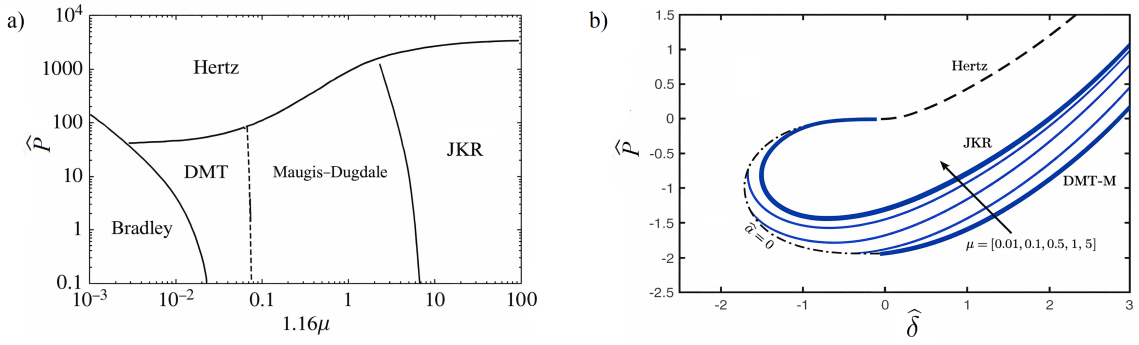

Figure 2.2: Asperity contact adhesion: (a) the adhesion map obtained by Johnson and Greenwood [70] for the contact of elastic spheres, adapted with minor modifications from Ciavarella et al. [8] (used with permission). (b) Dimensionless normal load $\widehat{P}$ as a function of dimensionless indentation $\widehat{\delta}$, comparing the predictions of the JKR model, the DMT-M model, and the cohesive-zone model of Maugis [71] for various Tabor parameters ($\mu = 0.01,\ 0.1,\ 0.5,\ 1,\ 5$). The adhesiveless Hertzian solution is shown as a black dashed line for reference, and in panel (b), the dot-dashed line indicates the condition $\widehat{a} = 0$.

Adhesion maps provide a compact summary of this regime selection [70]. At large compressive loads the adhesive correction becomes negligible and Hertz is sufficient; at small Tabor parameter the response approaches the Bradley/DMT side; at intermediate values a cohesive-zone transition is needed; and for sufficiently large μ the short-range JKR limit becomes appropriate.

2.4 Adhesion enhancement via viscoelasticity

The JKR framework becomes especially valuable once the contacting material is soft. However, polymers and elastomers, which are widely used in robotic gripping, switchable adhesion, and biomechanical interfaces [2, 4, 27–33], exhibit rate-dependent constitutive behavior. During unloading, the crack-like contact edge identified by JKR no longer responds with a rate-independent work of separation; instead, the apparent resistance to detachment is modified by bulk dissipation and fracture-

process-zone effects. For this reason, viscoelastic adhesive detachment can often be analyzed as the propagation of an external crack in a viscoelastic medium, provided that the limitations of this analogy are kept in mind.

2.4.1 Constitutive framework

The mechanical behavior of viscoelastic materials depends strongly on the excitation frequency ω [11]. At low frequencies, the material response is predominantly elastic and characterized by a relaxed Young's modulus E_0. At high frequencies, the response remains elastic but is governed by a higher, so-called instantaneous modulus E_∞, which can be several orders of magnitude larger than E_0 [18]. In the intermediate frequency range, where $E_0 < E(\omega) < E_\infty$, the material exhibits significant energy dissipation. In the frequency domain, the viscoelastic constitutive behavior can be described through a complex Young's modulus $\overline{E}(\omega)$. The ratio $\tan(\delta) = \mathrm{Im}\left(\overline{E}(\omega)\right) / \mathrm{Re}\left(\overline{E}(\omega)\right)$ provides a quantitative measure of the dissipative characteristics of the material.

An immediate consequence of viscoelastic dissipation is that the stress and strain fields at a given time t depend on the entire loading history of the system. Nevertheless, owing to the linearity of the constitutive behavior, the principle of superposition remains applicable. For instance, in the case of uniaxial loading, the stress $\sigma(t)$ and strain $\varepsilon(t)$ can be expressed through convolution integrals:

$$\varepsilon(t) = \sigma(0)\, C(t) + \int_{-\infty}^{t} C(t-\tau)\, \frac{d\sigma(\tau)}{d\tau} d\tau \,, \tag{2.14}$$

$$\sigma(t) = \varepsilon(0)\, R(t) + \int_{-\infty}^{t} R(t-\tau)\, \frac{d\varepsilon(\tau)}{d\tau} d\tau \,, \tag{2.15}$$

where $C(t)$ denotes the creep compliance function, which characterizes the strain response to a unit increment in stress $\sigma(t)$, and $R(t)$ is the relaxation function describing the stress response to a unit increment in strain $\varepsilon(t)$. Several mechanical analog models, all qualitatively similar, have been proposed to represent viscoelastic behavior. These models are constructed using combinations of springs and dashpots arranged in series and/or parallel configurations (e.g., the Wiechert model, the Kelvin model, or modified power-law formulations; see [11, 19, 72]).

Among these, the simplest model capable of capturing viscoelastic effects qualitatively is the Standard Linear Solid (SLS), characterized by a single relaxation time τ. Although useful analytically, the SLS model is usually too narrow-band to describe real elastomers, for which dissipation is distributed over a broad spectrum

of time scales. More accurate descriptions can be obtained through multi-mode viscoelastic models such as the Wiechert representation, at the cost of a large number of parameters [11]. Power-law formulations were introduced precisely to obtain compact broad-band descriptions through an effective continuous distribution of relaxation times [72].

In this context, it is useful to introduce an "effective" or "apparent" surface energy $\Delta\gamma_{eff}$, which accounts not only for the intrinsic surface energy $\Delta\gamma_0$ required to create new surfaces (typically assumed to be rate-independent), but also for the additional energy dissipated within the bulk material during deformation.

Given this rate dependence, the key objective is to relate the external loading to the velocity of the receding contact edge. Two main theoretical routes have been followed. The first relies on cohesive-zone models for the fracture process near the edge [12, 73–76]. The second extends Griffith-type energy balance to viscoelastic media [13–15, 77, 78]. Both routes inherit their physical relevance from the crack-like interpretation already introduced by JKR.

2.4.2 Cohesive-zone route

A fundamental aspect of viscoelastic crack propagation is the necessity of introducing a characteristic length scale. Indeed, in the framework of LEFM, a propagating crack is associated with a moving stress singularity that excites the material over the entire frequency spectrum, regardless of the crack velocity or applied load [79]. The viscoelastic crack propagation problem was first addressed by Schapery [73, 74] and Knauss [80] in the 1970s. In their formulation, it was assumed that bond rupture occurs within a finite region of length l_0 near the crack tip, referred to as the process zone. This characteristic length is expected to depend on the crack propagation velocity, since the material in the vicinity of the crack tip is subjected to an effective excitation frequency of the order $\omega \sim v_c/l_0$, where v_c denotes the crack speed. Building on this framework, Greenwood [12] employed a Dugdale-type cohesive zone model to evaluate the viscous contribution to the effective surface energy as a function of crack velocity. For the case of an SLS material, Greenwood [12] derived a closed-form expression for the dependence of the effective surface energy on the crack propagation velocity, $\Delta\gamma_{eff}(v_c)$, given by:

$$\Delta\gamma_{eff} = \Delta\gamma_0 \left[k + \frac{(1-k)}{2} \frac{d}{v_c \tau} k \int_0^1 H(\xi) \exp\left(-\frac{d}{v_c \tau} k (1-\xi) \right) d\xi \right]^{-1}, \tag{2.16}$$

$$H(\xi) = 2\xi^{1/2} - (1-\xi) \ln\left(\frac{1+\xi^{1/2}}{1-\xi^{1/2}} \right), \tag{2.17}$$

where $l_0 = \frac{\pi E_0 \Delta\gamma}{4\sigma_0^2}$ denotes the characteristic length of the process zone.

2.4.3 Energy-balance route

An alternative formulation based on energetic considerations was first introduced by Persson and Brener [13] and subsequently refined by Persson and co-authors [14, 15]. In this approach, the classical Griffith [34] energy balance is extended to account for viscoelastic dissipation. Specifically, under steady-state crack propagation, the power supplied to the system per unit area by the external loading is assumed to be equal to the sum of the power required to create new surfaces and the power dissipated within the bulk due to viscoelastic effects.

To evaluate the bulk dissipation, Persson and Brener [13] adopted the classical mode-I singular stress field from LEFM. However, in order to regularize the singularity, a threshold stress σ_c is introduced, representing the stress level at which molecular bonds break. Based on this assumption, a characteristic length scale a_P is defined as the effective radius of the crack tip, such that $\sigma_c = K_I / \sqrt{2\pi a_P}$, where K_I is the mode-I stress intensity factor.

The viscoelastic energy dissipation is then computed by integrating over a finite frequency range, from zero up to a cut-off frequency $\omega_c = 2\pi v_c / a_P$, where v_c denotes the crack propagation velocity (see [13–15]). Following this procedure, Persson and Brener [13] derived an implicit relation for the effective surface energy $\Delta\gamma_{eff}(v_c)$:

$$\Delta\gamma_{eff} = \Delta\gamma_0 \left[1 - E_0 \frac{2}{\pi} \int_0^1 \frac{\sqrt{1-x^2}}{x} \operatorname{Im}\left(\frac{1}{E(x\omega_c)} \right) dx \right]^{-1}, \tag{2.18}$$

where $\omega_c = \frac{2\pi v_c}{a_0} \frac{\Delta\gamma_0}{\Delta\gamma_{eff}}$ denotes the cut-off frequency, and $a_0 = E_0 \Delta\gamma_0 / (2\pi\sigma_c^2)$.[1]

2.4.4 Comparison and thesis relevance

For a semi-infinite body, both cohesive-zone formulations and energy-based approaches predict a monotonic increase of the effective surface energy $\Delta\gamma_{eff}$ with increasing crack propagation velocity v_c, up to the theoretical high-frequency limit

[1] In defining a_0, the sphere is assumed to be rigid, so that $G = K_I^2/(2E_0^*)$ (see [13, 81]).

$\Delta\gamma_{eff}/\Delta\gamma_0 = E_\infty/E_0$ [82]. In LEFM terms, this follows because the far-field stress intensity required for propagation must increase as the relevant modulus shifts from the relaxed to the high-frequency response, so that $\Delta\gamma_{eff}$ scales with $E^*(\omega)/E_0^*$. For real elastomeric materials such as PDMS, the ratio E_∞/E_0 can reach values on the order of 10^3, which explains why the apparent work of separation can exceed the thermodynamic surface energy by orders of magnitude [19].

The two routes nevertheless encode different assumptions and therefore serve different purposes in this thesis. Greenwood-type cohesive-zone theories retain an explicit process-zone description and are consequently better suited to problems in which the fracture length and geometric confinement must be tracked directly; this is the logic adopted in Chapter 3, where Greenwood's theory is extended to finite-size viscoelastic layers. Persson–Brener-type theories instead absorb the near-tip physics into an energy-balance formulation written in terms of the bulk viscoelastic spectrum and a stress-based length scale; this makes them more convenient to be extended to the broad-band viscoelasticiy, and Hertzian analysis developed in Chapter 4 and for the analytical descriptor later embedded in the surrogate-modeling framework of Chapter 5. The thesis therefore does not rely on a single crack-propagation model for all geometries: it uses Greenwood-type reasoning when confinement is the central variable, and Persson–Brener-type reasoning when the objective is a tractable broad-band description of spherical detachment.

2.4.5 Empirical scaling and open questions

Moreover, both the cohesive-zone approach [12] and the energy-based formulation [13] predict that, within an intermediate range of crack velocities, the effective surface energy follows a power-law dependence on the crack tip velocity. This behavior is consistent with the empirical relation proposed by Gent and Schultz [83]:

$$\frac{\Delta\gamma_{eff}\left(v_c\right)}{\Delta\gamma_0} = 1 + \left(\frac{v_c}{v_{ref}}\right)^n, \tag{2.19}$$

where $v_{ref} = \left(k_{GS}a_{GS}^n\right)^{-1}$ and $\{k_{GS}, n\}$ are the material constants introduced by Gent and Schultz [83], with $0 < n < 1$, while a_{GS} is the Williams–Landel–Ferry (WLF) shift factor used to account for the temperature dependence of the viscoelastic modulus [84].

Although the Gent–Schulz relation is phenomenological in nature, it remains widely adopted in engineering practice due to its strong agreement with a large body of experimental observations dating back to the 1970s [19, 83, 85–88]. In the present thesis its role is limited but definite: in Chapter 4 it is used as an empirical fit to

experimentally inferred effective surface energies, thereby exposing the part of the rate dependence that is not captured by the linear viscoelastic BEM/Persson–Brener framework.

Despite this progress, some key aspects of viscoelastic adhesion remain insufficiently clarified. Most available formulations and experiments have been developed for semi-infinite bodies, so the effect of finite layer thickness on the detachment stress, on the transition between crack-like and nearly uniform decohesion, and on the maximum attainable adhesion amplification is still not available in a general predictive form. At the same time, phenomenological laws such as Gent–Schulz are useful for correlating data, but they do not explain how the amplification parameters depend on geometry, confinement, preload history, or intrinsic material length scales, nor do they clearly delimit the range over which a simple power-law increase in $\Delta\gamma_{eff}$ remains meaningful. A further unresolved point concerns broad-band viscoelastic materials, for which the respective contributions of bulk dissipation and fracture-process-zone dissipation are difficult to separate quantitatively: standard linear solid models are too narrow-band to represent real elastomers faithfully, whereas full spectral descriptions are often too case-specific to permit general conclusions. These unresolved mechanics issues are not separate from the computational problem discussed next; rather, they are the reason why the thesis combines analytical crack-propagation theory with high-fidelity simulations and, subsequently, with surrogate models.

2.5 Data driven modelling and Machine Learning in adhesion

Numerical modeling of viscoelastic adhesive contacts requires defining a relaxation function and integrating it via time-marching schemes [19], which involve iterative solvers for the nonlinear contact problem at each time step [24, 25, 89]. Because the computational cost of these simulations depends on material bandwidth, mesh density, loading history, and the number of time increments needed to resolve the underlying physics [90], the wall-clock time can vary by orders of magnitude across parameter combinations. This poses a practical barrier to embedding adhesive-contact analyses in design-optimization loops or in real-time monitoring, where a fixed and low evaluation cost per query is essential.

In response to this computational bottleneck, machine learning (ML) has increasingly been adopted as a surrogate-modeling strategy in engineering mechanics [91, 92]. A purely data-driven approach, however, often struggles to generalize outside its training domain when data are scarce and physical consistency is mandatory. A

taxonomy of *informed* machine learning is being used [93], showing that incorporating prior physical knowledge systematically improves accuracy, interpretability, and extrapolation capability. This incorporation could be applied through input descriptors, architectural constraints, physics-based loss terms, or hybrid training data. Within soft-material mechanics, this idea has been realized concretely by Zhu et al. [94], who embedded governing equations and constitutive relations in a transfer-learning-enhanced physics-informed neural network for inverse parameter identification, and by Eshkofti and Hosseini [95], who applied a modified physics-informed neural network to coupled thermoelastic wave propagation. Comparable physics-informed operator-learning strategies have also been explored in other continuum settings, such as nonlinear wave-field reconstruction [96], confirming the methodological reach of embedded-physics learning while remaining mechanically remote from adhesive contact. Taken together, these studies show that physics-guided learning can stabilize predictions under sparse-data conditions, even in problems far from adhesion.

The adjacent fields of fracture mechanics, contact mechanics, and tribology have already absorbed ML tools at a mature level. In fracture, neural networks and decision-tree methods have been used to predict toughness [97, 98], to improve cross-geometry transferability via graph neural networks and transfer learning [99], to characterize indentation-driven instabilities through hybrid simulation–experiment–ML workflows [100], and to discover interpretable fracture relations via mechanics-informed symbolic regression [101]. In contact mechanics, Kalliorinne et al. [102] trained neural networks on surface-topography descriptors to bypass repeated numerical contact computations, while Goodbrake et al. [103] and Motiwale et al. [104] developed neural-network finite-element methods that embed equilibrium directly in the learning architecture. Most notably, Sahin et al. [105, 106] formulated physics-informed neural networks for forward and inverse elastic contact problems including Hertzian benchmarks, enforcing complementarity and boundary conditions within the training loop. Parallel developments in tribology [107–110], constitutive reconstruction [111], and material-characterization surrogates [112, 113] further confirm the broad penetration of ML in mechanics-related disciplines. Critically, however, all of these contributions either omit adhesive interactions entirely or treat non-adhesive elastic contacts, leaving viscoelastic adhesive detachment unaddressed.

Within adhesion itself, a distinct and rapidly growing literature applies ML not as a physics-augmented surrogate but either as an inverse-design engine for structured dry-adhesive systems or as a rapid predictor of bonded-joint strength. Kim et al. [114] pioneered the design-oriented direction by using deep-learning opti-

mization to discover adhesive pillar shapes that improve stress uniformity beyond what parametric families can achieve. Subsequent studies extended this approach to experimentally validated fibril design on PDMS and elastomers [115], composite-pillar architecture with tunability objectives [116], directional adhesion enhancement [117], fabrication-aware shear optimization of microstructures [118], functionally graded fibrillar adhesives [119], and, more recently, reinforcement-learning-based exploration of high-dimensional pillar-shape spaces [120]. A related but mechanically different line uses supervised regression to estimate global failure metrics in adhesively bonded structures, as illustrated by the prediction of single-lap-joint failure loads from heterogeneous datasets spanning metallic and composite adherends [121]. Although these contributions demonstrate significant integration of ML into adhesive engineering, they target either geometry optimization or joint-strength prediction rather than the continuum mechanics of contact formation and separation; none of them constructs a surrogate for the force–displacement–contact-area trajectory of a detaching interface.

Despite the breadth of these developments, a clear gap remains. The general informed-ML literature provides the methodological vocabulary but does not specialize it to adhesive contact. Fracture-ML studies predict crack-level quantities without entering the contact–adhesion domain. Contact-ML methods, including the most advanced physics-informed formulations, operate in elastic, non-adhesive settings. Adhesion-related ML studies focus on microstructure optimization or bonded-joint strength prediction rather than continuum surrogate modeling. No existing work addresses physics-guided surrogate modeling for curved single-asperity viscoelastic adhesive contact. Specifically, Hertzian detachment with unloading-rate dependence, broad-band viscoelasticity, and trajectory-level prediction of force, displacement, and contact radius despite their importance, gained less attention. Closing this gap is the objective of the remaining chapters of this thesis.

2.6 Summary and positioning of the thesis

The literature reviewed above defines a three-part problem. First, existing viscoelastic adhesion theories do not yet provide a general predictive account of how finite size and confinement cap the attainable amplification of pull-off force or effective surface energy. Second, much of the analytical literature remains tied to single-relaxation-time constitutive models, whereas the broad-band spectra of real elastomers require reduced descriptions that remain interpretable while extending beyond SLS behavior. Third, although machine learning is now widespread in mechanics and adhesive engineering, no prior work has developed a physics-guided surrogate for curved

single-asperity viscoelastic adhesive contact that predicts both scalar detachment metrics and reduced unloading trajectories. Taken together, these gaps show that the unresolved problem is not merely one of adding more data or more computation, but of connecting fracture-based interpretation, numerical fidelity, and predictive efficiency within a single framework.

These gaps map directly onto the objectives stated in Chapter 1. The first objective is addressed by clarifying how fracture-mechanics scaling, unloading rate, and geometric confinement govern detachment; the second by constructing and validating a BEM framework with Lennard–Jones tractions and viscoelastic hereditary effects; the third by quantifying how preload, constitutive broadness, and geometry control both scalar and trajectory-level responses; and the fourth by embedding physically motivated descriptors in learning-based surrogates. The remainder of the thesis follows this logic. Chapter 3 studies the detachment of a rigid flat punch and extends Greenwood-type crack-propagation ideas to finite-size layers. Chapter 4 develops the Hertzian problem for broad-band viscoelastic materials through Persson–Brener-type scaling, BEM simulations, and experiment. Chapter 5 then translates that mechanics framework into physics-augmented surrogate models for scalar quantities and reduced unloading trajectories.

Chapter 3

Pull-Off of a Flat Rigid Punch from Viscoelastic Layers

Publication note. The work presented in this chapter led to the peer-reviewed paper published in *Engineering Fracture Mechanics* [18].

This chapter establishes the flat-punch problem as the first mechanics benchmark of the thesis and uses it to clarify how confinement alters viscoelastic detachment. It combines analytical arguments and boundary element simulations to trace the transition from fracture-controlled pull-off to nearly uniform decohesion as the layer thickness decreases. The chapter therefore defines the finite-size limits of adhesion amplification before the analysis moves to Hertzian contact.

3.1 Introduction

Adhesive contact involving thin viscoelastic layers is central to many engineering systems, including tapes, coatings, gaskets, soft grippers and layered polymeric interfaces, where the bond strength is governed not only by the material properties but also by geometric confinement. In such systems, the relevant quantity is often the detachment stress, namely the maximum tensile stress required to separate the interface. While viscoelastic adhesion has been studied extensively for semi-infinite substrates [122–124], a predictive understanding of how finite layer thickness modifies the pull-off stress is still missing. This gap is mechanically important because confinement can change the mode of failure, promote a transition from crack-like propagation to nearly uniform decohesion, and strongly alter the maximum adhesion amplification attainable during unloading.

This issue is also relevant from an experimental and design standpoint. Thin layer configurations are routinely employed in applications such as those shown in Figure 3.1, and they are equally attractive as test geometries for extracting interfacial and cohesive properties, as suggested for instance by Peng et al. [125]. A rigorous treatment of flat-punch detachment from a viscoelastic layer is therefore needed both to interpret measurements correctly and to identify how thickness and unloading rate can be exploited to enhance interfacial strength.

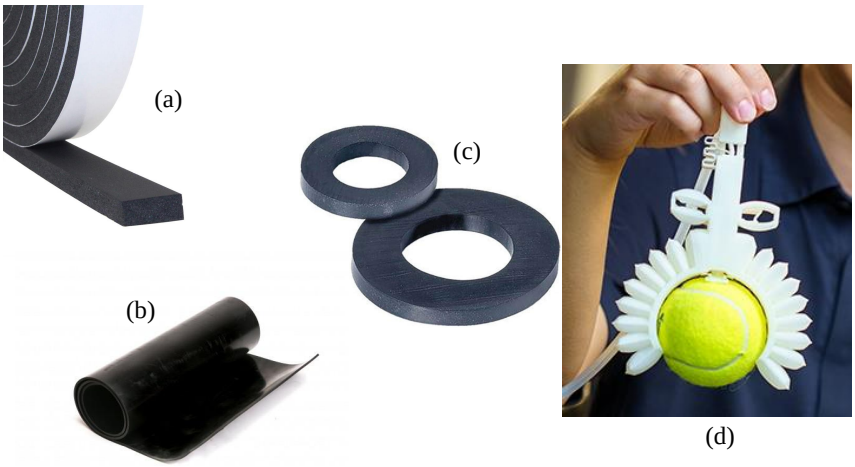

Figure 3.1: Practical engineering applications where thin polymeric layers are used: (a) rubber tape, (b) polymeric carpet, (c) gasket, (d) soft gripper for delicate handling and manipulation (UCSD Jacobs School of Eng., CC BY-NC-SA 4.0). (From Ref. [18])

In this chapter, we study the detachment of a rigid flat punch from an adhesive viscoelastic layer of finite thickness b under plane-strain conditions. The objective is to establish how confinement and rate effects act together in setting the pull-off

stress and the effective adhesive energy, and to determine the conditions under which very thin layers may approach the theoretical interfacial strength. To this end, Section 3.2 recalls the reference half-plane solution, while Section 3.3 develops the thin-layer elastic limits using Johnson's "thin strip" approximation [126] and the Griffith energy balance, thereby identifying the relevant detachment regimes and the bounds of the viscoelastic response. Section 3.4 then introduces the boundary element formulation, combining a standard linear viscoelastic model for the layer with a rate-independent Lennard-Jones force-separation law at the interface. Section 3.5 presents the numerical results and compares them with Greenwood's theory for viscoelastic crack propagation [12], which is here extended to account for finite-size effects. Particular attention is devoted to the role of loading history, layer thickness and unloading velocity in controlling pull-off stress amplification.

3.2 Detachment from a halfplane

Let us consider the plane contact problem of a flat punch of semi-width a indenting an elastic adhesive frictionless halfplane with Young modulus E and Poisson ratio ν. By applying the Griffith energy balance, the pull-off force [127, 128] is given by

$$P_{po} = L\sqrt{2\pi E^* \Delta\gamma_0 a}\,, \tag{3.1}$$

where L is the layer width, $E^* = E/(1-\nu^2)$ is the plane strain elastic modulus. Hence the mean interfacial stress at pull-off is

$$\overline{\sigma}_{po} = \sqrt{\frac{\pi E^* \Delta\gamma_0}{2a}}\,, \tag{3.2}$$

which has the classical Linear Elastic Fracture Mechanics (LEFM) square-root dependence with respect to the punch semiwidth a. Overbar indicates here the mean value. This implies that smaller punches have a higher pull-off stress, potentially reaching the theoretical strength (or the cohesive strength) of the interface, denoted as σ_0. This is typically observed for punches with a semi-width less than the following typical fracture length

$$a_0 = \frac{\pi}{2}\frac{E^* \Delta\gamma_0}{\sigma_0^2}\,. \tag{3.3}$$

In what follows in the paper we shall assume that the punch size is $a >> a_0$ as we are interested in the transitions due to the finite size of the layer rather than the size of the punch. For the latter effect the reader is referred to Ref. [122].

Hence, in dimensionless form, we have the following relations

$$\widehat{\overline{\sigma}}_{po} = \frac{\overline{\sigma}_{po}}{\sigma_0} = \frac{1}{\sqrt{a/a_0}} \,, \tag{3.4}$$

$$\frac{a_0}{h_0} = \frac{9\sqrt{3}\pi}{32\Sigma_0} \approx \frac{1.53}{\Sigma_0} \,, \tag{3.5}$$

where we have assumed a Lennard-Jones force-separation law, for which $\Delta\gamma_0 = \alpha_{LJ} h_0 \sigma_0$, where h_0 is the range of interaction and $\alpha_{LJ} = \frac{9\sqrt{3}}{16}$ is a constant, $\widehat{a} = a/h_0$, $\Sigma_0 = \sigma_0/E^*$ is usually in the range of $[0.1 \div 1]$ for soft polymers [128–130], implying a_0 to be 1 to 10 times higher than the range of attractive forces. For a true crystal, this would imply a range of few nanometers, but for soft materials, the range of adhesive forces may be larger. If a viscoelastic material with relaxed modulus E_0 and instantaneous modulus E_∞ is considered, then in the limit of very slow and very fast unloading rate we will have

$$\begin{cases} \widehat{\overline{\sigma}}_{po} = \sqrt{\frac{9\sqrt{3}\pi}{32\Sigma_0 \widehat{a}}} = \frac{1}{\sqrt{a/a_0}} \,; & \text{slow limit } E = E_0 \,, \\ \widehat{\overline{\sigma}}_{po} = \sqrt{\frac{9\sqrt{3}\pi}{32\Sigma_0 k\widehat{a}}} = \frac{1}{\sqrt{ka/a_0}} \,; & \text{fast limit } E = E_\infty \,, \end{cases} \tag{3.6}$$

where $k = E_0/E_\infty$ and $\widehat{a} = a/h_0$.

3.3 Detachment from a thin layer

If the substrate has a finite thickness, it is necessary to consider the effect of thickness in the analysis. Hence, here we focus on the plane contact problem of a flat punch with a semi-width of a indenting an adhesive layer with a thickness of b (Fig. 3.2). We first focus on the linear elastic solution, and then we will provide the limiting solutions for the viscoelastic problem based on the elastic formulation.

3.3.1 Elastic layer

Let us consider the layer in plane strain and supported by a rigid foundation. In the following the case of frictionless contact between the layer and the rigid substrate is considered while the correction due to the Poisson effect for the case of a layer perfectly bonded to the substrate is shown in Appendix I.

Following Johnson [126], we assume that plane sections remain plane upon loading. Hence for the case of no friction between the layer and the rigid substrate, the load

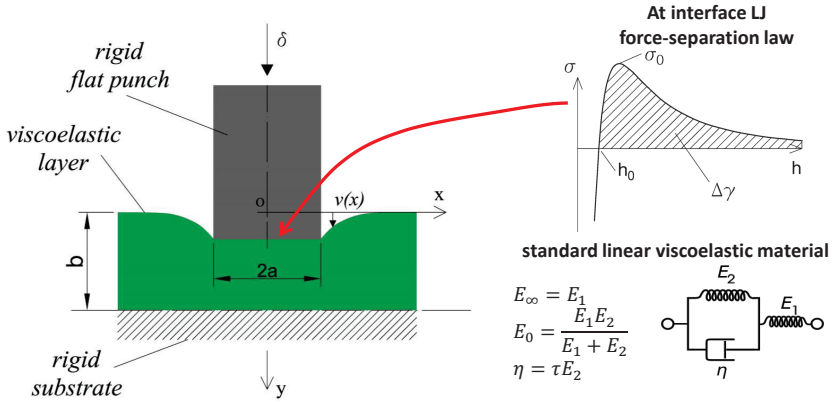

Figure 3.2: On the left is a sketch of a flat punch being loaded on a viscoelastic adhesive layer of thickness b. The numerical implementation employs the Lennard-Jones force-separation law, while the viscoelastic material is represented using a standard linear model, as depicted in the lower-right panel. (From Ref. [18])

P and the corresponding elastic strain energy U_E stored in the layer are

$$P = -2aLE^* \frac{\delta}{b} , \tag{3.7}$$

$$U_E = aLE^* \frac{\delta^2}{b} , \tag{3.8}$$

where δ is the indentation considered positive when the flat punch is approaching the substrate, consequently, P is positive when tensile. At unloading, the Griffith energy balance requires the elastic strain energy released per unit area to be equal to the surface energy. Hence, assuming detachment occurs immediately, we have the following relations

$$\frac{1}{2L}\frac{\partial U_E}{\partial a} = \Delta\gamma \rightarrow \begin{cases} \delta_{po} = -\sqrt{\frac{2b\Delta\gamma}{E^*}} , \\ \overline{\sigma}_{po} = \sqrt{\frac{2E^*\Delta\gamma}{b}} , \end{cases} \tag{3.9}$$

where, δ_{po} and $\overline{\sigma}_{po}$ are the indentation and the average interfacial stress at pull-off respectively. Notice that the pull-off stress depends on the layer thickness as $\overline{\sigma}_{po} \propto b^{-1/2}$, hence it is possible to define a characteristic thickness b_0 of the substrate where $\overline{\sigma}_{po}$ reaches the theoretical interfacial strength σ_0, i.e.

$$b_0 = \frac{2E^*\Delta\gamma}{\sigma_0^2} = \frac{4}{\pi}a_0 \approx 1.27a_0 , \tag{3.10}$$

which is of the same order of magnitude of a_0. Experiments with PDMS elastomers in Peng et al. [125], show that this b_0 is of the order of 0.1 mm, where clearly their loading rate corresponds to a certain effective elastic modulus. On the other hand,

in the limit of a very thick layer, we should obtain the half-plane solution, for which we can utilize Eq. (3.2) and Eq. (3.9) to determine a length scale

$$b_1 = \frac{4a}{\pi} \,, \tag{3.11}$$

with the meaning that for substrates thicker than b_1 one should anticipate the half-plane behaviour. Notice that, while b_0 is a characteristic lengthscale that depends on the material and interfacial properties, b_1 depends on the punch semi-width. Overall as indicated by Eq. (3.10) and Eq. (3.11), and as illustrated in Fig 3.3, we identify the following three regimes

$$\begin{cases} \overline{\sigma}_{po} = \sigma_0 \,, & b < b_0 \\ \overline{\sigma}_{po} = \sqrt{\frac{2E^*\Delta\gamma}{b}} \,, & b_0 \le b \le b_1 \\ \overline{\sigma}_{po} = \sqrt{\frac{\pi E^*\Delta\gamma}{2a}} \,, & b > b_1 \end{cases} \tag{3.12}$$

or, in dimensionless form,

$$\begin{cases} \widehat{\overline{\sigma}}_{po} = 1 \,, & b/a_0 < \frac{4}{\pi} \\ \widehat{\overline{\sigma}}_{po} = \sqrt{\frac{9\sqrt{3}}{8\Sigma_0 \widehat{b}}} = \sqrt{\frac{4}{(b/a_0)\pi}} \,, & \frac{4}{\pi} \le b/a_0 \le \frac{4}{\pi}\frac{a}{a_0} \\ \widehat{\overline{\sigma}}_{po} = \sqrt{\frac{9\sqrt{3}\pi}{32\Sigma_0 \widehat{a}}} = \frac{1}{\sqrt{a/a_0}} \,. & b/a_0 > \frac{4}{\pi}\frac{a}{a_0} \end{cases} \tag{3.13}$$

The boundaries between these regimes should be interpreted as asymptotic crossovers rather than sharp physical discontinuities. In the real cohesive-zone problem, the transition from confined-layer behaviour to half-plane behaviour is smooth: as b/a increases, the influence of the rigid lower boundary progressively disappears and the stored elastic energy becomes controlled by the contact edge rather than by the through-thickness deformation of the layer. Thus, $b_1 = 4a/\pi$ is not a strict material threshold, but the thickness at which the thin-layer energy-release estimate becomes comparable with the half-plane Griffith estimate. The piecewise form above is therefore best understood as an engineering envelope identifying the dominant mechanism in each limit.

3.3.2 Limiting solutions for a viscoelastic layer

Let us assume that the layer is constituted by a viscoelastic material with relaxed Young modulus E_0 and instantaneous Young modulus E_∞ so that $k = E_0/E_\infty$. In the limit of very slow/very fast unloading rate the substrate behaves as elastic. Thus, for the case of no friction between the substrate and the layer, according to Eq. (3.9),

one can anticipate the following two scenarios

$$\begin{cases} \overline{\sigma}_{po} = \sqrt{\frac{2E_0^*\Delta\gamma}{b}}\,, & \text{“very slow”} \\ \overline{\sigma}_{po} = \sqrt{\frac{2E_\infty^*\Delta\gamma}{b}}\,, & \text{“very fast”} \end{cases} \tag{3.14}$$

or in dimensionless form

$$\begin{cases} \widehat{\overline{\sigma}}_{po} = \sqrt{\frac{4}{(b/a_0)\pi}}\,, & \text{“very slow”} \\ \widehat{\overline{\sigma}}_{po} = \sqrt{\frac{4}{k(b/a_0)\pi}}\,, & \text{“very fast”} \end{cases} \tag{3.15}$$

where, one should notice that for rapid unloading (very fast scenario) the pull-off stress will reach the cohesive strength by the following value of the substrate thickness:

$$b_{0\infty} = \frac{4a_0}{k\pi}\,, \tag{3.16}$$

However, for a thick layer, the halfplane limit will be always obtained at $b_1 = 4a/\pi$, irrespective of the unloading rate. Figure 3.3 schematically displays the elastic limits at low and high retraction speed that constitute the bounds for the possible viscoelastic solutions.

Form Eq.s (3.11) and (3.16) it follows that if $a/a_0 < E_\infty/E_0$ then $b_{0\infty} > b_1$. In other words, if $a < a_0/k$ at a high enough retraction velocity, it is possible to reach the adhesive strength of the interface. It is easy to find elastomers with $E_\infty/E_0 \simeq 10^3 \div 10^4$ [131]. This implies that punches with semiwidth a much larger than a_0 can still reach the theoretical interfacial strength if unloading is performed fast enough. Also, this holds for layer thickness. If we assume that the experiments with PDMS in Peng et al. [125] were conducted relatively slowly, when b_0 was of the order of 0.1 mm, then clearly $b_{0\infty}$ could reach very large values, provided the punch is also large enough. This peculiarity may be exploited in the future as a technique to improve/enhance interfacial adhesion in micro-structured interfaces by optimizing not only the micro-pillar geometry, but also the unloading protocols.

3.4 Numerical implementation of the adhesive viscoelastic contact problem

In this section, the numerical scheme used to solve the adhesive viscoelastic contact problem is introduced. We utilized the boundary element method, which necessitates the discretization solely of the interface. A similar code has been used in previous works for solving both adhesive elastic [132] and viscoelastic [122] axisymmetric

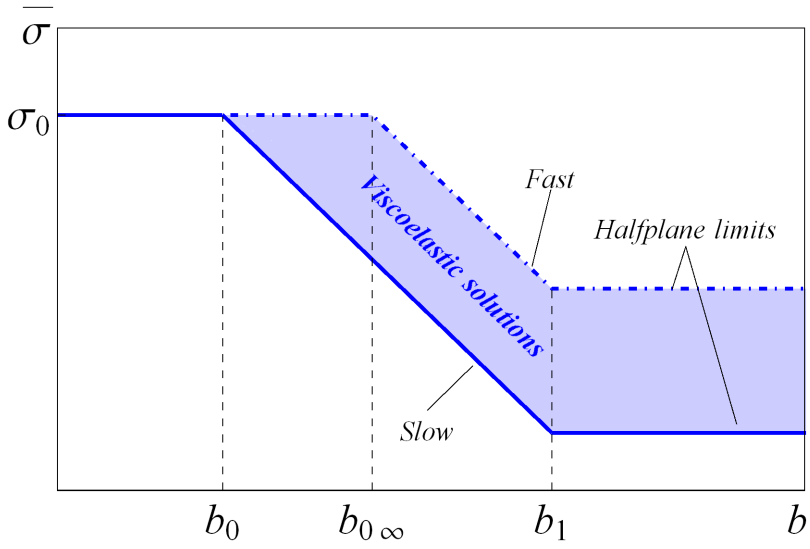

Figure 3.3: Schematic representation of the three possible detachment regimes. (From Ref. [18])

contact problems, therefore, in this section, we will focus on the essential adaptations required to tailor the implementation for a plane viscoelastic strip.

The flat punch interacts with the viscoelastic layer according to the Lennard-Jones 3-9 force-separation law defined as

$$\sigma\left(h\right)=\frac{8\Delta\gamma}{3h_0}\left[\left(\frac{h_0}{h}\right)^3-\left(\frac{h_0}{h}\right)^9\right]\ , \tag{3.17}$$

where σ is the traction ($\sigma>0$, when it is tensile), h is the interfacial gap and h_0 is the equilibrium distance. The theoretical strength of the interface (maximum tensile stress) is then equal to $\sigma_0=\Delta\gamma/(\alpha_{LJ}h_0)$ and takes place at a separation equal to $h=3^{1/6}h_0$. The gap is a function of the in-plane coordinate x as

$$h(x)=-\delta+h_0+v\left(x\right)\ , \tag{3.18}$$

where, $v\left(x\right)$ is the deflection of the viscoelastic layer with respect to the origin $(0,0)$ ($v\left(x\right)$ is positive as shown in Fig. 3.2). Here, Eq. (3.18) is solved numerically in a discrete manner at the $N=M+1$ nodes, being M the number of equally spaced elements with the length of $c=2a/M$. Following Bentall and Johnson [133] we implemented the method of overlapping triangles, i.e. for the n-th node the pressure is 0 at node x_{n-1}, rises linearly to p_n at node x_n and then falls linearly to 0 at node x_{n+1}, which gives overall a linear variation of the contact pressure $p\left(x\right)$ over the considered domain. With respect to the case of constant pressure elements, a piecewise-linear distribution of normal tractions produces a displacement field which

is everywhere smooth and continuous. Hence, according to Bentall and Johnson [133] the vertical deflection at node m of an elastic layer relatively to the origin $(x, y) = (0, 0)$ due to a triangular distribution of pressure centered in x_n is

$$v_m = aB\frac{4}{\pi E^*}\left[I_{A0} + I_A\left[m-n\right] + 4zI_{AR}\left[m-n\right]\right]p_n \ , \tag{3.19}$$

where $\{m, n\}$ are integers numbers, p_n is the pressure acting on the n-th node determined using Eq. 3.17 ($p_n > 0$ when it is tensile), $B = b/a$, $z = c/4b = 1/2BM$ and I_{A0}, I_A, I_{AR} are the following integral functions[1]

$$I_{A0} = \frac{2}{z}\int_0^\infty \left(\frac{1-\cosh\beta}{\beta+\sinh\beta}\right)\frac{\sin^2(\beta z)}{\beta^3}d\beta \ , \tag{3.20}$$

$$I_A\left[m-n\right] = -\frac{4}{z}\int_0^\infty \left(1+\frac{1-\cosh\beta}{\beta+\sinh\beta}\right)\frac{\sin^2(\beta z)}{\beta^3}\sin^2\left(\beta z\left(m-n\right)\right)d\beta \ , \tag{3.21}$$

$$I_{AR}\left[m-n\right] = \int_0^\infty \frac{\sin^2(\eta)\sin^2\left(\eta\left(m-n\right)\right)}{\eta^3}d\eta, \qquad \eta = \beta z \ . \tag{3.22}$$

By applying the superposition principle, the normal deflection v_m at node m due to a piecewise linear distribution of pressure can be written as

$$v_m = \frac{1}{E^*}\sum_{n=1}^{N} G_{mn}p_n, \tag{3.23}$$

where each column of the compliance matrix $\{(1/E^*)\overline{\overline{G}}\}_{NxN}$ corresponds to the displacement field due to a unity triangular pressure centered at node n being all the other nodes unloaded. Therefore, the displacement field and, correspondingly, the compliance matrix can be readily computed using Eq. (3.19). Once the elastic solution is obtained, the displacement field of the viscoelastic layer $v(x,t)$, can be determined by the elastic-viscoelastic correspondence principle in the form of Boltzmann integrals [134] as

$$v(x,t) = \frac{1}{E_0^*}\int G(x,s)\int_{-\infty}^{t} c(t-\tau)\frac{dp(s,\tau)}{d\tau}d\tau ds \ , \tag{3.24}$$

where $c(t)$ is the dimensionless creep compliance function, the strain variation after an application of a constant unit stress, and, in our discrete formulation, the Green function $G(x,s)$ is replaced by the appropriate tensor $\{\overline{\overline{G}}\}_{NxN}$, so that the viscoelastic

[1]Care should be taken when integrating I_{A0} which converges slowly. The Appendix 3 of Bentall and Johnson [133] suggests a convenient integration strategy we have also adopted. Notice that Bentall and Johnson [133] contains a misprint as the second part in which I_{A0} is split up should be integrated over the interval $[\delta, +\infty]$.

nodal displacements $\{v(t)\}_{Nx1}$ at time t are

$$\{v(t)\}_{Nx1} = \{\overline{\overline{G}}\}_{NxN} * \left\{ \frac{1}{E_0^*} \int_{-\infty}^{t} c(t-\tau) \frac{dp}{d\tau} d\tau \right\}_{Nx1}, \tag{3.25}$$

where the symbol "$*$" stands for the row by column product. For the linear viscoelastic material, the standard model is assumed with a single relaxation time τ, composed by a spring placed in series with an element constituted by a dashpot and a spring in parallel (see Fig. 3.2), for which the dimensionless creep compliance function is as follows

$$c(t) = \left[1 + (k-1) \exp\left(-\frac{t}{\tau} \right) \right] . \tag{3.26}$$

being τ the relaxation time of the material. Hence, by using a sequential time-marching continuation, we solved Eq.s (3.17,3.18,3.25), where at each time step an iterative scheme is used to determine the equilibrium solution.

3.5 Results

Here the results of the numerical investigations are shown by using the following dimensionless parameters

$$\widehat{a} = \frac{a}{h_0}; \quad \widehat{\sigma}(x) = \frac{\sigma(x)}{\sigma_0}; \quad \widehat{\overline{\sigma}} = \frac{P}{2aL\sigma_0}; \quad \widehat{\delta} = \frac{\delta}{h_0}; \quad \widehat{t} = \frac{t}{\tau}, \tag{3.27}$$

and $\widehat{\overline{\sigma}}_{po}$ is the (dimensionless) average stress at pull-off and is defined as $\widehat{\overline{\sigma}}_{po} = \max(\widehat{\overline{\sigma}})$. If not stated differently, in our simulations we considered $M = 200$, $\Sigma_0 = 0.05$, and $k = 0.1$.

3.5.1 History dependence

Viscoelastic materials typically exhibit a "history-dependent" response and this tremendously affects the detachment force in Hertzian indenters [135, 136]. Hence, first we aimed to explore how different loading scenarios affect the detachment characteristics of the flat indenter we considered, while keeping the unloading rate constant. The simulations were carried out under displacement control using a trapezoidal function (see inset in Fig. 3.4.a) which main parameters are shown in Table 3.1. We define the dwell time as $\widehat{t}_{dwell} = \widehat{t}_2 - \widehat{t}_1$, the unloading rate $\widehat{r} = (\widehat{\delta}_{load} - \widehat{\delta}_{unload})/(\widehat{t}_3 - \widehat{t}_2)$, and the loading rate as $\widehat{r}_{load} = (\widehat{\delta}_{load} - \widehat{\delta}_0)/(\widehat{t}_1)$ with reference to the the inset of Figure 3.4.a. We endeavored to investigate the impact of different loading protocols meticulously although the unloading curves presented

Table 3.1: Description of parameters governing the loading protocols for the curves presented in Figs. 3.4 and 3.5 .

Loading protocol	$\widehat{\delta}_0$	$\widehat{\delta}_{load}$	$\widehat{r}_{load}$	$\widehat{r}$	$\widehat{t}_{dwell}$
# 1	1	1	very fast	10	0
# 2	1	1	very slow	10	0
# 3	0	1	5	10	0
# 4	2	2	very fast	10	0
# 5	2	2	very slow	10	0
# 6	0	2	5	10	0

in Figure 3.4 are restricted to the six different protocols described in Table 3.1.

These loading scenarios included: (i) Unloading from a fully relaxed substrate after a slow loading process, indicated by the black curves (2,5). (ii) Unloading following rapid loading, causing the substrate to exhibit an elastic response with $E(t=0) = E_\infty$, as denoted by the blue curves (1,4). (iii) Unloading after indenting the substrate at a constant loading rate $\widehat{r}_{load} = 5$, represented by the red curves (3,6). It's important to note that while the loading phase is not shown for curves (1, 2, 4, 5), we accounted for the pre-loading effect in our simulations. Furthermore, the maximum indentation depth $\widehat{\delta}_{load}$ was kept at $\widehat{\delta}_{load} = 1$ for curves (1, 2, 3) (solid lines) and set to $\widehat{\delta}_{load} = 2$ for curves [4, 5, 6] (dashed lines). The punch has $a/a_0 = 64.85$, and the viscoelastic layer's (dimensionless) thickness is $B = b/a = 0.005$ which is equivalent to $\widehat{b}/\widehat{a_0} = 0.3242$.

The primary result from Fig. 3.4 is that, regardless of the significant variations in loading conditions, the magnitude of the pull-off stress remains consistent across various loading histories. Indeed, one can conclude that the pull-off stress remains nearly unaffected by the loading history. In Figure 3.4.b, we present the same curves as in Fig. 3.4.a, but with a shift in the horizontal axis by δ_P. This shift corresponds to the indentation depth at which the normal load vanishes during unloading. It helps to better observe the slight changes in the unloading trajectories. Furthermore a comprehensive investigation on the effect of the different loading scenario was conducted for various layer thicknesses. In Figure 3.5, we illustrate $\widehat{\overline{\sigma}}_{po}$ versus the variation in thickness b/a_0. The legend in Figure 3.5 clarifies that the plot presents results derived from all the loading conditions in Table 3.1, all with the same unloading rate. Remarkably, these plots closely overlap, indicating very similar values across the various simulations for all the thicknesses tested. To further quantify the distinctions between these loading cases, we examined the relative changes in pull-off stress with respect to one specific case that serves as the foundation for our subsequent investigations. The results are plotted in the inset of

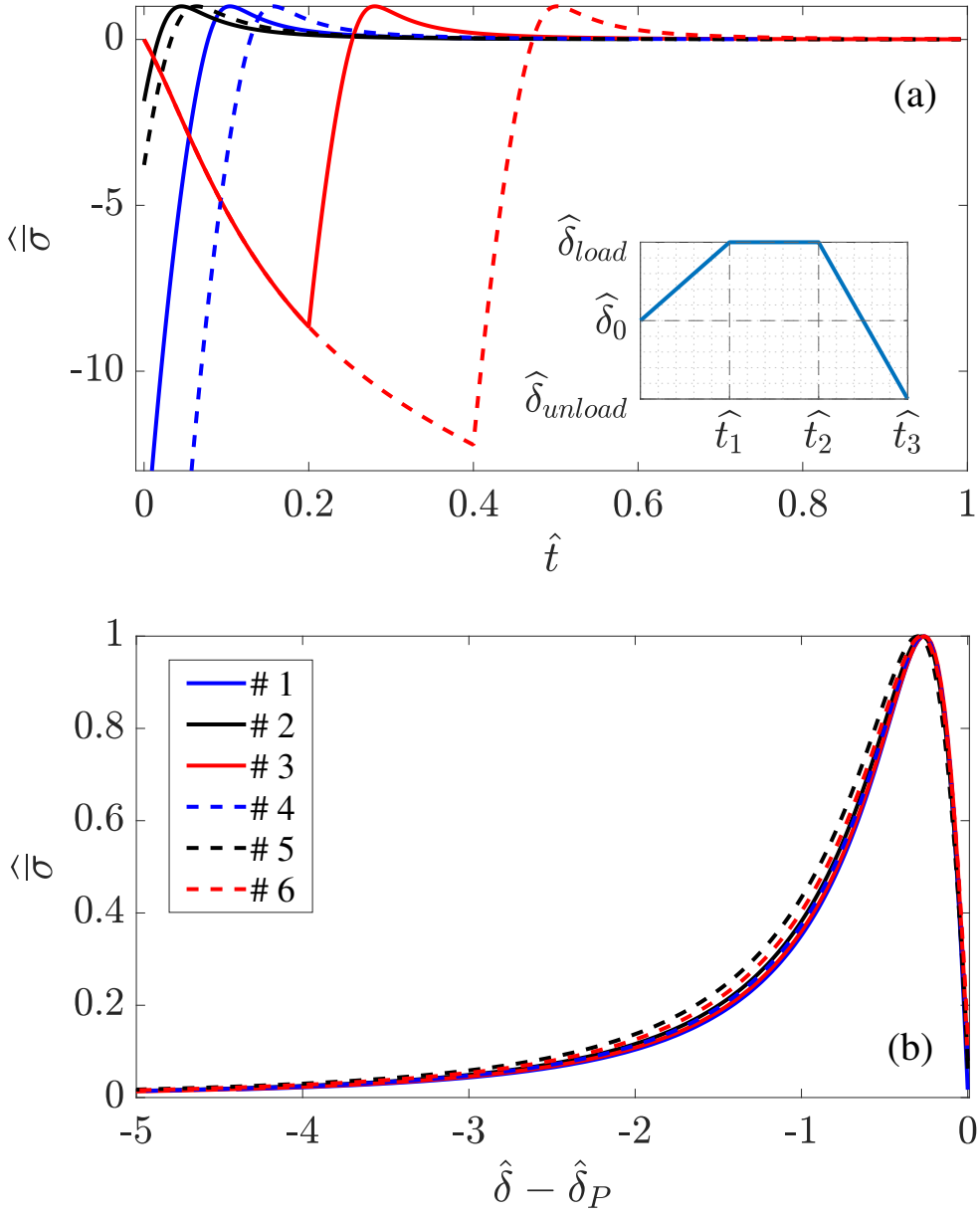

Figure 3.4: (a) Unloading curves for $\Sigma_0 = 0.05, k = 0.1$ and punch of radius $\widehat{a}/\widehat{a}_0 = 64.85$ from a fully relaxed viscoelastic surface with different loading protocols. (b) The identical curves displayed in (a) are reiterated here subsequent to a horizontal axis shift equal to $\widehat{\delta}_{P=0}$. (From Ref. [18])

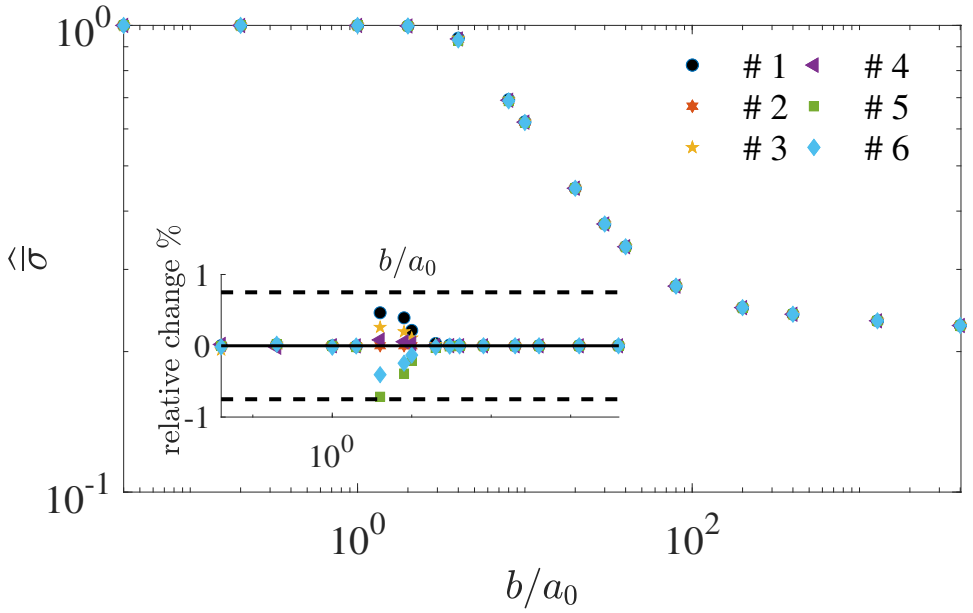

Figure 3.5: Normalized pull-off stress as a function versus the normalized layer's thickness for different loading protocols. (From Ref. [18])

Figure 3.5 as a relative change for various thickness values. It's evident that within a certain accuracy we can state that the detachment force of a flat indenter from a viscoelastic adhesive strip is *negligibly influenced by the loading history of the contact*. For the remainder of the paper we will consider unloading the viscoelastic strip from a fully relaxed condition, unless explicitly stated otherwise, we assume $\widehat{\delta}_0 = \widehat{\delta}^{load} = 1$, $\widehat{t}_{dwell} = 0$.

3.5.2 Dependence on the unloading rate

After establishing that the loading history does not influence the pull-off stress $\widehat{\overline{\sigma}}_{po}$, we examine how $\widehat{\overline{\sigma}}_{po}$ varies with respect to the layer thickness for four different unloading rates: $\widehat{r} = [0.1, 1, 10, 100]$ represented in Fig. 3.6 by black diamonds, green circles, red squares, and pink triangles, respectively. Figure 3.6 shows a comprehensive analyses for the punch semi-width $\widehat{a}/\widehat{a}_0 = 64.85$. The results are obtained starting from a fully relaxed substrate. For $b < b_0 \simeq 1.27a_0$, we reach the cohesive limit, where the pull-off stress remains independent on both the unloading rate and the layer thickness, approaching the theoretical value $\widehat{\overline{\sigma}}_{po} = 1$. Most importantly, for $b_0 < b < b_1$, the curves align well with the LEFM (Linear Elastic Fracture Mechanics) solution we have derived in Section 3.3 showing a scaling of $\propto b^{-1/2}$. Here, the pull-off stress increases with the unloading rate, and the pull-off data consistently stay well by the "slow" and "fast" limits we derived, represented by the blue dashed

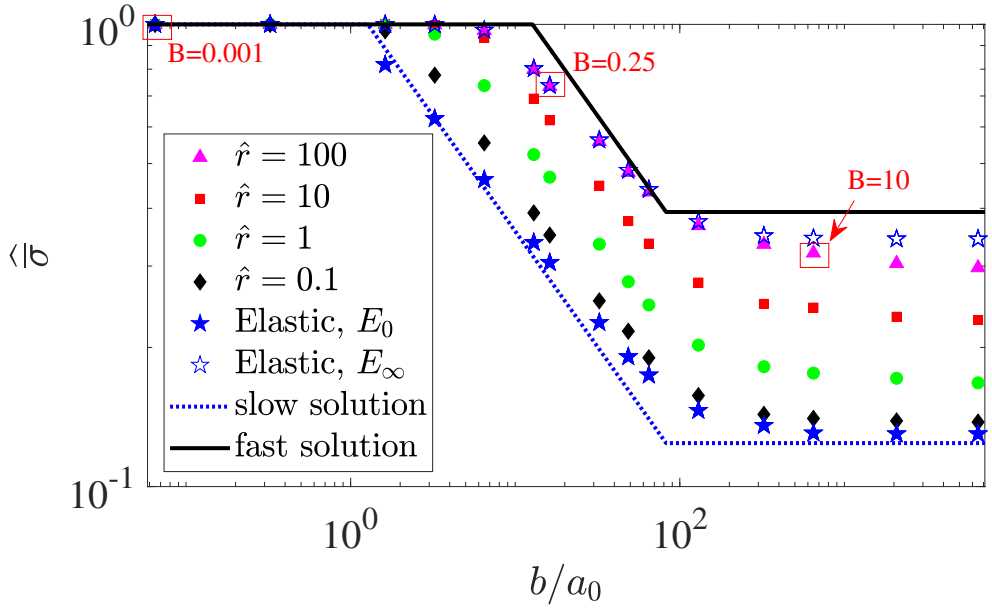

Figure 3.6: Normalized pull-off stress as a function of the normalized layer's thickness for different unloading rates of a punch with $\widehat{a}/\widehat{a}_0 = 64.85$. (From Ref. [18])

and solid black lines, respectively. For a thickness larger than b_1 the curves align with the half-plane solution and, for a given unloading rate, the pull-off stress remains constant independently on the layer thickness.

Notice that in the theoretical elastic solution the detachment happens with no propagation ($a_c = a$, being a_c the semi-width of the crack ligament). Clearly, this condition is never achieved in a more refined cohesive zone model, as it is the one we have implemented numerically. This accounts for the small deviations we found in the limiting case of very fast and very slow unloading between numerical and theoretical results. Nevertheless, to ascertain the correctness of the numerical viscoelastic results, the plots also include the curves obtained unloading an *elastic* strip with modulus E_0 (filled blue stars) and E_∞ (empty blue stars). One easily recognizes that the viscoelastic solutions are perfectly bounded between the two limiting elastic cases.

To support our conclusion we focus on the mechanism of crack propagation and stress distribution at the interface from the unloading onset up to pull-off. Figures 3.7 show the stress distribution for three specific cases out of the 120 cases shown in Fig. 3.6. All the cases are for unloading rate $\hat{r} = 100$. The punch radius in Figure 3.7 is $\widehat{a}/\widehat{a}_0 = 64.85$. The corresponding points for these three cases are highlighted with red squares in Fig. 3.6. According to Fig. 3.7, during unloading, the crack propagates at the interface hence the semi-width of the crack ligament a_c is smaller than the punch semi-width a when pull-off happens. This explains the difference between the expected pull-off stress from the analytical limits and the actual pull-off

stress.

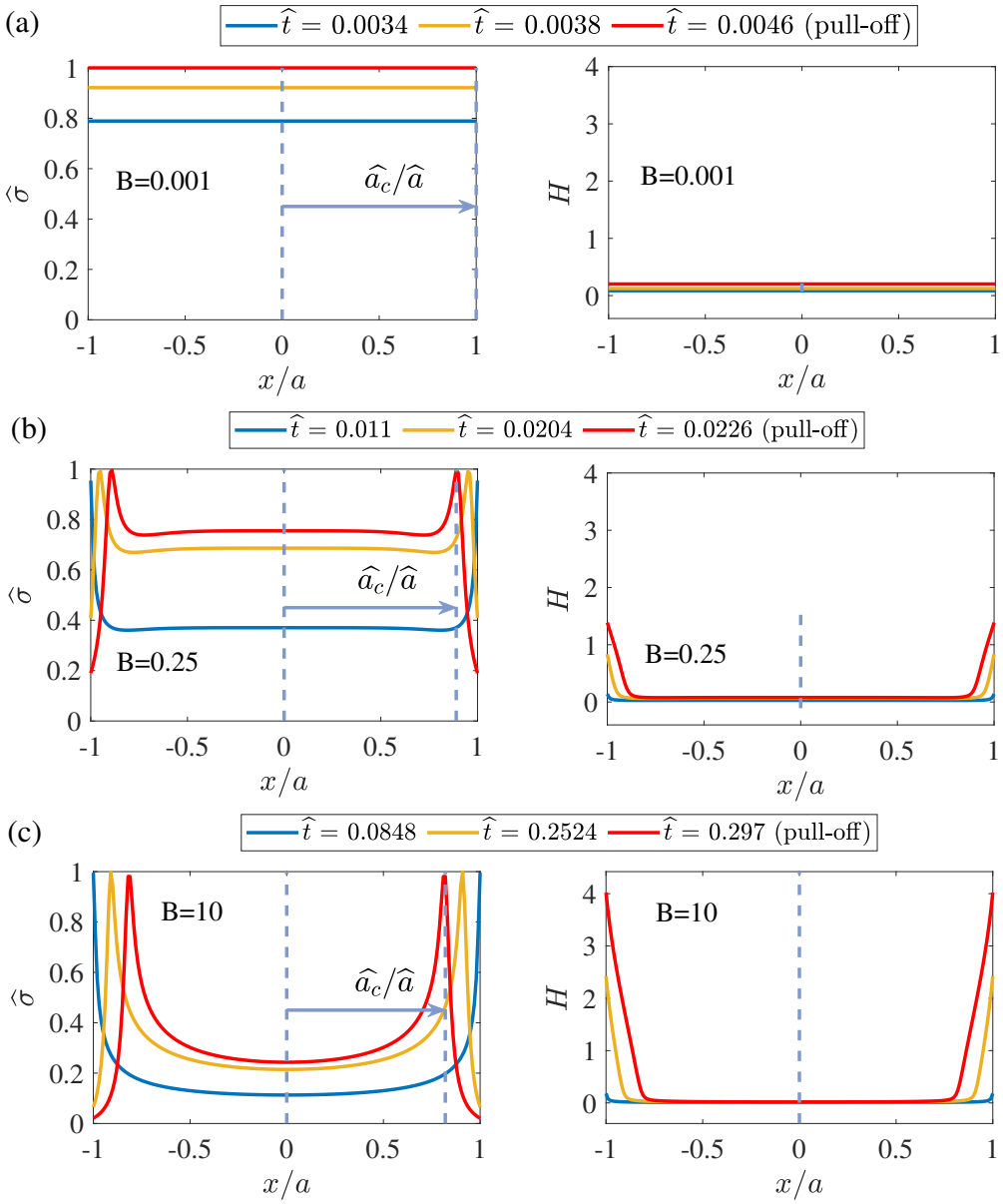

Figure 3.7: Gap function (the right plots) and the stress distribution (the left plots) on the surface of a layer with parameters $\Sigma_0 = 0.05$, $k = 0.1$, and $\widehat{a}/\widehat{a}_0 = 64.85$ are presented for various geometries: (a) $B = 0.001$, (b) $B = 0.25$, and (c) $B = 10$, all under an unloading rate of $\widehat{r} = 100$. Each plot displays results for three different moments, with pull-off data highlighted in red. (From Ref. [18])

Figure 3.7 displays three distinct cases with different values of B (0.001, 0.25, and 10), denoted as Figures 3.7a, 3.7b, and 3.7c, respectively. Figure 3.7a pertains to the cohesive zone, where the detachment occurs at $a_c \simeq a$ and with a uniform distribution of tensile tractions at the interface. For a more comprehensive understanding of

crack propagation and the detachment process, we have included gap plots on the right side of Figure 3.7. These plots represent the gap $H(x) = h(x)/h_0 - 1$ between the rigid punch and the viscoelastic layer as a function of the in plane coordinate x. Figure 3.7a illustrates that in the cohesive region the gap is uniformly distributed at the interface, with no crack formation. This is, in fact, the reason why we can achieve $\widehat{\overline{\sigma}}_{po}$ numerically with the same results as the expected analytical results (see Figure 3.6 for $B = 0.001$). In contrast, for the other two cases, as depicted in Figures 3.7b and 3.7c, we observe crack propagation, with detachment occurring at $a_c < a$. Notably, for larger values of B, a reduction in the ratio a_c/a is evident, resulting in the small deviation observed in Fig. 3.6 between the numerical and the analytical results.

The finite-thickness effect can be interpreted mechanically as a change in how elastic energy and viscoelastic dissipation are distributed during unloading. For thick layers, deformation is concentrated near the receding contact edge and detachment remains crack-like, so the response approaches the half-plane fracture-mechanics picture. When the layer becomes thinner, the rigid backing constrains the deformation field through the thickness and the tensile stress becomes more spatially uniform below the punch. In this limit, the detachment tends toward nearly simultaneous decohesion over the contact area, as it is shown in Fig. 3.7. This explains why the pull-off stress may approach the cohesive strength while the effective surface-energy amplification remains bounded by geometry.

A more detailed view on the dependence of the pull-off stress on rate effects is shown in Fig. 3.8 that shows $\widehat{\overline{\sigma}}_{po}$ as a function of the crack speed at pull-off, defined as

$$V_c = -da_c/dt \ , \tag{3.28}$$

where a_c represents the crack ligament semi-width, which decreases as the crack propagates at the interface. The results are closely related to the interaction between adhesion and viscoelastic dissipation in the strip (see also [137]), indeed it represents one of the major objective of viscoelastic crack propagation theories [138–144]. Consequently, we conducted additional analyses to examine this effect. We selected four different cases with a punch radius of $\widehat{a}/\widehat{a}_0 = 64.85$ and the corresponding thickness ratios of $\widehat{b}/\widehat{a}_0 = [3.24, 6.48, 12.97, 32.42]$, corresponding to the blue, orange, yellow, and purple curves, respectively. We conducted numerical experiments with 20 different unloading rates ranging from $\widehat{r} = 0.1$ to $\widehat{r} = 100$ to obtain curves representing a wide range of the dimensionless crack velocity $\widehat{V}_c = V_c\tau/h_0$ at pull-off. The analysis of Fig. 3.8 illustrates clearly the trend: thin layers and high retraction velocity favour high pull-off stress. Nevertheless, this effect is mitigated when the

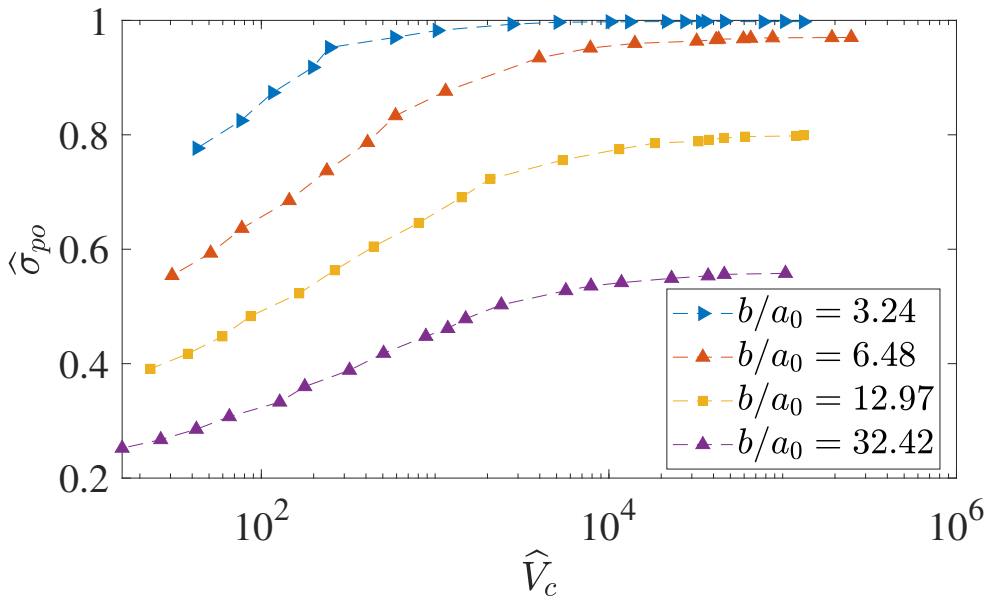

Figure 3.8: Normalized pull-off stress as a function of the normalized crack velocity at pull-off for four different values of b/a_0 for a punch with $\widehat{a}/\widehat{a}_0 = 64.85$ unloaded from a fully relaxed viscoelastic surface at different unloading rates. (From Ref. [18])

$b \approx a_0 \approx b_0$ as, in the cohesive region, the detachment tends to happen at a uniform stress.

Although, the pull-off force reduces increasing the layer thickness the enhancement in terms of effective surface energy remains the same when moving from low to high unloading rates, provided that $b > b_0$. Based on the thin layer elastic solution Eq. (3.9) we define the effective surface energy as

$$\Delta\gamma_{eff} = \frac{\overline{\sigma}_{po}^2 b}{2E_0^*}\left(\frac{a}{a_c}\right)^2 \tag{3.29}$$

where we considered that in general the detachment happens at $a_c < a$. Hence, in dimensionless form,

$$\widehat{\Delta\gamma}_{eff} = \frac{\Delta\gamma_{eff}}{\Delta\gamma_0} = \frac{\widehat{\overline{\sigma}}_{po}^2 \Sigma_0 \widehat{b}}{2\alpha_{LJ}}\left(\frac{\widehat{a}}{\widehat{a}_c}\right)^2 . \tag{3.30}$$

Fig. 3.9 shows that the normalized effective surface energy $\widehat{\Delta\gamma}_{eff}$ increases monotonically with respect to the crack velocity $\widehat{V}_c$ at pull-off up to a certain plateau value. In the case of $b/a_0 = 32.42$, the normalized effective surface energy reaches its theoretical upper limit $\widehat{\Delta\gamma}_{eff} = 1/k$ (all our simulations are for k=0.1). Notice that for any thickness of the layer larger than $b_{0\infty}$ one would get the maximum possible enhancement $1/k$. Care should be taken when interpreting the data using Eq. 3.30 as, if the latter is used for $b > b_1$ this may lead to unrealistic enhancements $\widehat{\Delta\gamma}_{eff}$,

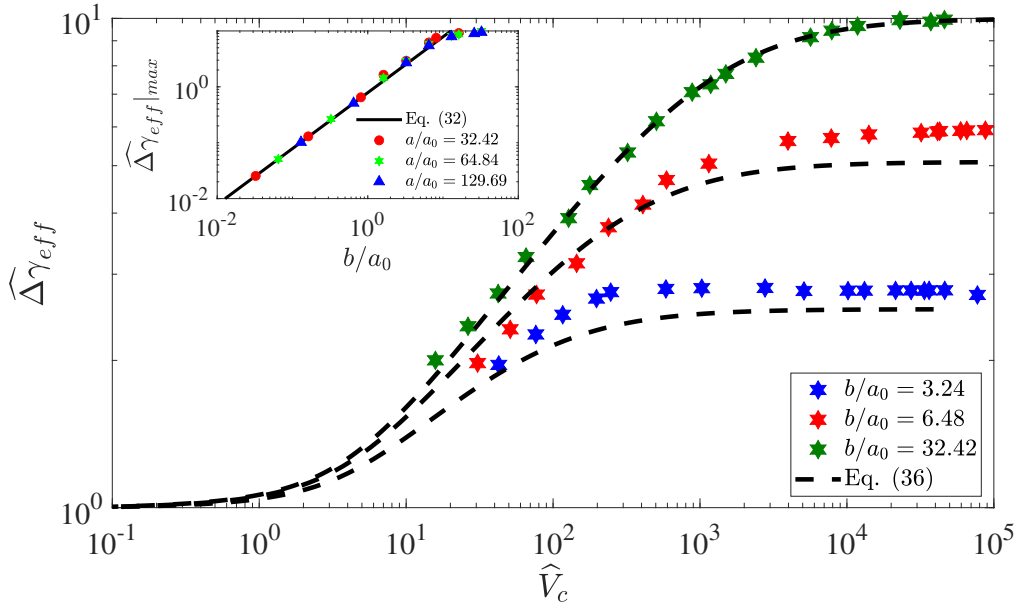

Figure 3.9: Normalized effective surface energy as a function of the crack velocity at pull-off for four different values of b/a_0 for a punch with $\widehat{a}/\widehat{a}_0 = 64.85$ unloaded from a fully relaxed viscoelastic surface at different unloading rates. Dashed lies are obtained with Eq. (3.35). Maximum enhancement for the dimensionless effective surface energy as a function of b/a_0. Inset: maximum enhancement of the effective surface energy obtained numerically at very high unloading rates for $a/a_0 = [32.42, 64.84, 129.69]$, respectively red circles, green stars, blue triangles. The solid black line shows the prediction of Eq. (3.31). (From Ref. [18])

which is due to the fact that for $b > b_1$ the halfplane solution should be considered.

It's important to note that, due to the finite size effect, for cases with $b < b_{0\infty}$, we observe the maximum enhancement of the normalized effective surface energy to be lower than $1/k$. This happens because, for the very thin layer, the cohesive region is approached, namely the DMT-type failure rather than the JKR-type, in the Peng et al. [125] terminology. In the latter case, if we assume $\widehat{\bar{\sigma}}_{po} = 1$, and $\widehat{a} = \widehat{a}_c$, and with the acquisition of Eq. (3.5), one can obtain the following relation for the maximum enhancement that can be reached at high retraction rates

$$\widehat{\Delta\gamma}_{eff}|_{max} = \left(\frac{\pi}{4}\right)\left(\frac{b}{a_0}\right), \tag{3.31}$$

which turns out to be solely dependent on the ratio b/a_0. In order to validate our upper bound enhancement factor (Eq. (3.31)), we considered three distinct values of punch semi-width a/a_0, on fully relaxed viscoelastic substrate with varying b/a_0 ratios, unloaded at a high unloading rate $\widehat{r} = 100$. The inset of Fig. 3.9 shows that the maximum enhancement obtained numerically compared very well with Eq.

(3.31).

We incorporated this correction in Greenwood (2004) theory [12] for crack propagation in viscoelastic semi-infinite media, which, in its original form gives

$$\widehat{\Delta\gamma}_{eff} = \left[k + (1-k)\,\frac{\alpha}{2}\int_0^1 H(\xi)\exp\left(-\alpha\,(1-\xi)\right)d\xi\right]^{-1} \tag{3.32}$$

where

$$H(\xi) = 2\xi^{1/2} - (1-\xi)\ln\left(\frac{1+\xi^{1/2}}{1-\xi^{1/2}}\right) \tag{3.33}$$

$$\alpha = \frac{\pi}{4\Sigma_0}\frac{\widehat{\Delta\gamma}_{eff}\alpha_{LJ}}{\widehat{V}_c} \tag{3.34}$$

Equation (3.32) for very slow propagation gives $\widehat{\Delta\gamma}_{eff} = 1$, while at high speed provides the maximum enhancement $\widehat{\Delta\gamma}_{eff}\Big|_{\max} = 1/k$. This picture, on which all present theories agree, is valid for semi-infinite solids, nevertheless, in agreement with recent results [122, 135, 136], we have found that due to finite size effects the maximum enhancement may be consistently reduced. For the present problem, if $b < b_{0\infty}$, the maximum enhancement will be given by $\widehat{\Delta\gamma}_{eff}\Big|_{\max} = (\pi/4)\,(b/a_0)$, so we propose here a generalization of Eq. (3.32) for $b_0 < b < b_{0\infty}$

$$\widehat{\Delta\gamma}_{eff}\left(\widehat{V}_c, \frac{b}{a_0}\right) = \left[\frac{4}{\pi\,(b/a_0)} + \left(1 - \frac{4}{\pi\,(b/a_0)}\right)\frac{\alpha}{2}\int_0^1 H(\xi)\exp\left(-\alpha\,(1-\xi)\right)d\xi\right]^{-1} \tag{3.35}$$

where we have explicitly indicated that now the velocity dependent effective surface energy depends not only on the crack speed, but also on the ratio between the layer thickness and the fracture length a_0. Notice that for $b > b_{0\infty}$ Eq. (3.32) remains valid, while for $b < b_0$ the effective energy is velocity *independent* and equal to $\widehat{\Delta\gamma}_{eff}\Big|_{\max} = (\pi/4)\,(b/a_0)$. Figure 3.9 compares the predictions obtained with the finite size Greenwood model (Eq. (3.35)) against the numerical results, which are found in fairly good agreement. This result (Eq. (3.31)), obtained with the more general cohesive-based theory, could also be used to correct the theory of Persson-Brener (2005) [142] and Persson (2017) [143], as we shall do in Appendix II.

One important parameter to examine is the work of separation, which is defined as

$$\widehat{w}_{sep} = \frac{w_{sep}}{2aL\Delta\gamma_0} = \int_{\widehat{\delta}_P}^{\infty}\widehat{\overline{\sigma}}\,d\widehat{\delta}\,. \tag{3.36}$$

which indicates the energy spent during the unloading phase to separate the contact. We calculated this parameter for four different layer thicknesses, specifically $b/a_0 =$

[3.24, 6.48, 12.97, 32.42], which corresponds to the blue, orange, yellow, and purple curves in Fig. 3.10. Similarly to previous research works [122, 135, 136] the $\widehat{w}_{sep}$ has a typical bell shape; at low and high velocity there is little energy expenditure to separate the contact as the material behaves essentially as elastic, but for intermediate regimes $\widehat{w}_{sep}$ presents a maximum related to the dissipative phenomena happening in the viscoelastic layer.

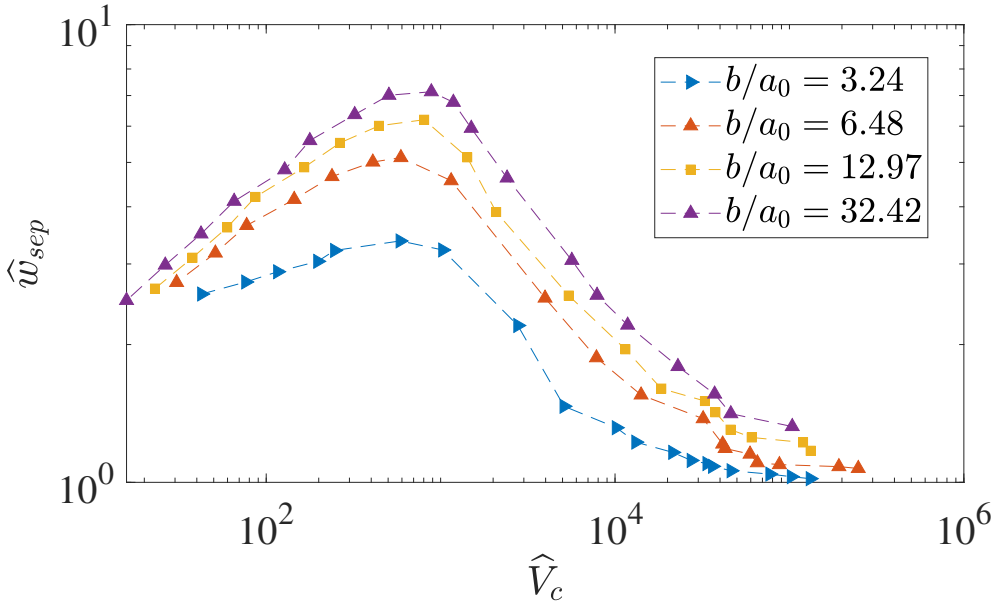

Figure 3.10: Normalized work of separation as a function of the crack velocity at pull-off for four different values of b/a_0 for a punch with $\widehat{a}/\widehat{a}_0 = 64.85$ unloaded from a fully relaxed viscoelastic surface at different unloading rates. (From Ref. [18])

3.6 Summary of findings

The plane problem of the detachment of a large flat punch from an adhesive viscoelastic layer of finite thickness b has been studied. First, we have derived an elastic model based on the "thin strip" assumption by Johnson [126]. It was found that the pull-off stress decays as $\propto 1/\sqrt{b}$. Nevertheless, this functional dependence is bounded (i) for very thin layer by the cohesive limit where the pull-off stress equals the theoretical stress of the material, (ii) for very thick layer by the halfplane limiting solution. The elastic model provided the bounds for the viscoelastic analysis. We found that if the layer is thin, particularly at high enough retraction velocity, the theoretical limit of the material could be reached. This turns particularly interesting as for soft polymers E_∞/E_0 may easily be of the order of $10^3 \div 10^4$ and this amplifies the layer thickness for which the theoretical strength can be observed. Clearly, this behavior

will be hindered by the fact that during unloading the crack starts to propagate at the interface hence, at pull-off, the actual crack ligament a_c is smaller than the punch semi-width.

Theoretical predictions have been compared with boundary element numerical simulations for a standard linear viscoelastic material and using a Lennard-Jones force-interaction law. We have shown that the loading conditions have a negligible effect on the pull-off force, in contrast with what was shown for a Hertzian geometry. Instead, the pull-off force consistently increases with the unloading rate up to a certain plateau given by the cohesive strength of the interface.

Finally, we have shown that when the data are represented in terms of effective surface energy, at high velocity the theoretical enhancement given by E_∞/E_0 is reached only when the layer thickness is larger than a characteristic lengthscale $b_{0\infty}$. For $b_0 < b < b_{0\infty}$ the maximum adhesion enhancement is limited by finite size effect and in particular we found $\widehat{\Delta\gamma}_{eff}|_{\max} = (\pi/4)\,(b/a_0)$. Hence, we have proposed an extension of Greenwood and Persson crack propagation theories accounting for finite size effects which we found in good agreement with numerical results.

Chapter 4

Adhesion in Broad-Band Viscoelastic Hertzian Contacts

Publication note. The work presented in this chapter led to the peer-reviewed paper published in *Journal of the Mechanics and Physics of Solids* [19].

This chapter extends the thesis from flat-punch detachment to Hertzian contact in broad-band viscoelastic materials, where geometry, pre-load effect, bulk dissipation, and crack-like separation interact more. It introduces the modified power-law constitutive model, develops analytical and numerical descriptions of rate-dependent adhesion, and tests their validity against experiments. The chapter thereby establishes the main mechanics framework on which the later surrogate models are built.

4.1 Introduction

To precisely assess adhesion in soft polymers (silicone, rubber), the properties of the viscoelastic material need to be characterized. Several numerical and experimental works have tried to accurately determine the viscoelastic material response in the time domain [145–148], in the frequency domain [149, 150] or using big data analysis and machine learning algorithms [151, 152]. All the approaches reveal that real rubbers and elastomers have to be characterized over a very wide range of frequencies which typically spans many orders of magnitude of the exciting frequency (broad-band behavior). This behavior plays a crucial role in determining the bulk dissipation, hence the interfacial adherence force.

Here we shall consider the problem of a rigid sphere of radius R that is unloaded from a fully relaxed broad-band viscoelastic adhesive half-space (see Fig. 4.1) presenting and comparing numerical, analytical and experimental results. A few recent works [16, 153, 154] have focused on the problem of the adhesion of a rigid Hertzian indenter unloaded from a viscoelastic substrate describing the material either by using (i) the classical three-element solid, also known as the Standard Linear Solid "SLS" (a spring in series with an element constituted by a dashpot and a spring in parallel), [16, 154, 155] or (ii) by considering the measured response spectrum of the viscoelastic material used in the experimental campaign [21, 153, 154]. The limitation of the first approach is that the SLS has a narrow-band behavior, hence, although providing valuable insights, it will be rarely useful for modeling the behavior of a real material. The limitation of the second approach is that the results obtained solve only the specific problem considered and it is difficult to draw general conclusions.

The objectives of this chapter are: (i) to define a material model which may be effectively and efficiently used for describing a real material viscoelastic behavior with a minimal number of constants in both the time and frequency domain, (ii) to determine, for the case of rigid Hertzian indenter-viscoelastic halfspace contact (see Fig. 4.1), how the broad-band material behavior influences the maximum adherence force as a function of the unloading rate (which is not the speed of the contact radius change, as we shall see) and of the preload, (iii) to provide closed form results for the effective surface energy $\Delta\gamma_{eff}$ based on the Persson and Brener [13] theory which allows to faithfully reproduce the numerical results together with their region of validity, (iv) to validate the proposed approach by comparing the numerical results with experimental data.

The remainder of the chapter is structured to address each objective outlined earlier: Section 4.2 provides a detailed description of the modified power law model used to characterize the viscoelastic material response; Section 4.3 presents, the

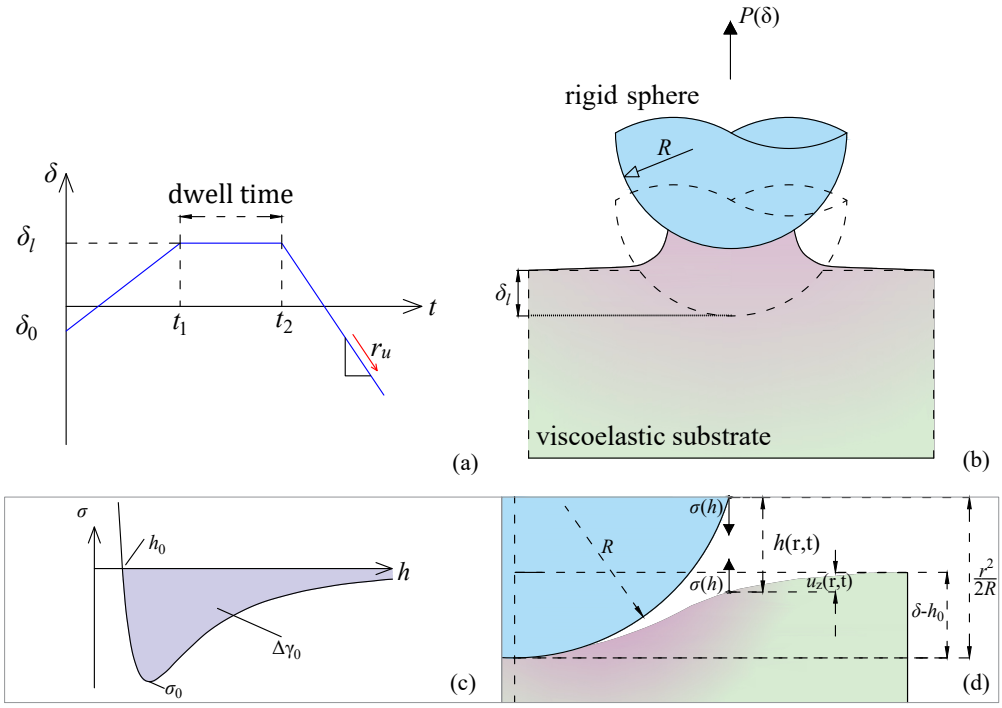

Figure 4.1: (a) The displacement-based loading protocol (pre-loading, dwelling, and unloading); (b) indentation phase (dashed) and unloading phase at a constant retraction rate; (c) Lennard-Jones adhesive stress $\sigma(h)$ as a function of the interfacial gap h; (d) geometric components of the gap function $h(r,t)$: indentation δ, equilibrium distance h_0, parabolic indenter profile $r^2/(2R)$, and viscoelastic deflection $u_z(r,t)$. From Ref. (From Ref. [19])

Boundary Element Model developed for analyzing the adhesive contact problem along with extensive numerical results; Section 4.5 introduces the developed analytical solution and demonstrates its applicability in characterizing adhesive contact problems; Section 4.6 focuses on the validation of the numerical results based on experimental outcomes; Section 4.7 discusses the presented results in light of the recent Literature; the chapter closes with the “Conclusions", Section 4.8.

4.2 Modified power law model

The challenge behind the mechanical modeling of viscoelastic materials arises because the mechanical response at time t depends on the contact history. Viscoelastic materials can be characterized in the frequency domain. If a sinusoidal stress $\sigma(\omega)$ at frequency ω is applied to a viscoelastic specimen the resulting harmonic strain $\varepsilon(\omega)$ will be delayed by a certain amount δ, hence the so-called complex modulus

$\overline{E}(\omega) = \sigma(\omega)/\varepsilon(\omega)$ can be defined in the complex plane. Alternatively, in place of $\overline{E}(\omega)$ one may define its reciprocal, the $\overline{C}(\omega) = \varepsilon(\omega)/\sigma(\omega)$ which is the complex compliance.

One approach to reproduce the broad-band response spectrum of a real viscoelastic material [21, 156] is to move from a SLS material model, which is constituted by a spring in parallel with a single Maxwell element (a spring in series with a dashpot), to the so-called Wiechert model constituted by a spring in parallel with many Maxwell elements [11], so that several relaxation times can be included in the material representation. Very often the number of elements needed for a faithful representation gets large enough so that the model returns a very good representation of the material viscoelastic behaviour, but at the same time it makes it difficult to extract general conclusions, due to the large number of fitting parameters determined.

One option to overcome this difficulty is to rely on power law material models [13, 73, 147, 157, 158], which assume a certain power law function for the distribution of the relaxation times. For example Popov [157] proposes a model that is fully defined by 5 constants: the relaxed and glassy moduli, two characteristic times, and one exponent. Schapery [73] uses an approximation for the creep compliance function $C(t) = (M_e + M_1 t^{-p})^{-1}$ which includes only three material constants $\{M_e, M_1, p\}$ and can describe well the behavior for very long times while being less accurate in describing the short-time material behavior. Furthermore, Persson and Brener [13] consider a model where the retardation times are distributed as a power law in between two characteristic times and vanishes elsewhere.

In the following, we will consider and extend the Modified Power Law (MPL) material model introduced by Williams [72], which is fully defined by a minimal set of four parameters: the glassy E_∞ and the rubbery E_0 moduli, a single characteristic time τ_0 and one exponent n. Closed-form results in both time and frequency domains that can be readily used for real viscoelastic material characterization or as input in viscoelastic crack propagation theories are provided in Appendix III, while in the following the main results are reported.

The MPL model is used here as a reduced constitutive representation rather than as a replacement for a full generalized Maxwell fit when exact material identification over the entire frequency range is required. This concept has been used in different ways to characterize viscoelasticity [73, 147, 157, 158]. Its advantage is that it preserves the correct relaxed and glassy limits while introducing a single exponent n that controls the breadth of the relaxation spectrum. This makes it suitable for parametric mechanical interpretation and for coupling with crack-propagation theory. Its limitations should also be kept in mind: the formulation remains linear

viscoelastic, assumes thermorheological simplicity, and cannot by itself describe nonlinear damage, cavitation, chain pull-out, or other rate-dependent processes localized inside the fracture process zone.

For the MPL material, the following relaxation spectrum $H(\tau)$ is assumed,

$$H(\tau) = \left(\frac{E_\infty - E_0}{\Gamma(n)}\right)\left(\frac{\tau_0}{\tau}\right)^n \exp\left(-\frac{\tau_0}{\tau}\right) , \tag{4.1}$$

where $\{\tau_0, n\}$ are constants to be determined and $\Gamma(n)$ is the Gamma function. The substitution of Eq. (4.1) into Eq. (7) gives the complex modulus $\overline{E}(\omega) = E'(\omega) + \boldsymbol{i}E''(\omega)$:

$$\overline{E}(\omega) = E_0 + (E_\infty - E_0)\,\boldsymbol{i}\omega\tau_0 \exp(\boldsymbol{i}\omega\tau_0)\,\mathbf{E}_n(\boldsymbol{i}\omega\tau_0) , \tag{4.2}$$

where $\mathbf{E}_n(x)$ is the exponential integral function of order $n > 0$. Appendix III provides closed-form results for both the real $E'(\omega)$ and the imaginary parts $E''(\omega)$ of the complex modulus.

The relaxation function $R(t)$ is given by [72]:

$$R(t) = E_0 + \int_0^\infty \tau^{-1} H(\tau) \exp(-t/\tau)\, d\tau , \tag{4.3}$$

which, upon substitution of Eq. (4.1) gives a very simple form:

$$R(t) = E_0 + \frac{E_\infty - E_0}{(1 + t/\tau_0)^n} \tag{4.4}$$

or in dimensionless form

$$\widehat{R}\left(\widehat{t}\right) = 1 + \frac{1/k - 1}{\left(1 + \widehat{t}\right)^n} \tag{4.5}$$

being $\widehat{R} = R(t)/E_0$, $\widehat{t} = t/\tau_0$ and $k = E_0/E_\infty$, which shows that at a given dimensionless time $\widehat{t}$ the material relaxation depends only on the parameters $\{n, k\}$.

Similarly, we can assume a modified power law distribution for the retardation spectrum, as:

$$L(\tau) = \left(\frac{C_0 - C_\infty}{\Gamma(n)}\right)\left(\frac{\tau}{\tau_0}\right)^n \exp\left(-\frac{\tau}{\tau_0}\right) , \tag{4.6}$$

where $\{\tau_0, n\}$ are constants to be determined. Hence the complex compliance is (substitute Eq. (4.6) into Eq. (17)):

$$\overline{C}(\omega) = C_\infty + \frac{(C_0 - C_\infty)}{\boldsymbol{i}\omega\tau_0} \exp\left(-\frac{\boldsymbol{i}}{\omega\tau_0}\right) \mathbf{E}_n\left(-\frac{\boldsymbol{i}}{\omega\tau_0}\right) , \tag{4.7}$$

where $\mathbf{E}_n(x)$ is the exponential integral function of order $n > 0$, $C_0 = 1/E_0$ is the creep compliance in the rubbery limit and $C_\infty = 1/E_\infty$ is the creep compliance in the glassy limit. Notice that once $\overline{C}(\omega)$ is obtained, the complex modulus is also obtained as $\overline{E}(\omega) = 1/\overline{C}(\omega)$ and vice-versa. Appendix III reports closed form results for both the real $C'(\omega)$ and the imaginary part $C''(\omega)$ of $\overline{C}(\omega)$.

The creep compliance function $C(t)$ is given by (Williams, 1964):

$$C(t) = C_\infty + \int_0^\infty \tau^{-1} L(\tau) \left(1 - \exp\left(-t/\tau\right)\right) d\tau \ , \tag{4.8}$$

which, upon substitution of Eq. (4.6) into Eq. (4.8) gives:

$$C(t) = C_0 - 2\frac{(C_0 - C_\infty)}{\Gamma(n)} \left(\frac{t}{\tau_0}\right)^{n/2} \mathbf{K}_n\left(2\sqrt{\frac{t}{\tau_0}}\right) \ , \tag{4.9}$$

where $\mathbf{K}_n(x)$ is the modified Bessel function of the second kind. The dimensionless creep compliance function $\widehat{C} = C/C_0$ is

$$\widehat{C}\left(\widehat{t}\right) = 1 - 2\frac{(1-k)}{\Gamma(n)} \widehat{t}^{\,n/2} \mathbf{K}_n\left(2\sqrt{\widehat{t}}\right) \ , \tag{4.10}$$

which shows that at a given dimensionless time $\widehat{t}$ the material creep depends only on the parameters $\{n, k\}$.

In Section 4.6, we will show that Polydimethylsiloxane (PDMS, 10:1 resin to curing agent ratio) one of the most common silicone-based polymers used in soft contact mechanics [2, 159, 160] has a characteristic exponent at room temperature of $n \simeq 0.22$, which is close to what Williams [72] found for unfilled HC rubber. In Fig. 4.2, we illustrate the time evolution of the relaxation and creep compliance functions of MPL for different exponents n (solid black lines) alongside a comparison of the SLS viscoelastic behaviour (blue dashed lines). Fig. 4.2 shows that in order to obtain a behavior close to a standard material, we should set $n \approx 1.6$, which implies PDMS has a much broader spectrum with respect to the SLS. It is recalled that for a SLS the dimensionless creep compliance function is $\widehat{C}(\widehat{t}) = [1 + (k-1)\exp(-\widehat{t})]$.

4.3 The numerical model

Let us consider the problem of a rigid sphere of radius R that is unloaded from a fully relaxed viscoelastic adhesive half-space (see Fig. 3.2). To model the adhesive contact problem a numerical scheme based on the Boundary Element Method was implemented in the software MATLAB, together with a time marching algorithm, which follows the implementation by Papangelo and Ciavarella [24, 25]. In the

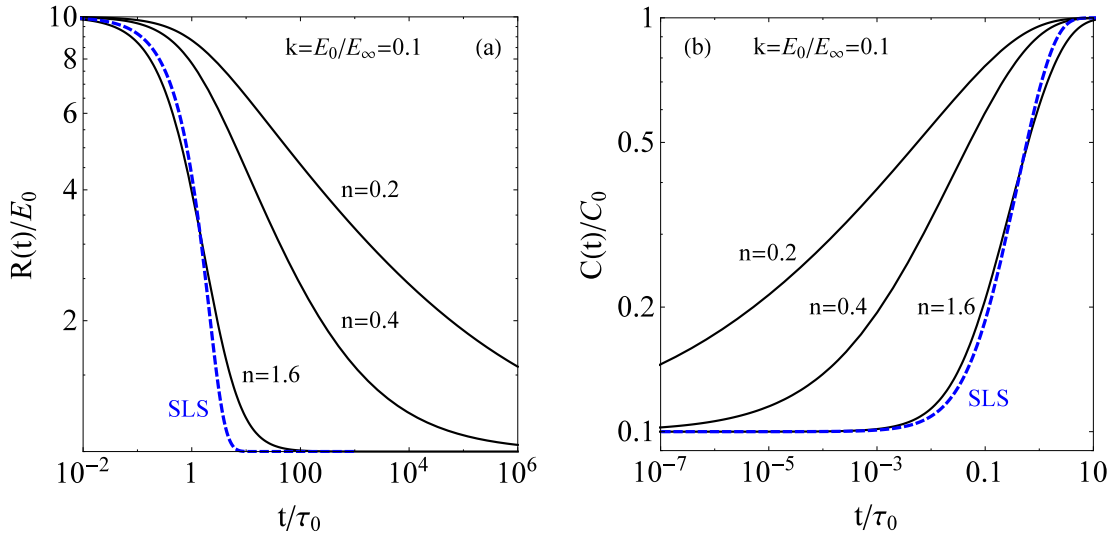

Figure 4.2: Time evolution of (a) the relaxation function $R(t)$ (Eq. 4.4), (b) the creep compliance function $C(t)$ (Eq. 4.9) for $n = [0.2, 0.4, 1.6]$ (solid black line) and a comparison with the behaviour of a SLS viscoelastic material (dashed blue line). From Ref. (From Ref. [19])

numerical model, it is assumed that the interaction between the sphere and the substrate is governed by a Lennard-Jones force-separation law [1]:

$$\sigma(h) = -\frac{8\Delta\gamma_0}{3h_0}\left[\left(\frac{h_0}{h}\right)^3 - \left(\frac{h_0}{h}\right)^9\right] , \tag{4.11}$$

where σ is the interfacial stress ($\sigma > 0$, when compressive), h the local gap, h_0 the equilibrium distance with the surface energy $\Delta\gamma_0 = \frac{9\sqrt{3}}{16}\sigma_0 h_0$. The gap function is then written as:

$$h(r,t) = -\delta + h_0 + \frac{r^2}{2R} + u_z(r,t) , \tag{4.12}$$

where $\delta > 0$ when the sphere approaches the viscoelastic half-space, the sphere profile is approximated by a parabola, and $u_z(r,t)$ is the deflection of the viscoelastic half-space, which depends on the loading history (we have explicitly shown the dependence of u_z on time t). The vertical deflections of the halfspace for an *elastic* axisymmetric problem are obtained as [68, 69]:

$$u_z(r) = \frac{1}{E_0^*}\int \sigma(s)\, G(r,s)\, sds , \tag{4.13}$$

where $G(r,s)$ is the Kernel function:

[1] Strictly speaking Eq. (4.11) would hold for infinite parallel planes, nevertheless in adhesive contact mechanics it is often assumed that Eq. (4.11) holds also for slightly inclined surfaces, which is the so-called "Derjaguin approximation", see [69].

$$G\left(r,s\right)=\begin{cases}\frac{4}{\pi r}K\left(\frac{s}{r}\right), & s<r\\ \frac{4}{\pi s}K\left(\frac{r}{s}\right), & s>r\end{cases} \tag{4.14}$$

$K\left(k\right)$ is the complete elliptic integral of the first kind of modulus k and $E_0^*=E_0/(1-\nu^2)$ is the composite elastic modulus (the sphere is rigid) being ν the Poisson ratio considered independent on the excitation frequency ω. Hence, according to the elastic-viscoelastic correspondence principle in the form of Boltzmann integrals [11], the normal displacements of the viscoelastic half-space $u_z(r,t)$ at time t, at position r will depend on the contact history as:

$$u_z(r,t)=\int G\left(r,s\right)s\int_{-\infty}^{t}C(t-\tau)\frac{d\sigma(s,\tau)}{d\tau}d\tau ds\ . \tag{4.15}$$

where the moduli in the creep compliance function $C(t)$ should be consider in the plane strain conditions, i.e. $C_0^*=1/E_0^*$. The gap function Eq. (4.12) is solved through a Newton-Raphson scheme on $N=M+1$ equally-spaced nodes, being M the number of interfacial elements so that Eq.s (4.11,4.12,4.15) are satisfied. To determine the half-space deflections Eq. (4.15) was discretized in time and space. In time, we used a time marching algorithm with a time step Δt. In space, we assumed the pressure distribution has a triangular shape over each element, i.e. for the element j-th the pressure is p_j at $r=r_j$ and falls linearly to 0 at $r=r_{j-1}$ and $r=r_{j+1}$, which is usually referred as the “method of the overlapping triangles" [161]. Further details of the numerical implementation can be found in Ref.s [24, 25].

The numerical prediction of pull-off in adhesive Hertzian contact is especially sensitive to spatial and temporal resolution, because the detachment instability is governed by a small cohesive zone near the contact edge and becomes increasingly demanding as the JKR limit is approached. For this reason, the numerical results should be interpreted together with the analytical consistency checks used throughout the chapter: recovery of the elastic limiting response, bounded behaviour between relaxed and glassy viscoelastic limits, agreement with Persson–Brener scaling in the range where its assumptions apply, and systematic trends with preload and unloading rate. Although a systematic full convergence map is not shown here, we conducted several numerical tests to ensure the accuracy of the numerical results as the parameter combination changes.

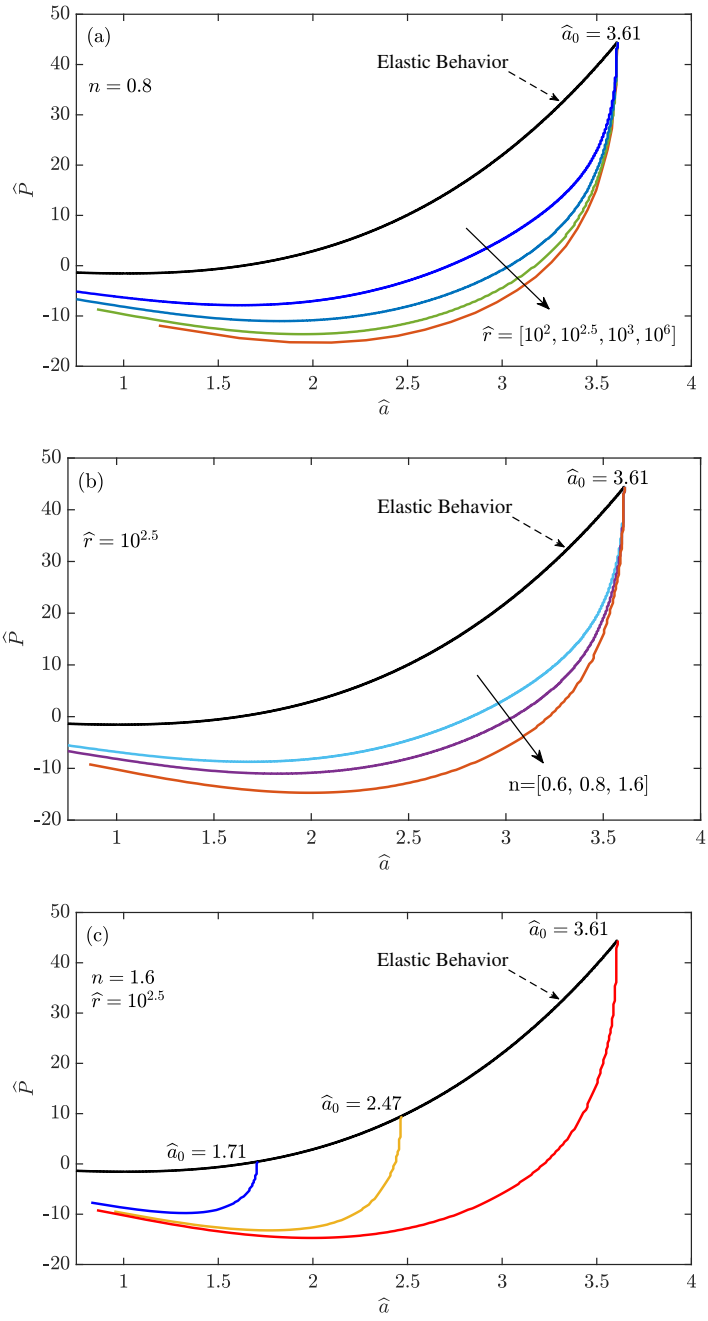

Figure 4.3: Dimensionless load $\widehat{P}$ versus the dimensionless contact radius $\widehat{a}$. (a) Material exponent $n = 0.8$, initial contact radius $\widehat{a}_0 = 3.61$, unloading rates $\widehat{r} = [10^2, 10^{2.5}, 10^3, 10^6]$; (b) initial contact radius $\widehat{a}_0 = 3.61$, unloading rate of $\widehat{r} = 10^{2.5}$ for different material exponents $n = [0.6, 0.8, 1.6]$; (c) initial contact radii $\widehat{a}_0 = [1.71,\ 2.47,\ 3.61]$, with a constant unloading rate of $\widehat{r} = 10^{2.5}$ and material exponent $n = 1.6$. For all the panels unloading starts from a fully relaxed substrate with $k = 0.1$ and $\mu = 3.24$. (From Ref. [19])

4.4 Numerical results

In the rest of the paper, unless differently stated, the numerical results will be presented in dimensionless notation, as follows:

$$\widehat{\delta} = \frac{\delta}{(\pi^2 \Delta\gamma_0^2 R/E_0^{*2})^{1/3}} \; ; \quad \widehat{a} = \frac{a}{(\pi R^2 \Delta\gamma_0/E_0^*)^{1/3}} \; ; \quad \widehat{P} = \frac{P}{\pi \Delta\gamma_0 R} \, , \tag{4.16}$$

being $\widehat{\delta}$ the dimensionless indentation, $\widehat{a}$ the dimensionless contact radius, $\widehat{P}$ the dimensionless normal load, $\widehat{P}_{po} = |\min\left(\widehat{P}\right)|$ the maximum detachment force, i.e. the pull-off force. Unless specified otherwise, our simulations employ $N = 500$ nodes. Let's consider a sphere with an initial contact radius of a_0 is unloaded from a fully relaxed viscoelastic substrate, with various unloading rates r. This unloading process mimics experimental conditions: (i) indenting the viscoelastic substrate to a specified depth (δ_{load}), (ii) allowing dwell time for substrate relaxation, then (iii) unloading at a constant velocity r. The corresponding dimensionless unloading rate is defined as $\widehat{r} = r\tau_0/h_0$. Unless differently stated, the results provided in the following will refer to the Tabor parameter [37] $\mu = \left(\frac{R\Delta\gamma_0{}^2}{E_0^{*2}h_0{}^3}\right)^{1/3} = 3.24$ and $k = E_0/E_\infty = 0.1$.

4.4.1 Dependence of the detachment force upon the loading protocol details

As it was discussed, the unloading rate r has a crucial role in the mechanical response of viscoelastic materials. We examined our model for different unloading rates while Fig. 4.3 (a) reports only four different unloading rates of $\widehat{r} = [10^2, 10^{2.5}, 10^3, 10^6]$. The sphere is unloaded from a fully relaxed substrate with the exponent material of $n = 0.8$ and all the unloading curves in Fig. 4.3 start from the initial contact radius of $\widehat{a}_0 = 3.61$. As anticipated in viscoelastic contact problems, the unloading rate significantly affects the unloading trajectory. Fast unloading boosts viscoelastic dissipation at the crack tip which in turn gives a high pull-off load at detachment. Note that the elastic behavior observed in Fig. 4.3 corresponds to the initial state of the relaxed substrate.

For the same unloading rate $\widehat{r} = 10^{2.5}$, and starting from the same initial contact radius $\widehat{a}_0 = 3.61$ the unloading trajectory will be influenced by the response spectrum of the material. In particular, by using the MPL formulation for simulating a broad-band material (see Fig. 4.2), Fig. 4.3 (b) shows the unloading curves for $n = [0.6, 0.8, 1.6]$, showing that for a given unloading rate the pull-off force generally increases by increasing n. As we will show later, this happens because the more

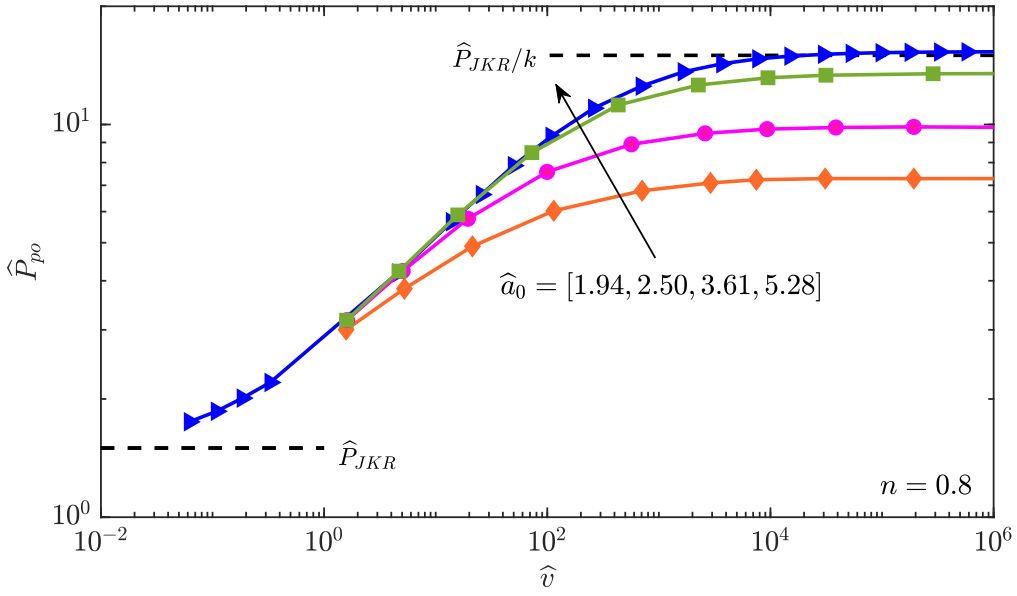

Figure 4.4: Normalized pull-off force as a function of the normalized crack velocity for a material with power law exponent $n = 0.8$ and starting the unloading phase from a fully relaxed substrate with initial contact radii $\widehat{a}_0 = [1.94, 2.50, 3.61, 5.28]$. (From Ref. [19])

narrow-band the material response spectrum is, the faster the theoretical amplification ($\Delta\gamma_{eff}/\Delta\gamma_0 = E_\infty/E_0$) is reached as a function of the retraction rate.

Here, the results of a comprehensive numerical campaign specifically designed for providing, at a given unloading rate, the minimal initial contact radius (or preload) needed to maximize adhesion in a rigid sphere/soft substrate contact are provided. Figure 4.5 (a) shows the pull-off force obtained unloading the substrate at a given unloading rate $\widehat{r} = 10^{0.5}$ as a function of the initial contact radius $\widehat{a}_0$ for $n = [0.4, 0.6, 0.8, 1.6]$ (respectively triangle, star, diamond and square markers). The results show that as $\widehat{a}_0$ increases the pull-off force converges to a certain plateau and that in general, at a given $\widehat{r}$, broad-band materials (low n) will need a smaller initial contact radius to reach convergence of the pull-off force. Hence, in experiments, if the maximum adhesion is sought one must first perform a convergence study on the pre-loading conditions. In Fig. 4.5 (a) we have used a spline to interpolate the simulated points (markers), then we have computed the derivative $d\widehat{P}_{po}/d\widehat{a}_0$ and set the condition $d\widehat{P}_{po}/d\widehat{a}_0 < 0.1$ to determine a *threshold contact radius* indicated by $\widehat{a}_{0t}$, above which we considered the pull-off force is converged. In Fig. 4.5 (a) the black curves change from dotted to solid when the contact radius is greater than $\widehat{a}_{0t}$.

The results in Fig. 4.5 (a) refer to a particular unloading rate taken as a reference $\widehat{r} = 10^{0.5}$. A convergence study was performed over about 5 orders of magnitude in terms of unloading rate, as shown in the inset of Fig. 4.5 (b), where every marker

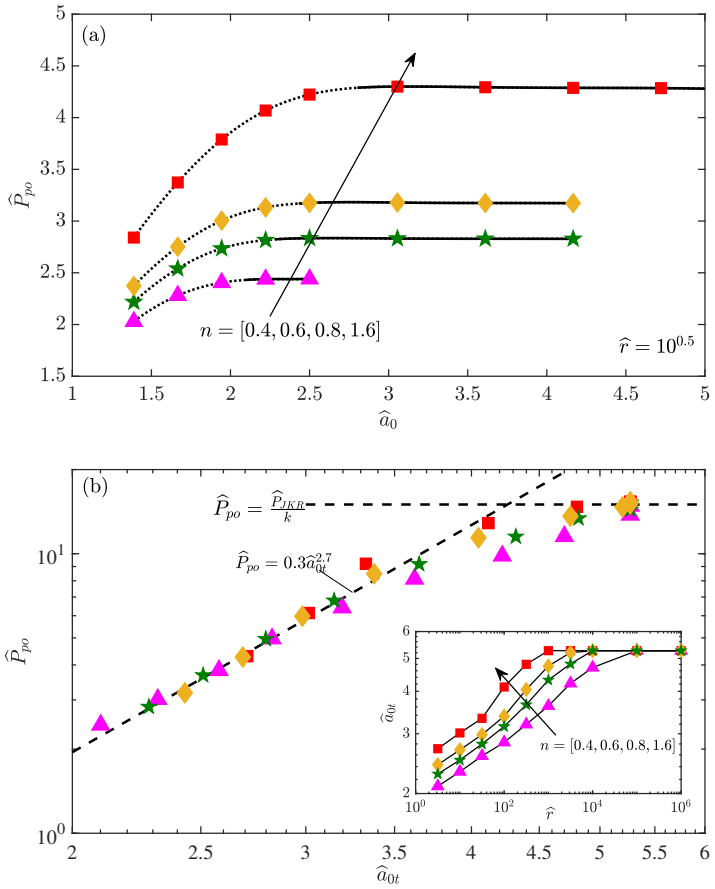

Figure 4.5: Threshold contact radius: (a) Dimensionless pull-off force $\widehat{P}_{po}$ with respect to the normalized initial contact radius $\widehat{a}_0$ with the same unloading rate of $\widehat{r} = 10^{0.5}$ for different material exponents $n = [0.4, 0.6, 0.8, 1.6]$, and $k = 0.1$; (b, inset) Dimensionless threshold contact radius $\widehat{a}_{0t}$ with respect to the normalized unloading rate $\widehat{r}$ for different material exponents $n = [0.4, 0.6, 0.8, 1.6]$ and $k = 0.1$. (b, main figure) The same data reported in the inset are shown as dimensionless pull-off force $\widehat{P}_{po}$ with respect to the normalized threshold contact radius $\widehat{a}_{0t}$. In all the panels triangle, star, diamond and square markers correspond respectively to $n = [0.4, 0.6, 0.8, 1.6]$. (From Ref. [19])

shown corresponds to the threshold contact radius $\widehat{a}_{0t}$ obtained for that material exponent n and at that given normalized unloading rate $\widehat{r} \in [10^0, 10^6]$. The inset of Fig. 4.5 (b) explicitly shows a dependence on the viscoelastic material spectrum broadness (i.e. the exponent n). Nevertheless if the data are represented by the normalized pull-off force at convergence as a function of $\widehat{a}_{0t}$ they collapse for all the exponents n into a single power law curve that we find to be $\widehat{P}_{po} = 0.3\widehat{a}_{0t}^{2.7}$ (black dashed line in Fig. 4.5 (b)), which clearly saturates when the maximum enhancement $\widehat{P}_{po} = \widehat{P}_{JKR}/k = 1.5/k$ is reached. Notice that, the smallest unloading rate considered in our analysis is $\widehat{r} \approx 3$ (see Fig. 4.5 (b), inset) as for quasi-static unloading the elastic solution is retrieved and $\widehat{P}_{po}$ will not depend on $\widehat{a}_0$.

Furthermore, Fig. 4.5 (b) shows that the transition from the power-law behaviour

to the plateau is faster for materials with large material exponent n than for those characterized by low values of n, as a consequence of their narrow spectrum. Hence Fig. 4.5 (b) shows that regardless of the material model, the key parameter that determines the minimum contact radius $\widehat{a}_{0t}$ is the maximum amplification of the pull-off force that has to be reached.

4.5 Persson and Brener crack propagation theory for broad-band viscoelastic materials

In the previous sections, we have shown how the pull-off force depends on the unloading rate and on the initial contact area for various exponent n that characterize the broadness of the viscoelastic material response spectrum. Here, closed-form solutions are obtained for the effective surface energy $\Delta\gamma_{eff}$ based on Persson and Brener [13] crack propagation theory. It is useful to recall that for a Hertzian indenter, in the case of soft materials, the JKR model [22] applies, which provides the pull-off force depends only on the sphere radius and surface energy $P_{JKR} = \frac{3}{2}\pi R\Delta\gamma_0$, hence, in the following, the normalized effective surface energy will be simply defined as $\widehat{\Gamma}_{eff} = \Delta\gamma_{eff}/\Delta\gamma_0 \simeq P_{po}/P_{JKR}$.

We note that our crack propagation formulation is the extension of Persson and Brener [13] idea of equating the input power from the remote load to the power that is dissipated due to the generation of new surfaces and due to viscoelastic dissipation, so one can obtain the effective surface energy $\Delta\gamma_{eff}$ as [13]:

$$\frac{\Delta\gamma_{eff}}{\Delta\gamma_0} = \left[1 - \left(1 - \frac{E_0}{E_\infty}\right)\int_0^{+\infty} \frac{L(\tau)}{(1/E_0 - 1/E_\infty)\,\tau}\left\{\sqrt{1 + b^{-2}(\tau)} - b^{-1}(\tau)\right\} d\tau\right]^{-1}, \tag{4.17}$$

$$b(\tau) = \frac{2\pi v\tau}{l_0}\left(\frac{\Delta\gamma_0}{\Delta\gamma_{eff}}\right) . \tag{4.18}$$

Introducing the dimensionless parameters:

$$\widehat{v} = \frac{v\tau_0}{l_0}; \qquad \widehat{\tau} = \frac{\tau}{\tau_0}, \tag{4.19}$$

and substituting the retardation spectrum defined for the MPL material model in Eq. (4.6) into Eq. (4.17) one gets

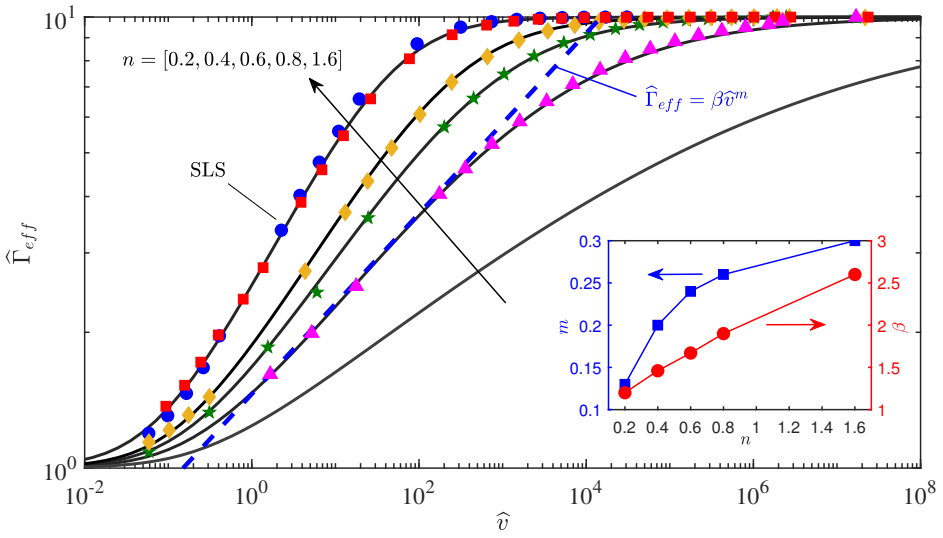

Figure 4.6: Normalized effective surface energy $\widehat{\Gamma}_{eff}$ with respect to the normalized crack velocity $\widehat{v}$ for different power law material exponent $n = [0.4, 0.6, 0.8, 1.6]$, respectively triangle, star, diamond and square markers, and $k = 0.1$. The blue circle markers in the plot correspond to the SLS material. Solid lines stand for the PB model (Eq. 4.21) for $n = [0.2, 0.4, 0.6, 0.8, 1.6]$. The blue dashed line is a guide to the eye, showing the power law behaviour of the function $\widehat{\Gamma}_{eff}(\widehat{v}) = \beta \widehat{v}^m$ in the intermediate velocity range. The inset depicts the fitting parameters $\{\beta, m\}$ for the values of n shown. (From Ref. [19])

$$\widehat{\Gamma}_{eff} = \left[1 - (1-k)\int_0^{+\infty} \frac{\widehat{\tau}^{n-1}\exp\left(-\widehat{\tau}\right)}{\Gamma\left(n\right)} \left[\sqrt{1 + \left(\frac{\widehat{\Gamma}_{eff}}{2\pi\widehat{v}}\frac{1}{\widehat{\tau}}\right)^2} - \left(\frac{\widehat{\Gamma}_{eff}}{2\pi\widehat{v}}\frac{1}{\widehat{\tau}}\right)\right] d\widehat{\tau}\right]^{-1}, \tag{4.20}$$

which can be written as

$$\widehat{\Gamma}_{eff} = \left[1 - (1-k)\, I\left(n, \widehat{v}, \widehat{\Gamma}_{eff}\right)\right]^{-1}, \tag{4.21}$$

where $I(n, \widehat{v}, \widehat{\Gamma}_{eff})$ stands for the integral in Eq. 4.20 whose expression is given in closed form in Appendix IV. Following Persson and Brener [13] original arguments, we determine the lengthscale l_0 equating the linear elastic fracture mechanics stress field to the critical stress σ_c required to break the atomic bonds. Hence:

$$\sigma_c = \frac{K_I}{\sqrt{2\pi l_0}}\,; \qquad K_I^2 = 2E_0^*\Delta\gamma_0\,, \tag{4.22}$$

$$l_0 = \frac{E_0^*\Delta\gamma_0}{\pi\sigma_c^2} = \frac{E_0^*\Delta\gamma_0}{\pi\left(\alpha\sigma_0\right)^2}\,, \tag{4.23}$$

where $E_0^* = \frac{E_0}{1-\nu^2}$ is the rubbery plain strain elastic modulus of the halfspace, K_I is the stress intensity factor in mode I and the "2" in its expression takes into account that one of the contacting bodies is rigid, while α in Eq. (4.23) is a coefficient of order unity to relate the critical stress σ_c in PB theory to the σ_0 we are using in the numerical simulations that are based on the LJ force-separation law. Notice that for soft polymers $l_0/h_0 \approx 1$ hence l_0 should physically be of the same order of the intermolecular distance.

Solving Eq. (4.21) for $n = [0.2, 0.4, 0.6, 0.8, 1.6]$, $k = 0.1$ and for varying crack velocity $\widehat{v}$ one easily find the results shown in Fig. 4.6 (black solid lines). So, for a given effective energy, broad-band materials would require a much higher crack speed than for narrow-band materials. The numerical results from the same set of parameters are shown in Fig. 4.6 as markers ($n = [0.4, 0.6, 0.8, 1.6]$, respectively triangle, star, diamond and square markers), where we find an excellent agreement with the analytical results by using $\alpha = \pi/9 \simeq 0.3491$. It is reminded that the numerical results shown in Fig. 4.6 have been obtained unloading a fully relaxed halfspace and are related to an initial contact radius exceeding the threshold value, i.e $\widehat{a}_0 > \widehat{a}_{0t}$ (see Fig. 4.5). Numerical simulations conducted for $k = E_0/E_\infty = [0.01, 0.05, 0.1]$ confirmed that $\alpha \simeq \pi/9$ independently on the ratio rubbery to glassy modulus k.

It is worth mentioning that the SLS is very often used as a paradigmatic model for a polymer viscoelastic behavior. As a comparison, Fig. 4.6 reports the results obtained for the SLS as blue circles, which confirms the case of the SLS is close to $n = 1.6$ and shows a notably large amplification of interfacial adhesion at relatively low crack speed if it is compared with broad-spectrum viscoelastic material. Our experimental results will show in Section 4.6 that 10:1 PDMS silicone has an exponent $n \simeq 0.22$, which implies the maximum adhesion amplification may be observed only at unloading rates which are orders of magnitude larger than that needed for the SLS, which poses also questions about the practical feasibility of reaching so large retraction rates and possible nonlinear effects that may come into play, which will be discussed in the *Discussion* section. For a more convenient use of Eq. (4.21), the power law scaling of the effective surface energy in the intermediate velocity range is reported here as $\widehat{\Gamma}_{eff} = \beta \widehat{v}^m$ (see blue dashed line in Fig. 4.6), where the parameters β, m can be found in Fig. 4.6 inset.

The applicability of Eq. (4.21) for the prediction of the effective surface energy would remain limited by the fact that in all the viscoelastic crack propagation theories, including Eq. (4.21), the enhancement of the surface energy is a function of the crack velocity at pull-off which is generally not an input parameter in experiments and would be anyway difficult to control. Nevertheless, Fig. 4.7 shows in the inset

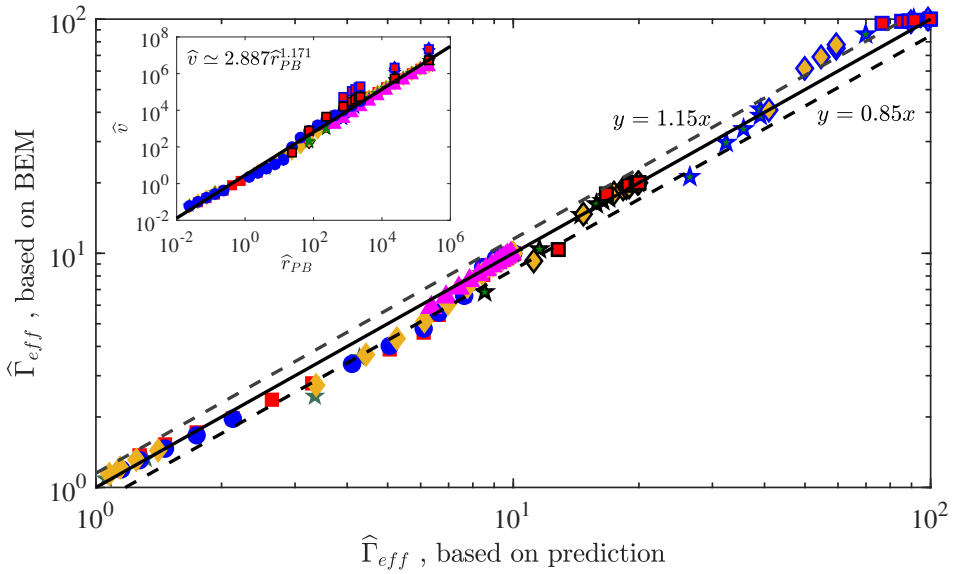

Figure 4.7: Normalized effective surface energy $\widehat{\Gamma}_{eff} = P_{po}/P_{JKR}$ based on the numerical BEM simulations versus the normalized effective surface energy predicted by using the Eq.s (4.21,4.24). (inset) Normalized crack velocity $\widehat{v}$ versus the normalized unloading rate ($\widehat{r}_{PB}$). In both the main figure and the inset the same numerical results are shown, in particular for different power law material exponent $n = [0.4, 0.6, 0.8, 1.6]$, respectively triangle, star, diamond and square markers, and $k = [0.01, 0.05, 0.1]$ respectively markers with a blue contour line, with a black contour line and without contour line. Blue circles stand for the SLS with $k = 0.1$. (From Ref. [19])

that the crack velocity at pull-off $\widehat{v}$ scales approximately as:

$$\widehat{v} = 2.887\widehat{r}_{PB}^{1.171} \ , \tag{4.24}$$

over about 10 orders of magnitude in terms of unloading rate $\widehat{r}_{PB}$, where $\widehat{r}_{PB} = r\tau_0/l_0$. Figure 4.7 shows the numerical results obtained for the material exponents $n = [0.4, 0.6, 0.8, 1.6]$, respectively triangles, stars, diamonds, squares (circles stand for the SLS material) and for $k = [0.01, 0.05, 0.1]$ respectively markers with a blue contour line, with a black contour line and without contour line. Filled blue circles stand for the SLS with $k = 0.1$. Hence, after using Eq. (4.24) to estimate the crack speed at pull-off as a function of the retraction rate, we have used Eq. (4.21) to predict the effective surface energy and compared with the numerical BEM results, using the same symbols as in the inset, which are shown in the main Fig. 4.7. The solid black line represents the condition of the perfect match between prediction and actual numerical results, while as a guide to the eye, we have drawn also two dashed lines representing $\pm 15\%$ error. Although the scaling may be improved by using more refined models, the use of Eq.s (4.21,4.24) makes the estimate of the pull-off force straightforward based only on the material parameters and on the unloading rate. It

is recalled that all the numerical results have been obtained for the Tabor parameter $\mu = 3.24$, hence we expect Eq. (4.24) to be valid in the limit of short-range adhesion also referred to as the "JKR limit" [22].

4.6 Experimental adhesion tests

In the previous sections we have developed a general MPL material model capable of describing the viscoelastic behaviour of both narrow and broad band materials, then we have compared BEM numerical results with PB theory finding an excellent agreement. Finally, in this section, the numerical predictions will be validated against experimental results.

A series of adhesion tests were performed using a smooth spherical lens loaded and unloaded from a soft viscoelastic substrate at various unloading velocities. The spherical lens was made of borosilicate crown glass (SLB-05-10P, Sigma Koki) with a nominal radius of R = 5.19 mm and the substrates were made of polydimethylsiloxane (PDMS, Sylgard 184, DowCorning Corporation) with resin to curing agent weight ratio of 10:1. PDMS is a silicone elastomer well known to exhibit viscoelastic properties, as confirmed in several previous studies [21, 153, 156, 162]. For the substrate material characterization, a classical dog-bone shaped specimen was fabricated and used for dynamic mechanical analysis (DMA). All the samples were cured at 70 °C for two hours on a heating table and then followed by natural cooling.

4.6.1 Material characterization

The DMA test was performed using a DMA850 (TA Instruments) to characterize the viscoelastic properties of the PDMS. The dog-bone-shaped specimen had cross-sectional dimensions of 3.86 mm in width and 0.75 mm in thickness. Temperature sweeps were conducted at a fixed frequency of $f = 1$ Hz and a strain amplitude of $\epsilon = 0.1\%$. The temperature runs from -130 °C to 20 °C with 10 °C step size. To move from temperature to frequency domain we used the WLF time-temperature superposition [84], hence the shift factor is defined as

$$\log_{10} a_T = \log_{10} \frac{f_{T_g}}{f_T} = \frac{-17.44\,(T - T_g)}{51.6 + T - T_g}\,, \tag{4.25}$$

where f_T is the frequency at the temperature T and T_g is the glass transition temperature. For the PDMS substrate, we assumed $T_g = -115$°C, which agrees well with the results reported in Ref. [21] for the same material. Furthermore, we note

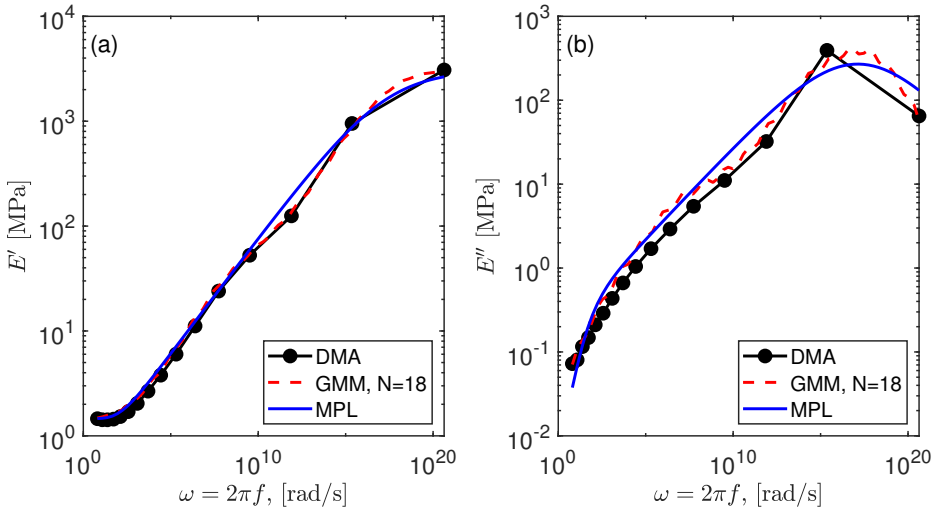

Figure 4.8: (a) Real part of the complex elastic modulus E' in the frequency domain at $T_{amb} = 20\ ^{\circ}C$. (b) Imaginary part E'' of the complex elastic modulus in the frequency domain at $T_{amb} = 20\ ^{\circ}C$. In both panels: the black curve with circle markers stands for the experimental data, the blue curve for the fitted MPL material model and the red curve for the fitted GMM model with 18 arms (see Fig. A.2). (From Ref. [19])

that using $T_g = -115°$C our measurements of the complex modulus $\overline{E}$ also satisfy the Kramers-Kronig (KK) relation [163]

$$E''(\omega) = -\frac{2\omega}{\pi}\int_0^{+\infty}\frac{E'(u)}{\omega^2 - u^2}du\,, \tag{4.26}$$

where $\omega = 2\pi f$ is the angular frequency and the integral should be intended as its Principal Value [163].

The experimental data for the complex modulus were shifted to $T_{amb} = 20\ ^{\circ}$C by using Eq. (4.25) and fitted using Eq. (4.7), which is written in terms of the complex compliance $C(\omega)$ as that is the function needed in the numerical BEM implementation (see Eq. (4.15)). Figure 4.8, panels (a)-(b), shows the complex modulus $\overline{E}(\omega) = 1/\overline{C}(\omega) = E'(\omega) + \boldsymbol{i}E''(\omega)$ as obtained experimentally (black solid curve with circle markers) and as fitted by the MPL material model (blue solid curve). For PDMS we found

$$\begin{gathered} E_0 = 1.458 \text{ MPa} \\ E_\infty = 3.089 * 10^3 \text{ MPa} \\ n = 0.2207 \\ \tau_0 = 0.01876 \text{ s} \end{gathered} \tag{4.27}$$

For comparison purposes, the result that would have been obtained by fitting the experimental data using a Generalized Maxwell Model (GMM, also known as

the "Wiechert model") with 18 arms, hence 37 constants, is also shown in Fig. 4.8 as a dashed red curve. One realizes that both the GMM and the MPL models give a fair representation of the material behavior, although the MPL model is simpler to use, and the four parameters used in the fitting procedure $\{E_0, E_\infty, n, \tau_0\}$ have a straightforward physical interpretation.

4.6.2 Experimental setup and comparison

A custom-designed adhesion test instrument, based on the tribometer platform (NTR2, CSM Instruments), was constructed to measure the pull-off force. As illustrated in Fig. 4.9 (a), the lens was rigidly fixed to the force sensor. The PDMS substrate was positioned above a transparent rigid box, with the contact interface observable through a camera via a prism mounted inside the box. The pull-off tests comprised three sequential steps: loading, dwelling, and unloading. Initially, the lens was gradually loaded against the PDMS substrate with a preload force denoted as P, followed by a dwell period of 60 seconds to ensure complete relaxation of adhesive contact. Subsequently, the lens was pulled out at a fixed unloading rate, r. Throughout the entire process, the normal force was recorded and the pull-off force represents the absolute minimum normal force. Firstly, we measured the variation of the normal force with the contact radius, a, at a very low unloading rate $r = 0.98\mu$m/s to determine the interfacial parameters, as shown in Fig. 4.9 (b). By fitting the relationship between the normal force and contact radius using Carpick's method [164], we estimated the intrinsic work of adhesion $\Delta\gamma_0 = 0.152$ J/m^2 and the Tabor parameter $\mu = 2.05$. Next, we conducted tests by varying the unloading rate r. The lens is brought into contact with the PDMS substrate and loaded to the preset preload $P_0 = 1.5$ mN. After a 60-second dwell period, the lens is moved upward until the contact is broken and the lens is pulled off from the substrate. We used our numerical BEM code, using the MPL material model for the viscoelastic substrate, to predict the pull-off force during the unloading process. The comparison with experiments leads to the result shown in Fig. 4.10, where the pull-off force, P_{po} [mN], is plotted as a function of the unloading rate, r [μm/s] (the red squares stand for the experimental data, the black solid line for the numerical results). According to Fig. 4.10, the experimental results confirm an increase in the pull-off force with increasing unloading rates. While there is good agreement between numerical and experimental results in the range of retraction rates $r = [1, 100]$ μm/s, the experimental data exhibit marked higher values than the numerical predictions for high values of the unloading rate $r > 100$ μm/s, which agrees well with other published experimental results [20, 21]. For having a good fit of the low speed experimental results, we set

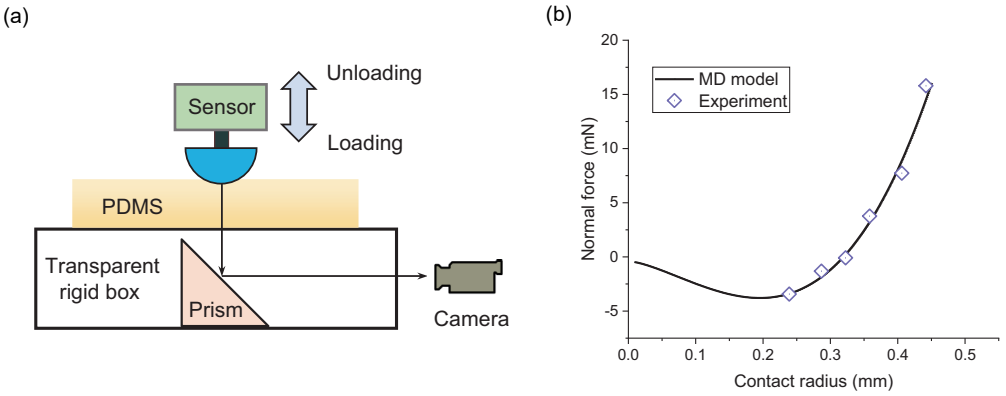

(a) **(b)**

Figure 4.9: (a) Schematic of the experimental setup for adhesion tests; (b) Variations of normal force with contact radius a at a very low unloading rate to determine the interfacial parameters. (From Ref. [19])

$h_0 = 30.8$ nm, which is discussed in detail in the Discussion section.

4.7 Discussion

4.7.1 On the possibility of reaching the maximum adhesion enhancement

According to viscoelastic crack propagation theories [13, 73, 74] the maximum enhancement of the pull-off force is $\widehat{P}_{po} = \widehat{P}_{JKR}/k$, hence based on the results reported in Section 4.4, one can estimate that for a PDMS material with $k \simeq 4.73 * 10^{-4}$ the maximum amplification of the pull-off force will be reached for $\widehat{a}_{0t} \simeq 30.9$. Using the interfacial and material properties we have found for PDMS ($\Delta\gamma_0 = 152.3$ mJ/m^2, $\nu = 0.5$, $E_0^* \simeq 1.94$ MPa) and for $R = 5.19$ mm gives an initial contact radius of $a_{0t} = 5.8$ mm, which is larger than the sphere radius and even considering a parabolic (Hertzian) profile certainly outside the limit of validity of the hypothesis of small deformations, which raises doubts about the practical feasibility of reaching the maximum amplification factor predicted by crack propagation theories.

Another consideration to be made is related to the unloading rate that would be needed to reach the maximum adhesion amplification. By using the results reported in Section 4.6, one estimates that to reach the maximum amplification for a PDMS substrate one would need to unload the substrate at $\widehat{v} \approx 10^9$ (see Fig. 4.6), which using $l_0 = 30.0$ nm and $\tau_0 = 0.01876$ s together with Eq. (4.24) gives the dimensional unloading rate of about $r \approx 31.4$ m/s, which is about 4 orders of magnitude larger than the maximum unloading velocity usually used in adhesion experiments [20, 21], provided also the limitations introduced by the inertia of the

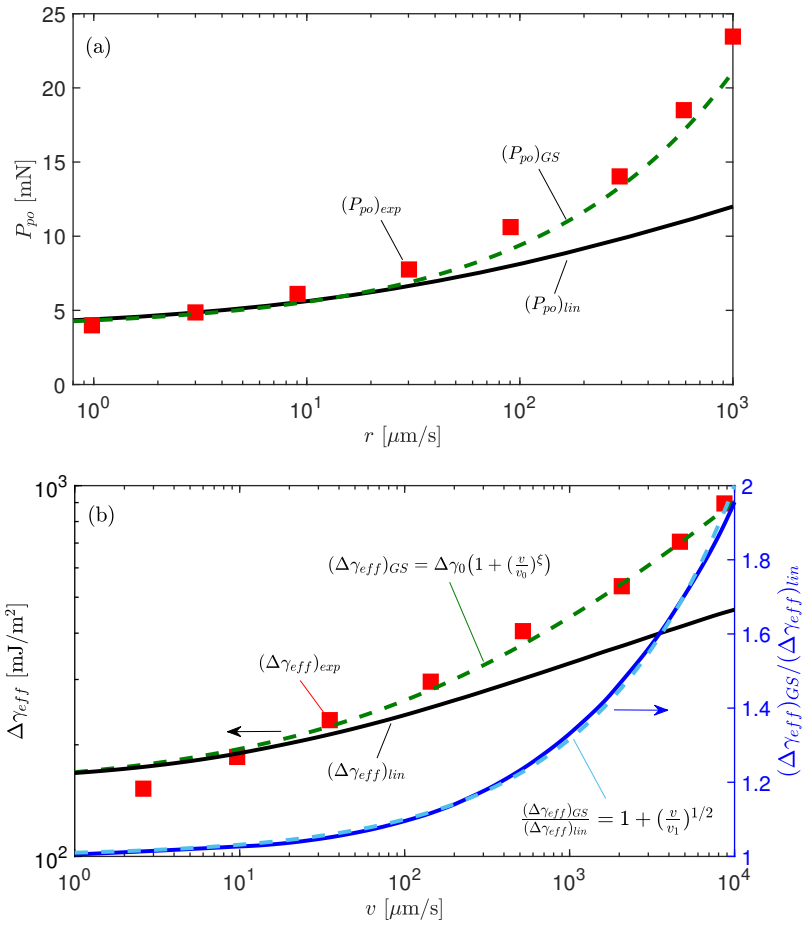

Figure 4.10: (a) Pull-off force as a function of the unloading rate: comparison between numerical (from the BEM code, solid black line, labelled $(P_{po})_{lin}$) and experimental results (red square markers) for preload $P_0 = 1.5$ mN, $R = 5.19 * 10^{-3}$ m, $\Delta\gamma_0 = 152.3$ mJ/m^2, $h_0 = 30.8$ nm. The green dashed line was obtained using the effective surface energy fitted on the experimental results labelled as $(\Delta\gamma_{eff})_{GS}$ and shown in panel (b). (b, left y-axis) Effective surface energy from: the experimental results (red squares, labelled $(\Delta\gamma_{eff})_{exp}$), the fit of the experimental data using a Gent and Schulz power law model (Eq. (4.28), where $v_0 = 213.5$ μm/s and $\xi = 0.4154$, dashed green line, labelled $(\Delta\gamma_{eff})_{GS}$), the prediction obtained for the PDMS substrate using the *linear* numerical BEM model (solid black line, labelled $(\Delta\gamma_{eff})_{lin}$). In this respect we used our approximate Eq. (4.24) to determine the crack velocity at pull-off starting from the experimental retraction rate. (b, right y-axis) The ratio between $(\Delta\gamma_{eff})_{GS}/(\Delta\gamma_{eff})_{lin}$ for which a power law fit is provided $\frac{(\Delta\gamma_{eff})_{GS}}{(\Delta\gamma_{eff})_{lin}} = 1 + (\frac{v}{v_1})^{1/2}$ where $v_1 = 10^4 \mu$m/s (dashed pale blue curve). (From Ref. [19])

motorized linear stages. Hence, insufficient preload and unloading rates used in experiments may partially explain why, in Literature, measurements of very large enhancement factors, even close to $1/k$, are missing (see for example Tiwari et al. [20], VanDonselaar et al. [21]).

Our numerical and experimental results seem to be in agreement with the experimental adhesion tests reported in Refs. [20, 21] for a similar PDMS material, where they also found that PB theory agreed well with experimental observations only up to about $r \approx 100\ \mu m/s$. This may suggest that both numerical and theoretical models are lacking essential phenomena to describe the detachment process at high retraction rates. At present, a few hypotheses have been formulated, ranging from the possibility of nonlinear dissipative phenomena, happening within the process zone, like (i) cavitation and stringing, (ii) extraction of non-cross linked polymeric chains from the substrate, (iii) temperature dependence of the material behaviour at the crack tip, (iv) the nonlinear behaviour of the material at the large strains ($\approx 10\%$) experienced close to the crack tip [20, 21], of course not included into the (linear) theoretical and numerical models, which is discussed in the next subsection.

4.7.2 Energy dissipation within the process zone

To obtain a satisfactory fit of the experimental data at low unloading rates we set $h_0 = 30.8$ nm. Notice that from quasi-static experiments, using the definition of the Tabor parameter we would have obtained a much larger equilibrium distance $h_0 = 1.55\ \mu$m, which is close to what can be obtained for the same PDMS material using the parameters in Oliver et al. [160]. This calls for further investigations in the future.

For the PDMS material we have characterized, using $h_0 = 30.8$ nm, one obtains that the size of the process zone that fits the experimental data in Fig. 4.10a is $l_0 \simeq 30.0$ nm. Indeed, determining the length of the process zone in viscoelastic crack propagation is still an open question. In the de Gennes [165] and Saulnier et al. [166] theories, the size of the "nonlinear" zone is assumed to be a constant, and the fracture energy has its maximum amplification at intermediate speeds. In PB theory this size is not constant and is directly proportional to the applied energy release rate G, which results in a model practically coincident with the cohesive zone model of Knauss and Schapery (see Knauss [167]). However, in fitting experimental data of fracture Hui et al. [168] consider two examples, a styrene-butadiene co-polymer from Gent and Lai [169], where they don't have independent estimate of the cohesive strength, but simply fit the fracture energy vs speed data, obtaining a process zone size at low speed of a nonphysical size of 0.1 nm, consistent with Gent and Lai [169].

In the second example, they consider a polyurethane elastomer called Solithane 113 of Knauss [167], and obtain by the same process a size of 1 nm. Hence, Hui et al. [168] conclude that this size cannot realistically represent a dissipation zone for which a lower bound should be the length of the monomer unit ≈ 46 nm [170]. [2] Notice that nonlinear crack propagation theories have been developed by Schapery using cohesive models [172], and have provided a fracture process zone at low speeds of approximately 10 nm, much more realistic than the 0.1 nm found by Knauss [167] and Schapery [74] for Solithane rubber. In fitting crack propagation data in rubbers, Schapery [173] (Tab. 1) found a jump in propagation speed at a certain applied load which seems to suggest a sharp change of cohesive zone fracture energy as a function of speed. He found a low speed fracture energy which is higher than the fast propagation speed fracture energy of a factor of about 6. In our adhesion experiments, our theory is linear and hence we cannot exclude that a nonlinear theory would explain this apparent continuous change of cohesive zone fracture energy with the speed of the linear theory, which is an increase with speed rather than a decrease and hence gives no instability.

Barthel [174] reports post mortem experimental measurements of the process zone length from damage that occurred at the crack tip and shows this should be of a physically reasonable size of the order of microns. Also, it clearly increases with size as PB and Schapery suggest, but contrary to the original DeGennes and Sauliner theories. Furthermore, linear theories seem to work better for very viscoelastic solids, namely when the glass transition temperature is above ambient temperature, perhaps because for very viscoelastic materials the dissipation in the bulk becomes dominant [174].

We have estimated the experimental effective surface energy $\Delta\gamma_{eff}(v)$ (Fig. 4.10b, left y-axis) as obtained from experiments (red squares), fitted by a Gent-Schultz [83] power law equation (green dashed curve)

$$\Delta\gamma_{eff} = \Delta\gamma_0 \left(1 + \left(\frac{v}{v_0}\right)^{\xi}\right) , \tag{4.28}$$

and estimated from our linear BEM numerical scheme (black solid line), respectively $\{(\Delta\gamma_{eff})_{exp}$, $(\Delta\gamma_{eff})_{GS}, (\Delta\gamma_{eff})_{lin}\}$ in Fig. 4.10b. To estimate the crack velocity at pull-off from the retraction rates used in the experiments we used the approximate relationship in Eq. (4.24), and this shows that a linear theory would fit the data much better

[2] Recent literature contributions have started to question the validity of classical linear elastic fracture mechanics for unfilled plastics and elastomers suggesting that fracture initiates at a critical tensile strength, see Wang et al. [171].

(see dashed green line in Fig. 4.10) if we assume a rate-dependent surface energy. Notice that PDMS (10:1) elastic behavior (quasi-static loading, room temperature) has been well characterized and it shows a very neat linear behavior up to $\approx 50\%$ strain [175], hence, in principle, one would expect PB theory should work, unless other causes of dissipation are at play.

Indeed, even considering that $l_0 \simeq 30.0$ nm is a more realistic estimate of the length of the fracture process zone, still we have shown that above $v = 100$ μm/s the linear theory largely underestimates the effective surface energy as shown in Fig. 4.10b. Hence, other rate-dependent causes of dissipation seem to be at play which consistently contribute to determine the overall energy to be spent for the crack to propagate.

As we have demonstrated numerically, linear theories such as PB theory, successfully estimate the dissipation happening within the bulk material, but they fail to account for the rate-dependent nonlinear dissipative processes taking place within the process zone. Clearly, the assumption of constant intrinsic fracture energy and cohesive stress in the cohesive zone where large strain, high strain rate and nonlinear deformations (including damage) happen, is questionable as noticed by a very recent contribution by Barthel [174]. Introducing the dissipative contribution coming from the nonlinear phenomena happening within the process zone would ultimately require additional constants to be determined from actual measurements, unless one aims at describing all the nonlinear processes happening within the process zone. Unfortunately, the way the effective surface energy $\Delta\gamma_{eff}$ increases with speed would require a separate investigation as this is a completely different contribution than the one coming from viscoelastic bulk dissipation and, at present, the scientific community has not agreed on a good model for it [176–179].

Given the considerable effort in the theory in characterizing the viscoelastic linear properties, these recent models are trying mostly to understand how much of the fracture energy amplification comes from the bulk dissipation and how much from the cohesive zone process rate-dependence. In this respect, the estimate we gave in Fig. 4.10b suggests that in our experiments at $v = 10^4 \mu$m/s the nonlinear rate-dependent dissipative contribution originated within the process zone $(\Delta\gamma_{eff})_{GS} - (\Delta\gamma_{eff})_{lin}$ equals the one coming from the dissipation in the bulk $(\Delta\gamma_{eff})_{lin}$ (blue curve).

4.8 Summary of findings

We have studied the adhesive contact between a rigid Hertzian indenter and a substrate constituted by a broad spectrum viscoelastic halfspace. For the material

we have adopted a Modified Power-Law (MPL) material model, originally proposed by Williams [72], that we have extended to provide closed-form results for the creep compliance function and for the relaxation function in the time domain, and also for the complex modulus and the complex compliance in the frequency domain. Notably, the MPL model is a function of only 4 parameters, the two moduli, a characteristic exponent n and a characteristic time τ_0. In particular, by changing the exponent n, we have shown that it is possible to have a realistic description of a broad-band viscoelastic material, which we have demonstrated by fitting the complex modulus measured for a PDMS sample.

By using a numerical model based on the Boundary Element Method (BEM), extensive numerical studies have been performed in a wide range of the unloading rate, spanning about 8 orders of magnitude. We have shown that due to viscoelasticity, the effective surface energy can be strongly enhanced with respect to the thermodynamic surface energy, nevertheless to avoid finite size effects a certain minimum contact radius has to be reached, which we named a "threshold contact radius" a_{0t}. Our numerical simulations have shown that a_{0t} is independent of the material exponent, but it depends on the pull-off enhancement that has to be reached at high unloading velocity.

Provided that finite size effects are avoided ($a_0 > a_{0t}$), the theory of Persson and Brener [13] can be used to determine the pull-off force of the spherical indenter as a function of the crack speed at pull-off with high accuracy, but only within the assumptions of the linear theory and rate-independent fracture process zone parameters. Relating the numerical results based on a Lennard-Jones force-separation law to the theory of Persson and Brener [13] required to define a parameter $\alpha = 0.3491$ of order unity that relates the critical stress σ_c in PB theory to the maximum stress used in the LJ law σ_0, which was found independent on the ratio $k = E_0/E_\infty$. Adhesion experiments are usually run in displacement control, and the crack speed at pull-off is certainly not a control parameter, nevertheless, we have shown that the velocity of the crack at pull-off $\widehat{v}$ scales as $\widehat{v} \simeq 2.887\widehat{r}_{PB}^{1.171}$ over more than 8 orders of magnitude, which provides an extremely simple relation to roughly estimate the pull-off force starting only from the material model parameters and the unloading rate with about $\pm 15\%$ confidence.

Finally, by using the MPL for the viscoelastic material and the developed BEM code, we have attempted a comparison between the numerical and the experimental results, which turned out to be satisfactorily accurate up to unloading rates $r = 100$ μm/s, while for faster unloading the numerical results predict lower enhancement with respect to what is measured by our experiments. This observation turns out to

be in good agreement with previous Literature results Refs. [20, 21], where similar experiments were conducted.

A nonlinear description of the material behaviour must be necessarily a better description than linear, so perhaps the J integral approach of Schapery [180] could improve our results. However, as in classical nonlinear fracture mechanics, we ultimately need to measure experimentally the critical value of the fracture energy, which cannot be found reliably from other material properties, in viscoelastic adhesion even if some progress is made by the linear theories, the estimate of the bulk dissipation contribution to fracture energy enhancement is not sufficient, and, ultimately, the fracture process zone rate-dependency must be measured experimentally. Hence, at present, the measurement of the $\Delta\gamma_{eff}(v)$ curve remains the only engineering approach, resulting in the phenomenological Gent and Schultz [83] law. Notice that if we use the measured Gent-Schultz law with a power $\xi = 0.41$ and assume the far field material is elastic with relaxed modulus, we can solve the adhesive contact problem using the Muller solution as corrected in Ciavarella [181]. This results in a pull-off force that doesn't scale with the same power law of the Gent-Schulz law, but with power 0.27 in this case, so also the Muller solution is misleading.

Chapter 5

Data-driven surrogate models for viscoelastic adhesion

Publication note. The work presented in this chapter led to the peer-reviewed paper published in *International Journal of Solids and Structures* [81].

This chapter translates the Hertzian mechanics framework into fast surrogate models for viscoelastic adhesion. The first part compares standard machine-learning regressors with physics-augmented variants for predicting pull-off force, effective surface energy, and work to pull-off across the simulated parameter space, showing how analytical descriptors improve generalization and interpretability without sacrificing predictive speed. The second part extends the surrogate framework from scalar outputs to reduced-order prediction of unloading trajectories through feed-forward neural networks, moving from endpoint prediction toward time-resolved surrogate modelling.

5.1 Introduction

Real-time prediction of viscoelastic adhesion is essential for applications requiring reliable handling, adaptive contact, and rapid design optimization, yet conventional numerical simulations remain too computationally demanding for such use because they depend strongly on material behavior, loading history, and iterative time-marching schemes. In this context, machine learning offers a computationally efficient alternative, since once trained it can provide fast predictions even for complex, high-dimensional problems. Although ML has already shown strong potential across materials science, fracture, contact mechanics, tribology, and adhesion-related design, most existing studies focus on simplified geometries or purely data-driven surrogates that sacrifice physical interpretability.

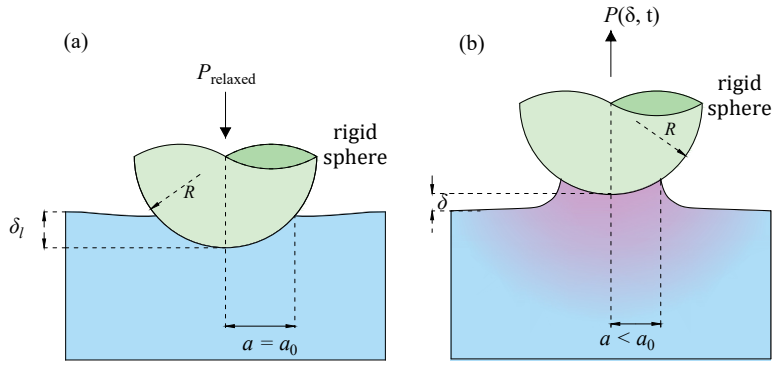

Figure 5.1: Schematic representation of the contact interaction between a rigid sphere and a viscoelastic surface: (a) viscoelastic surface in the fully relaxed state under contact, (b) unloading phase at a constant unloading rate. (From Ref. [81])

In this chapter, we address the problem of a rigid sphere with radius R being unloaded from a relaxed broad-band viscoelastic adhesive half-space (see Fig. 5.1). We aim to present ML-based models, both classical (ML) and physics-augmented (PA-ML), that predict the pull-off force and the work to pull-off as a function of five parameters: the Tabor parameter μ, the exponent n characterizing the broadness of the material spectrum, the modulus ratio k, the normalized indentation depth reached during the quasi-static loading phase, and the normalized unloading rate. A detailed comparative analysis will be conducted to evaluate the accuracy of different ML algorithms (Linear Regression, Regression Tree, Random Forest, and XGBoost will be considered) and to compare the performance of a pure data-driven approach (ML) against that of a physics-augmented ML model (PA-ML).

The remainder of the chapter is structured as follows: Section 5.2 provides a detailed description of our physical model, including the normalization approach that enables comparison with analytical models. This section also includes a discussion

on the scaling of input parameters and their impact on the computational cost of the numerical model; Section 5.3 presents the range of exploration as well as the background on ML and describes the ML models and PA-ML models employed in this study; Section 5.4 provides the results of ML and PA-Ml models; Section 5.5 extends the framework to trajectory-level prediction of adhesive forces through feed-forward neural networks. Finally, Section 5.6 summarizes the main findings and presents concluding remarks.

5.2 Physical background and simulation framework

The simulation framework employed here was established in full in Chapter 4 (Sections 4.2–4.3) and is not repeated here. Briefly, a rigid sphere of radius R is unloaded from a fully relaxed viscoelastic adhesive halfspace at constant rate r_u (see Fig. 5.1). The interface is governed by the Lennard-Jones force-separation law (Eq. 4.11); the gap at radial position r and time t is given by Eq. (4.12); the time-dependent half-space deflection follows from the elastic–viscoelastic correspondence principle (Eq. 4.15); and the MPL creep compliance is Eq. (4.9) [19, 81]. The full BEM implementation and normalisation are in Appendix V.

In normalised form, the five inputs to the model are: the Tabor parameter μ, the viscoelastic parameters $\{k = E_0/E_\infty, n\}$, the normalised initial indentation $\widehat{\delta_l} = \delta_l/h_0$, and the normalised unloading rate $\widehat{r_u} = r_u/\tau_0 h_0$. The output of the numerical model includes the interfacial gap h, the pressure distribution, the normal force P, the indentation δ as a function of time. Figure 5.2 shows the dimensionless normal force $\widehat{P} = \frac{P}{1.5\pi\Delta\gamma_0 R}$ as a function of the dimensionless indentation $\widehat{\delta}$ for different combinations of the input parameters $\{\widehat{\delta_l}, n, \widehat{r_u}\}$ for $\mu = 3.24$ and $k = 0.1$. These curves illustrate the relationship between the applied load and the indentation depth under various input conditions. One can observe the influence of the normalized input parameters, such as the unloading rate (Figure 5.2(a)), the power law exponent (Figure 5.2(b)), and the indentation-depth (Figure 5.2(c) and (d)), on the force-displacement behavior and its effect on key parameters such as the maximum adherence force reached during unloading $\widehat{P_{po}} = |\min(\widehat{P})|$ (known as pull-off force) and work to pull-off which is defined as $w_{\text{po}} = \int_{\delta_{\text{on}}}^{\delta_{\text{po}}} P(\delta, t)\, d\delta = \widehat{w}_{po}(1.5\pi\Delta\gamma_0 R h_0)$, where δ_{on} denotes the displacement at which the normal force first becomes zero during unloading (i.e., the onset of tensile loading), and δ_{po} is the displacement at pull-off [17]. This quantity represents the area under the unloading curve in the tensile regime and captures the energy dissipated during detachment, including both adhesive and viscoelastic contributions as it is highlighted in Figure 5.2(a).

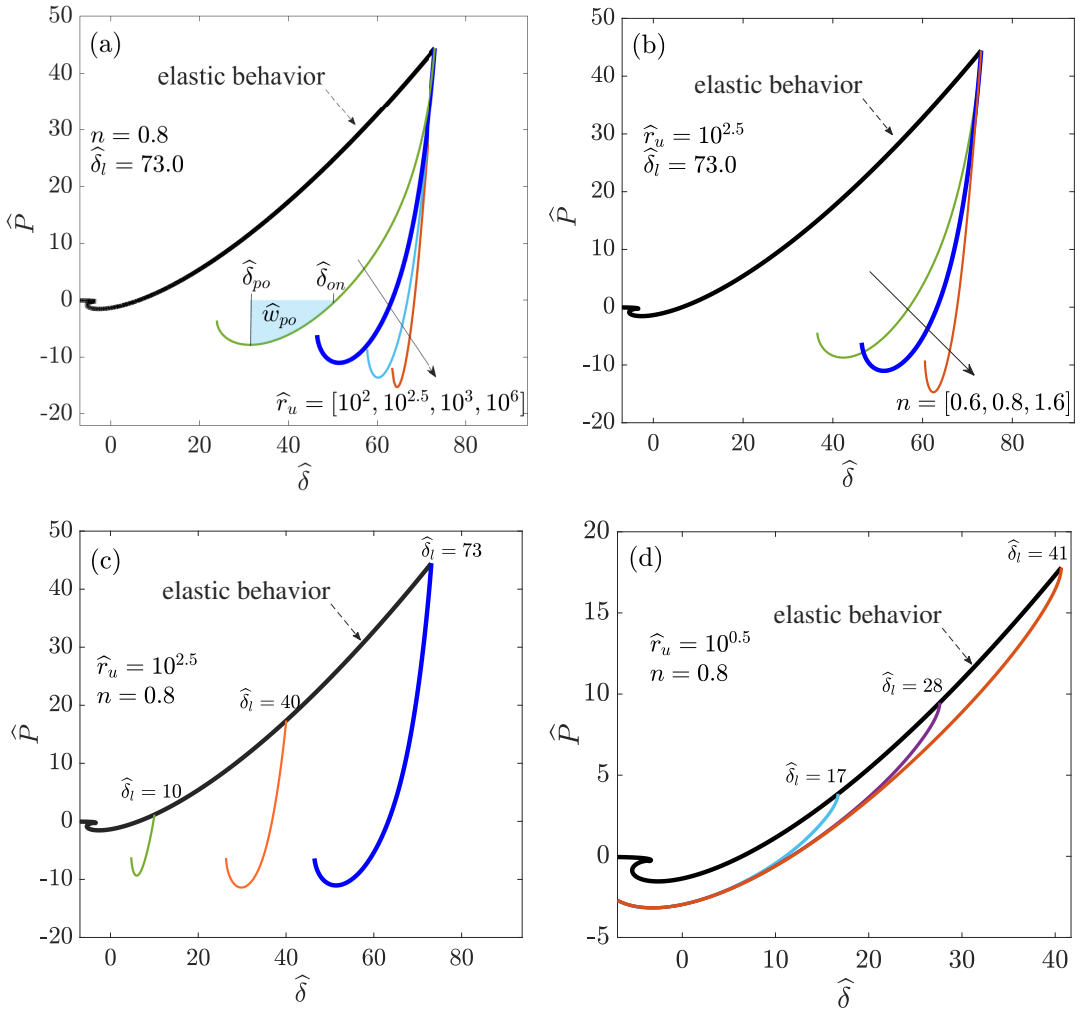

Figure 5.2: Load vs. indentation curves demonstrating adhesive interactions (with negative load values indicating tensile forces) between a Hertzian indenter and a viscoelastic substrate. All panels correspond to a fixed Tabor parameter of $\mu = 3.24$ and dimensionless modulus ratio of $k = 0.1$. (a) Effect of unloading rate on the adhesive response, for a fixed initial indentation depth of $\widehat{\delta}_l = 73.0$ and material power-law exponent $n = 0.8$; (b) Influence of the material's power-law exponent $n = [0.6, 0.8, 1.6]$, under fixed initial indentation depth of $\widehat{\delta}_l = 73.0$ and unloading rate of $\widehat{r}_u = 10^{2.5}$; (c) Effect of different initial indentation depths, $\widehat{\delta}_l = [10.0, 40.0, 73.0]$, with constant material exponent of $n = 0.8$ and unloading rate of $\widehat{r}_u = 10^{2.5}$; (d) Observation of saturation behavior for $\widehat{r}_u = 10^{0.5}$, $n = 0.8$, and $\widehat{\delta}_l = [16.7, 27.6, 40.7]$, where the pull-off force approaches a limiting value beyond a critical indentation depth, indicating the presence of a threshold in the adhesive response. (From Ref. [81])

While the BEM model provides detailed insight into the adhesive response under a wide range of conditions, its nonlinear and history-dependent nature results in significant computational demands. Specifically, the total computational cost scales with the product of spatial discretization size, number of time steps, and convergence iterations per step—making real-time prediction across large parameter spaces challenging. To complement these simulations, we employ the extended Persson–Brener (XPB) model derived in Section 4.5 of Chapter 4 [19]. In normalised form, the effective surface energy $\widehat{\Gamma}_{\text{eff}} = \Delta\gamma_{\text{eff}}/\Delta\gamma_0 \approx \widehat{P}_{\text{po}}$ (where $\widehat{P}_{\text{po}}$ is the normalised pull-off force) is expressed as a function of crack velocity v and viscoelastic material parameters through the integral:

$$\widehat{\Gamma}_{\text{eff}} = \left[1 - (1-k)\int_0^{+\infty} \frac{\widehat{\tau}^{n-1}\exp\left(-\widehat{\tau}\right)}{\Gamma(n)} \left[\sqrt{1+\left(\frac{\widehat{\Gamma}_{\text{eff}}}{2\pi\widehat{v}}\frac{1}{\widehat{\tau}}\right)^2} - \left(\frac{\widehat{\Gamma}_{\text{eff}}}{2\pi\widehat{v}}\frac{1}{\widehat{\tau}}\right)\right] d\widehat{\tau}\right]^{-1}, \tag{5.1}$$

with the normalized parameters defined as $\widehat{v} = \frac{v\tau_0}{l_0}$, $\widehat{\tau} = \frac{\tau}{\tau_0}$, where $l_0 = \frac{E_0^*\Delta\gamma_0}{\pi\sigma_c^2}$ is a stress-based characteristic length and the critical stress $\sigma_c = \alpha\sigma_0$ is related to the peak tensile stress σ_0 from the Lennard-Jones interaction through a proportionality factor $\alpha \approx \pi/9$, as shown in [19]. Furthermore, it was shown in Ref [19] that the crack speed $\widehat{v}$ is approximately related to $\widehat{r}_u$ as $\widehat{v} = 2.887\widehat{r}_u^{1.171}$. Hence, in the following, we will use this approximation to determine the effective surface energy predicted by XPB as a function of k, n, and $\widehat{r}_u$. We note that the implicit equation (5.1) is solved very efficiently using fixed-point iteration [19].

5.3 Machine learning for generalization beyond analytical models

5.3.1 Range of exploration beyond analytical models

Figure 5.3 schematically visualizes the parameter space explored in this work as three-dimensional cubes. The left cuboid spans the power-law exponent n, the Tabor parameter μ, and the normalized initial indentation depth $\widehat{\delta}_l$. In this study, the exponent n ranges from wide band behavior of $n = 0.2$ encompassing the range commonly observed in silicone-based polymers at room temperature (e.g., PDMS, as reported in [2, 159]) to values around 2.0 related to a very narrow banded behavior. The Tabor parameter μ ranges from 0.04 related to DMT-like to 3.24 JKR-like behavior, while $\widehat{\delta}_l$ extends up to 100. The color gradient in this cuboid qualitatively encodes computational cost, with deeper red tones indicating higher

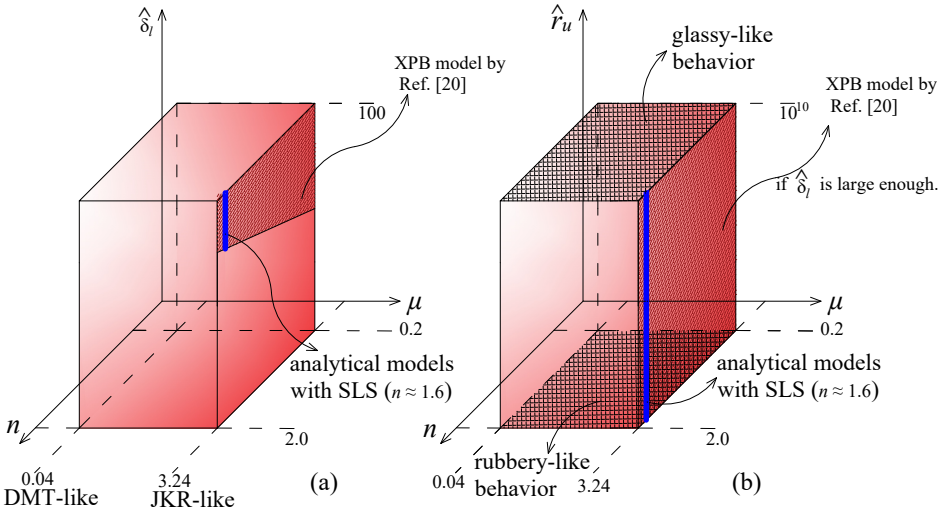

Figure 5.3: Visualization of the material exploration space represented schematically through cuboid shapes in a multi-dimensional parameter space (minimum values of $\widehat{\delta}_l$ and $\widehat{r}_u$ are $10^{-2.2}$ and $10^{-1.5}$ respectively). The figure highlights specific regions: the glassy-like and rubbery-like regions (checkered pattern), the XPB analytical model region (hatched plane), and the analytical models based on Standard Linear Solid (SLS shown as blue line). The space is color-coded to qualitatively indicate computational cost, with intense color representing high computational expense and lighter shades indicating easily computable configurations: (a) Hypercuboid in the (n, μ, $\widehat{\delta}_l$) space and (b) hypercuboid in the (n, μ, $\widehat{r}_u$) space. (From Ref. [81])

expense, particularly for large $\widehat{\delta}_l$ and large μ which implies fine spatial and temporal discretization as well as an extended time span. The blue vertical line at $n \approx 1.6$ identifies the region where SLS analytical models remain valid. The hatched surface indicates the domain in which the XPB model is applicable, specifically in the saturated indentation regime. The right cuboid in Figure 5.3 spans n, μ, and the normalized unloading rate $\widehat{r}_u$, which varies from very slow unloading ($\widehat{r}_u = 10^{-1.5}$), close to pure rubbery-like behavior, to extremely rapid unloading ($\widehat{r}_u = 10^{10}$) to capture the glassy behavior. As detailed in Appendix VII, the minimum indentation value in the samples, $\widehat{\delta}_l$, is $10^{-2.2}$. The hatched plane face marks the validity of the XPB model [19] when $\widehat{\delta}_l$ is sufficiently large (not shown in this projection), and the blue vertical line again indicates where the SLS approximation holds across all values of μ and $\widehat{r}_u$. However, substantial portions of the parameter space remain outside the validity limits of XPB [19].

5.3.2 Machine learning framework for tabular data

ML for tabular data applies algorithms to structured datasets organized in rows (samples) and columns (features) to analyze and predict outcomes. In supervised learning, models trained on labeled data map inputs to outputs, predicting continuous

values for regression tasks by minimizing errors, often using Mean Squared Error (MSE) loss. Data is split into training, validation, and test sets: the training set is used for model parameter optimization, validation set ensures overfitting preventions. Finally, the test set evaluates the model's performance on unseen data, providing an unbiased assessment of its predictive capabilities. This structured approach promotes effective learning and reliable performance in practical applications. The data processing and modeling workflow employed in this study is outlined in Figure 5.4.

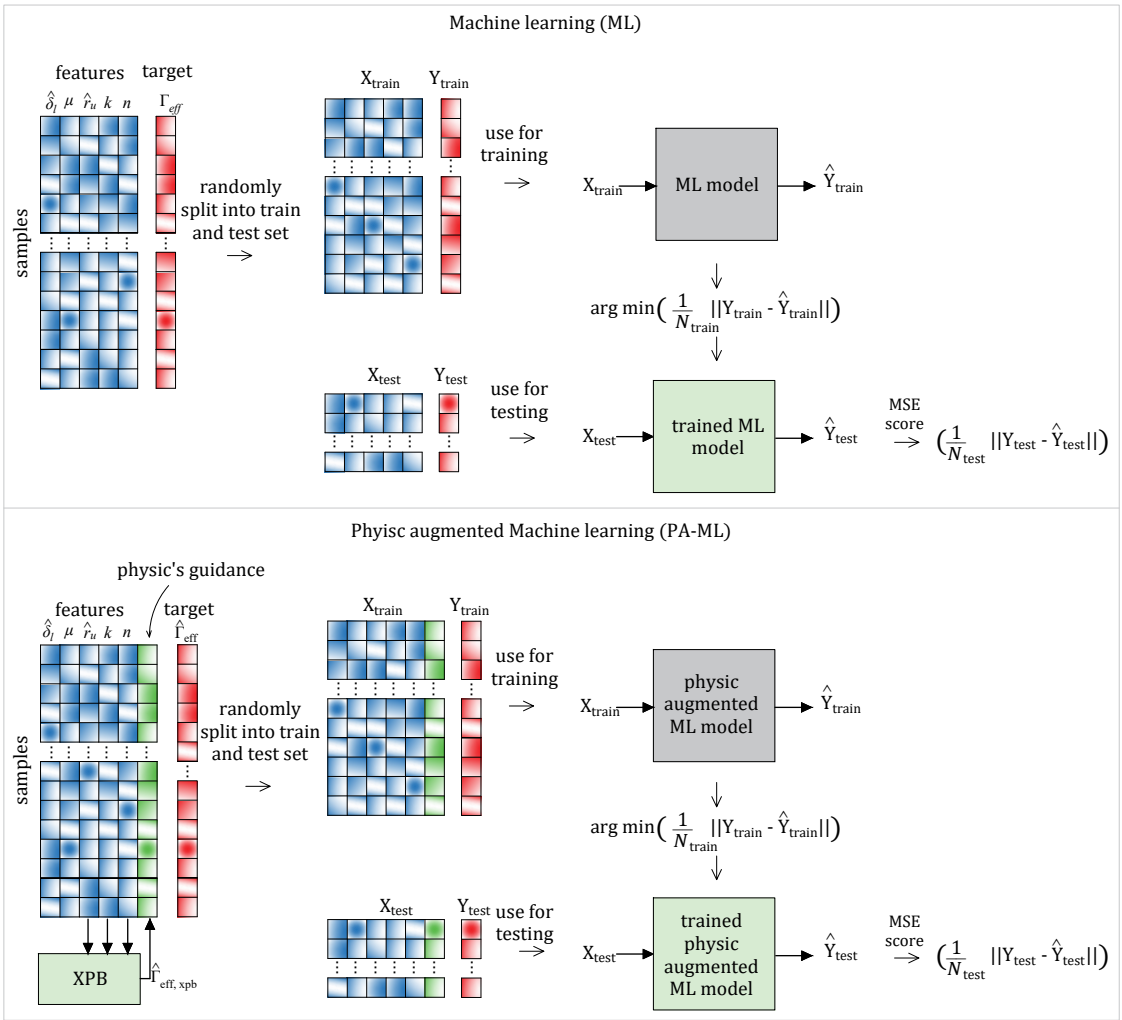

Figure 5.4: Schematic representation of the data processing and modeling workflow. The tabular data are partitioned into train and test datasets. The standard model is trained using the training set by minimizing the MSE objective function. The physics-augmented model incorporates the analytical XPB framework during training to enhance model accuracy and generalization. The performance of each model is evaluated on the test set using MSE as the scoring metric. (From Ref. [81])

The work at hand is characterized by tabular data, as described in Section 5.2

where one can see the inputs as the Tabor parameter μ, material exponent n, modulus ratio k, normalized indentation depth $\widehat{\delta}_l$, normalized unloading rate $\widehat{r}_u$ and output parameters would be the key characteristics of pull-off ($\widehat{\Gamma}_{eff}$ or $\widehat{w}_{po}$). Moreover, our work faces the challenge of small and sparse data due to the computational efforts related to obtaining numerical solutions in regimes where the XPB model is valid. The total number of data samples used in this work does not exceed 8505, making the use of classical ML models efficient and practical. The descriptive statistics of the dataset, including measures of central tendency, variability, and data transformations, are provided in Appendix VII.

In this section, for the prediction of effective surface energy and the work to pull-off, we utilize a linear regression model as a trivial baseline and tree-based ensemble methods for building the data-driven predictive models. Specifically, we compare regression trees, random forest regressors, and Extreme Gradient Boosting (XGBoost) models using k-fold cross-validation. See Appendix VI for more details on each of the ML models. We note that physical augmentation can be achieved in various ways [93]. In this work, we use the analytical XPB model to make predictions based on the parameters k, n, and $\widehat{r}_u$. These analytical results are fed as an additional input to the data-driven model. As shown in Figure 5.3, the XPB predictions are only valid at the *edges* of the variable space, where the hypotheses of short-range adhesion hold and the initial indentation depth is large enough to prevent finite-size effects. Nonetheless, they can still serve as a rough estimate of the effective surface energy. In our physics-augmented model, we denote this XPB estimate as $\widehat{\Gamma}_{\text{eff,xpb}}$. This quantity is derived from Equation 5.1 and introduced as an auxiliary variable representing a coarse approximation of the effective surface energy. Thereby, the model has to learn to compensate for the error of the analytical formulation in regimes where the XPB is inadequate. The training process of the physics-augmented model, incorporating data augmentation through XPB, is depicted in Figure 5.4.

5.4 Results

5.4.1 Results for effective surface energy prediction

This section compares two model families for predicting viscoelastic behavior. The first is a data-driven model with five input parameters (denoted as ML), while the second incorporates an additional input from the analytical XPB model, making it a physics-augmented (denoted by PA-ML) model with six inputs. Both models are trained using Linear Regression, Regression Tree, Random Forest, and XGBoost.

Their performance is assessed via 5-fold cross-validation, and the best model is tested on unseen data. The subsections cover the data-driven model first, followed by the physics-augmented model.

Table 5.1 summarizes the performance of various ML models in terms of MSE and R^2 values (mean $\pm$ standard deviation), with MSE scaled by 10^{-3}, along with model sizes, i.e. number of trainable parameters. The results in Table 5.1 highlight the trade-offs between performance and model complexity across the four ML models. Linear Regression exhibits the highest MSE and the lowest R^2 under cross-validation, indicating limited predictive accuracy. In contrast, ensemble-based models, such as Random Forest and XGBoost, achieve significantly lower MSEs and higher R^2 values, with XGBoost showing the best performance. We note that this superior performance comes with increased model complexity. However, XGBoost has a smaller model size compared to Random Forest, despite its excellent predictive capability. More details on the performance of the data-driven models are given in Appendix VI. From now on, references to ML for $\widehat{\Gamma}_{\text{eff}}$ prediction will specifically refer to the XGBoost model.

Table 5.1: Performance of ML approaches for the prediction of effective energy surfaces: MSE and R^2 values (mean $\pm$ std. deviation), with MSE reported as $\cdot 10^{-3}$ obtained from 5-fold cross-validation model and model sizes as number of trainable parameters included.

	MSE ($\cdot 10^{-3}$)	$\mathbf{R^2}$	**model size**	**train time (s)**
Linear Regression	19.1948 ± 0.7166	0.8384 ± 0.0047	6	0.0026
Regression Tree	0.3502 ± 0.0996	0.9970 ± 0.0008	6457	0.0217
Random Forest	0.2155 ± 0.0874	0.9982 ± 0.0007	416700	1.5508
XGBoost	0.1449 ± 0.0411	0.9988 ± 0.0003	4993	0.9959

The best-performed model (XGBoost) is utilized to predict the effective surface energy within the training data regime, but also outside that regime. This approach aims to evaluate the model's out-of-sample generalization. As discussed in Section 5.2, the computational costs of obtaining numerical samples for high values of indentation depth and large Tabor parameter are substantial. Additionally, the numerical model is sensitive to low values of n. For instance, when $n \leq 0.2$, our computational model fails to determine the pull-off force for cases where $\widehat{\delta}_l \geq 73$ and $\mu \geq 3.24$ at a reasonable computational cost. Figure 5.5(a) displays the ML-predicted results for effective surface energy (represented by circle dots) compared with the XPB model solution (depicted with dashed lines). Notably, Figure 5.5 represents a specific subset of the parameter space, specifically for $\hat{\delta}_{\text{load}} = 73$ and $\mu = 3.24$. The data-driven model predictions closely resemble those of the analytical model, even for $n = 0.2$, despite the absence of training data in this parameter range. However, a closer look at the results for $n = 0.2$ reveals deviations from the analytical predictions provided

by XPB. This indicates that while the ML model generalizes to unseen data, its accuracy weakens in regions where no prior information is available. In fact, this observation motivated us to incorporate physics-based augmentation to enhance the model's reliability in extrapolated scenarios.

Table 5.2 summarizes the performance of ML model on the physics augmented data for four algorithms, where XPB outputs are used as additional input features. The MSE and R^2 are evaluated as summarized in Table 5.2. The results demonstrate that tree-based models significantly outperform linear regression in terms of both accuracy (lower MSE and higher R^2) and robustness (lower standard deviation). This time, Random Forest achieves the best performance. XGBoost and Regression Tree models also show comparable performance, with only marginal differences in MSE and R^2 values, though the Random Forest exhibits substantially larger model sizes. The results in Table 5.2 are further supported by Figure A.5 in Appendix VI.

Comparing Table 5.2, which presents the performance of the PA-ML approach, with the pure data-driven ML results in Table 5.1 reveals a significant reduction of 60.3% in the mean of MSE across the folds. However, note that the primary goal of physics augmentation is not merely to reduce error on seen data but to enhance generalization beyond unseen data, as illustrated in Fig. 5.5(a) and (b). The best ML model in Table 5.1 is XGBoost with a size of 4993, while the corresponding PA-ML approach in Table 5.2 has a size of 4636, resulting in a 7.15% reduction. This trend is also observed in Regression Tree model, which shows size reductions of 0.22%. However, for the PA-ML models the best performance is achieved by Random Forest, while this performance is achieved at the cost of the increase in the model size. Hence, all subsequent references to PA-ML for $\widehat{\Gamma}_{\text{eff}}$ prediction will specifically refer to the Random Forest model.

The key aspect of Figure 5.5 is that the XPB model remains valid in this region, enabling a meaningful comparison between the purely data-driven ML approach and the PA-ML approach. This comparison is illustrated in Figures 5.5(a) and (b), where the circular data points represent ML predictions, and the dashed points correspond to XPB results. In regions with sufficient training data (n = 0.6 and n = 1.6, particularly at high unloading rates), both models align well with XPB. However, deviations become more pronounced in areas with data scarcity. Notably, the red data points correspond to n = 0.2, a region where no training data is available ; yet, the ML model gives a fairly good representation of system behavior. In this challenging regime, the purely data-driven model (Figures 5.5(a)) exhibits deviations from XPB, while the PA-ML model (Figures 5.5(b)) produces smoother and more accurate predictions, demonstrating its superior generalization beyond the training

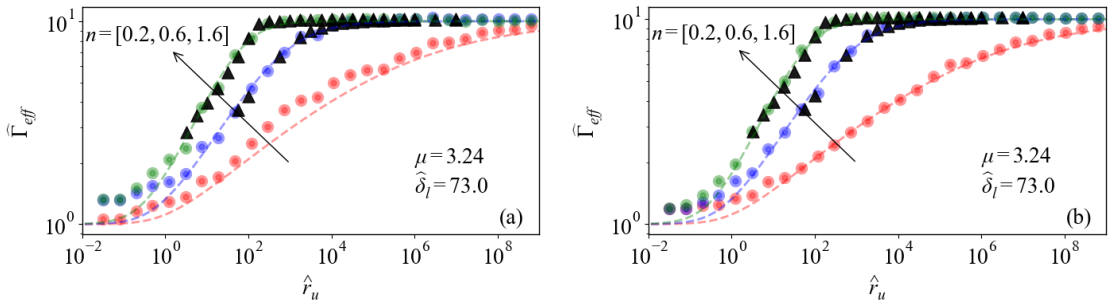

Figure 5.5: Comparison of the predictions from the purely data-driven machine learning (ML) approach (XGBoost) and the physics-augmented machine learning (PA-ML) approach (Random Forest) for the relationship between normalized surface energy and unloading rate. The dashed lines represent the XPB solution, triangle markers indicate the training data, and circles denote the predictions from the ML models. The models are evaluated for the parameters $\mu = 3.24$, $\widehat{\delta}_{\text{load}} = 73$, $k = 0.1$, and for three values of $n = [0.2, 0.6, 1.6]$: (a) results from the purely data-driven ML model (XGBoost had the best performance) and (b) results from the PA-ML model (Random Forest had the best performance). (From Ref. [81])

set. The PA-ML model predictions closely align with the XPB analytical solution at $k = 0.1$, the most representative value in the training set (see Appendix VII). We further evaluated the model against XPB across the range $k = 0.5$ to $k = 0.02$; nevertheless, it reliably captures the overall trend down to $k = 0.02$.

To gain insights into how variations in physical parameters influence the computational cost of numerical simulations, and highlight the computational efficiency offered by ML models, we present details of computational costs from the dataset. Using our BEM-based numerical simulations implemented in MATLAB 2023b on a desktop computer equipped with Windows 11 pro, a 12th Gen Intel(R) Core(TM) i9-12900K, 3200 Mhz, 16 Cores, and 96 GB RAM, the CPU computation time exhibits significant variability depending on the complexity of the physical inputs. Throughout 8505 simulations, the average simulation time was 1.76×10^3 s, with a skewed distribution. The total computational time is $\approx 1.66 \times 10^7$ s, which corresponds to approximately 12 days of parallel runtime on a 16-core machine. The normalized maximum-to-minimum simulation time ratio was $\approx 1.06 \times 10^5$, indicating a substantial variability in computational cost. This variability is strongly influenced by the input parameters. In particular, an increase in either μ or $\widehat{\delta}_l$, or a decrease in n, k, or $\hat{r}_u$, tends to result in longer simulation times. In contrast, predictions generated by our trained PA-ML models, evaluated in Python 3.12 on a laptop with an Intel i7-6700HQ CPU, 16 GB RAM, running Windows 10, remained consistently below 5 milliseconds per inference across all explored parameter combinations. This demonstrates that ML models provide nearly instantaneous predictions. Hence, ML-

based models offer computational efficiency independent of the complexity inherent in the input parameters.

Table 5.2: Performance of PA-ML approaches for the prediction of effective energy surface: MSE values (scaled by 10^{-3}) are presented as mean ± standard deviation, along with R^2 values obtained from 5-fold cross-validation and model sizes.

	MSE ($\cdot 10^{-3}$)	$\mathbf{R^2}$	**model size**	**train time (s)**
Linear Regression	16.7658 ± 1.0776	0.8586 ± 0.0102	7	0.0029
Regression Tree	0.1355 ± 0.0796	0.9989 ± 0.0007	6443	0.0282
XGBoost	0.0977 ± 0.0824	0.9992 ± 0.0007	4636	0.1204
Random Forest	0.0575 ± 0.0247	0.9995 ± 0.0002	417800	2.0387

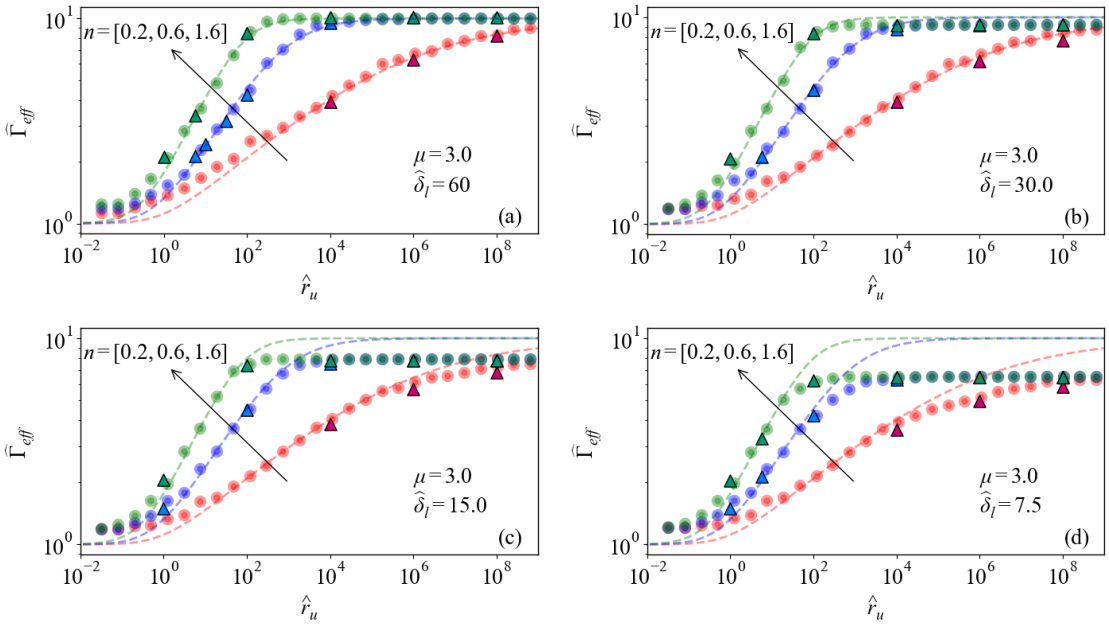

Figure 5.6: Impact of indentation depth on rate-dependent effective surface energy, evaluated at a fixed Tabor parameter ($\mu = 3.0$), material modulus ratio ($k = 0.1$), and for three values of the power-law exponent $n = [0.2, 0.6, 1.6]$. Predictions from the PA-ML model are shown as circular markers, XPB analytical results as dashed lines, and test BEM results are represented by triangular markers. Subplots correspond to: (a) $\widehat{\delta}_l = 60$; (b) $\widehat{\delta}_l = 30$; (c) $\widehat{\delta}_l = 15$; and (d) $\widehat{\delta}_l = 7.5$. (From Ref. [81])

What we have accomplished so far is the development of a model that performs relatively well in regions where numerical results are unavailable. Note that BEM results are shown as black diamonds in Figure 5.5, and BEM results are displayed only for the range $n \in [0.6, 1.6]$, as lower values become numerically demanding. Exponents close to $n = 0.2$ are typical of broadband materials such as PDMS, commonly used in soft contact mechanics studies [19]. The parameter set illustrated in Figure 5.5 features both a large Tabor parameter and a large indentation. In this

regime, the XPB model accurately reproduces the numerical results; thus, XPB can be reliably used as a proxy for the ground truth. To understand the advantages of the ML models over the XPB model, one should examine its results in regions where XPB does not apply, particularly where μ and $\widehat{\delta}_l$ are low. According to Figure 5.6, XPB is only valid for high values of the Tabor parameter and high indentation depth (as seen in Figure 5.6(a)). In contrast, Figure 5.6(b), (c) and (d) clearly indicate that XPB fails at higher unloading rates, whereas the PA-ML results remain well-aligned with test data (triangular nodes obtained through BEM). By comparing Figures 5.6(a) to (d), where the indentation depth decreases from $\widehat{\delta}_l = 60$ to $\widehat{\delta}_l = 7.5$, it is evident that the maximum viscoelastic amplification decreases as the indentation depth is reduced. Consequently, ML models serve as a valuable intermediary, particularly in regimes where analytical models (XPB) prove inadequate and numerical models (BEM) become computationally prohibitive. While XPB becomes not accurate outside its valid range, BEM, despite its accuracy, becomes excessively expensive and impractical in certain parameter regimes due to exponential increases in computational cost and numerical instabilities at extreme unloading rates or indentation depths.

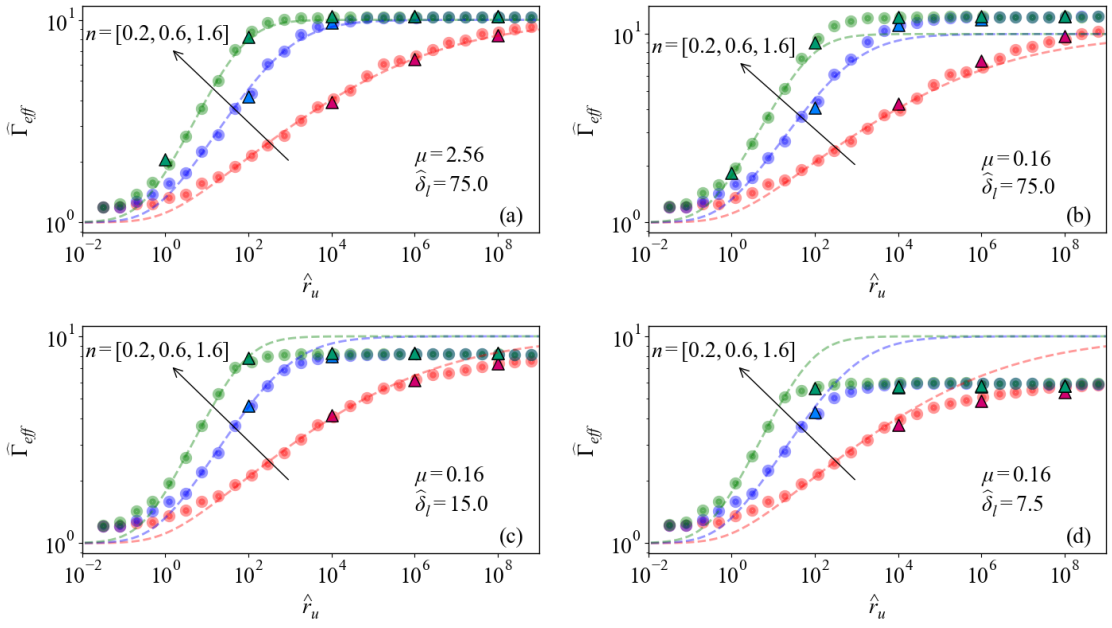

Figure 5.7: The transition from JKR to DMT behavior captured by the PA-ML model for varying Tabor parameter values material modulus ratio ($k = 0.1$), and for three values of the power-law exponent $n = [0.2, 0.6, 1.6]$. Circular dots represent the PA-ML predictions, the dashed lines are the XPB solution, and the triangular markers denote the test BEM results. Subplots correspond to: (a) $\mu = 2.56$, $\widehat{\delta}_l = 75$; (b) $\mu = 0.16$ $\widehat{\delta}_l = 75$; (c) $\mu = 0.16$ and $\widehat{\delta}_l = 15$; and (d) $\mu = 0.16$, $\widehat{\delta}_l = 7.5$. (From Ref. [81])

We investigate the effect of varying the Tabor parameter on effective surface energy as a function of $\hat{r}_u$ for a constant indentation depth to evaluate the performance of

PA-ML and compare its results with those of XPB, as shown in Figure 5.7. The XPB predictions is represented by dashed lines, and the BEM results are shown by triangular nodes as test data. For an indentation depth of $\widehat{\delta}_l = 75$ and Tabor parameter values ranging from $\mu = 2.56$ to $\mu = 0.16$ in Figures 5.7(a) to (b), a transition from JKR to DMT behavior is observed. This transition is not captured by the XPB model but is accurately detected by the PA-ML model. Also, Figures 5.7(c) and (d) show that the model could consider the indentation depth effect in the DMT regime. Nevertheless, deviations appear in the region of low unloading rate. This is due to the scarcity of training data available at a low unloading rate.

Furthermore, we leveraged our PA-ML model to provide more insight into the interdependence of indentation depth ($\widehat{\delta}_l$) and the Tabor parameter (μ), as illustrated in Figure 5.8. In Figure 5.8, the black dashed-dotted line represents the upper bound for DMT-like behavior, which is equal to $\frac{4}{3k} = 40/3$ [26, 182], while the JKR-like limit ($1/k = 10$) is indicated by the mild brown dashed-dotted line. The XPB prediction is depicted by the dashed gray line, demonstrating its independence from variations in μ and $\widehat{\delta}_l$. We present the results for a very high unloading rate ($\widehat{r}_u = 10^9$) and a specific value of the material power law exponent ($n = 0.6$) in Figure 5.8(a), which illustrates the highest achievable adhesion as a function of indentation depth and μ. This point was briefly addressed in our previous study [19], where it was noted that achieving adhesion is not solely a function of the unloading rate; the indentation depth also plays a significant role in determining the effective surface energy and, consequently, the adhesion. Here, we demonstrate the interdependence of $\widehat{\delta}_l$ and μ through our PA-ML predictions. It is important to note that for all cases similar to Figure 5.8(a), where $k = 0.1$, $n = 0.6$, and the unloading rate is $\widehat{r}_u = 10^9$, the XPB model consistently predicts a value equal to the JKR limit of $1/k = 10$.

From Figure 5.8(a), it can also be deduced that for lower values of indentation depth, an increase in μ results in a growth in the effective surface energy. Conversely, for higher values of indentation depth, an increase in the μ parameter leads to a reduction in the effective surface energy, transitioning from a DMT-like limit to a JKR-like limit. Hence, one can deduce that the Tabor's effect is not uniform, which means the depth-dependent Tabor effect on adhesion.

Considering Figure 5.8(b), where we plotted the results for mid values of the unloading rate, it can be deduced that all scenarios corresponding to different values of μ for high values of indentation depth converge to a plateau equal to the XPB results, which is lower than both the JKR-like and DMT-like limits. Additionally, it is evident that for lower values of indentation depth, the dependency on the Tabor parameter persists, and for higher values of μ, our PA-ML models predict higher adhesion.

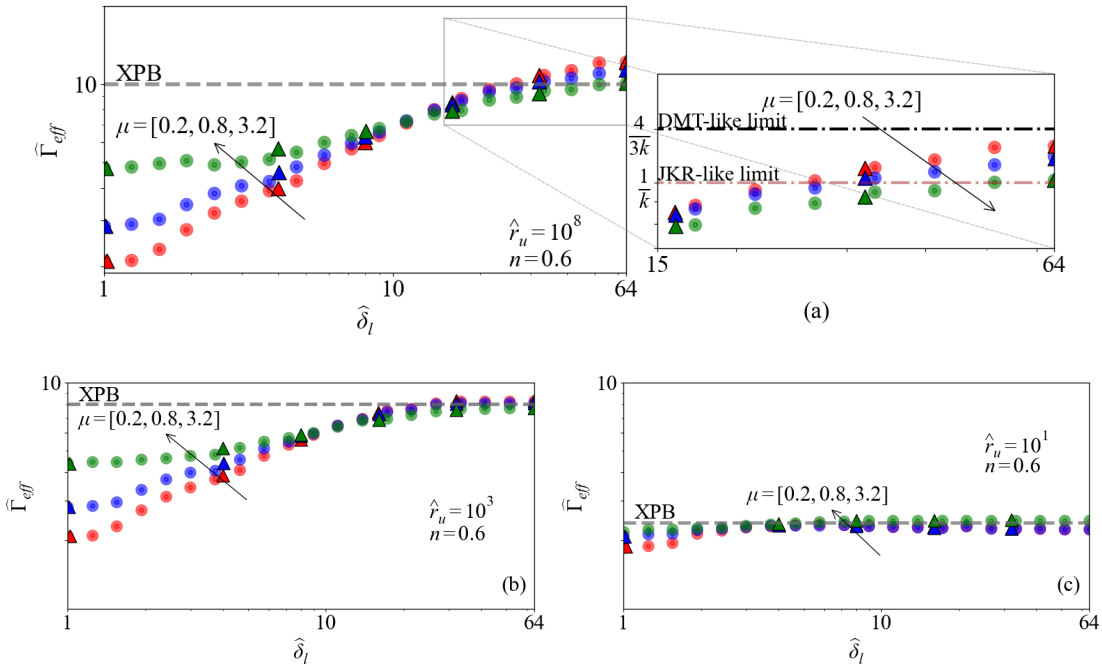

Figure 5.8: PA-ML model (Random Forest): Normalized surface energy versus indentation depth for different values of $\mu = [0.05, 0.2, 0.8, 3.2]$. Dash-dotted lines represent the JKR limit (which is equal to $\frac{1}{k}$)[19] and DMT limit (which is $\frac{4}{3k}$) [182], gray dashed line indicates the XPB results, circular dots correspond to the BEM solution, and the solid lines indicate the PA-ML predictions for (a) $\hat{r}_u = 10^8$, $n = 0.6$, $k = 0.1$; (b) $\hat{r}_u = 10^3$, $n = 0.6$, $k = 0.1$; (c) $\hat{r}_u = 10^1$, $n = 0.6$, $k = 0.1$. The results indicate that the JKR and DMT limits were only achieved with high indentation depth values and very high unloading rates. (From Ref. [81])

Furthermore, Figure 5.8(c) shows that at low unloading rates (here, $\hat{r}_u = 10$), the effective surface energy remains almost independent of indentation depth and the Tabor parameter, yielding results aligned with the XPB model predictions.

5.4.2 Results for prediction of work to pull-off

To gain insight into the energy required to detach a sphere from a viscoelastic surface, one can refer to the concept of work to pull-off $w_{\text{po}} = \int_{\delta_{\text{on}}}^{\delta_{\text{po}}} P(\delta, t)\, d\delta = \hat{w}_{po}(1.5\pi\Delta\gamma_0 R h_0)$, where δ_{on} is the displacement at which the normal force first becomes zero during unloading, and δ_{po} denotes the displacement at pull-off [17] as shown in Figure 5.2. We employed the same approach and architecture of surrogate ML models used for predicting effective surface energy, but adapted it for the prediction of normalized work to pull-off. For the pure data-driven ML approach, we again utilized five inputs, as outlined in Figure 5.4, but with $\hat{w}_{po}$ as the output representing the work to pull-off, and for PA-ML, we followed a similar approach to the previous PA-ML implementation, but with a different output target.

The performance results of the ML and PA-ML are presented in Tables 5.3 and 5.4. Consistent with the findings in Tables 5.2, Random Forest exhibits the best performance among the algorithms for predicting the work to pull-off, achieving R^2 of 0.9945 ± 0.0025 across five folds. Consequently, we illustrate the prediction results of the work to pull-off through Random Forest for a wide range of unloading rates and power law exponents in Figure 5.9, and all subsequent references to ML and PA-ML for $\widehat{w}_{\text{po}}$ prediction imply the use of Random Forest.

Table 5.3: Performance of ML approaches for the prediction of work to pull-off ($\widehat{w}_{po}$): MSE and R^2 values (mean ± std. deviation) obtained from 5-fold cross-validation, with MSE reported as $\cdot 10^{-3}$ and model sizes included.

	MSE ($\cdot 10^{-3}$)	$\mathbf{R^2}$	**model size**	**train time (s)**
Linear Regression	51.4637 ± 12.5943	0.9062 ± 0.0227	6	0.0019
Regression Tree	4.6163 ± 2.0924	0.9916 ± 0.0038	6503	0.0241
XGBoost	3.1094 ± 1.8688	0.9943 ± 0.0035	4766	0.1184
Random Forest	2.9948 ± 1.3544	0.9945 ± 0.0025	419700	1.4867

Table 5.4: Performance of PA-ML approaches for the prediction of work to pull-off ($\widehat{w}_{po}$): MSE and R^2 values (mean ± std. deviation) obtained from 5-fold cross-validation, with MSE reported as $\cdot 10^{-3}$ and model sizes included.

	MSE ($\cdot 10^{-3}$)	$\mathbf{R^2}$	**model size**	**train time (s)**
Linear Regression	51.1512 ± 12.5556	0.9067 ± 0.0226	7	0.0017
Regression Tree	4.0330 ± 2.0619	0.9926 ± 0.0037	6493	0.0285
XGBoost	2.9248 ± 1.8478	0.9946 ± 0.0034	4954	0.1267
Random Forest	2.4197 ± 1.2864	0.9956 ± 0.0023	419400	2.0190

Figure 5.9 demonstrates that the work to pull-off versus the unloading rate exhibits a different behavior compared to the effective surface energy. Unlike the effective surface energy, the work to pull-off follows a bell-shaped curve as a function of the unloading rate as also have been shown in a work by full numerical modeling [17]. The results in Figure 5.9 reveal an interacting effect between the unloading rate and the power law exponent on the work to pull-off, which was not observed in the results for the effective surface energy. Specifically, for relatively lower values of the unloading rate, an increase in the power law exponent leads to a rise in the work to pull-off, whereas for higher values of the unloading rate, our PA-ML model predictions indicate that an increase in the power law exponent results in a decrease in the work to pull-off.

It is important to note that, to date, there has been no analytical model capable of describing the work to pull-off the concept across any range of material variables.

Therefore, for physical augmentation in our PA-ML and the prediction of work to pull-off, we decided to utilize the XPB model's output. In the following results, we aim to evaluate the effect of incorporating the outputs of the XPB model—specifically, the effective surface energy—on the prediction of a distinct parameter, as the effective surface energy is expected to positively correlate with work to pull-off.

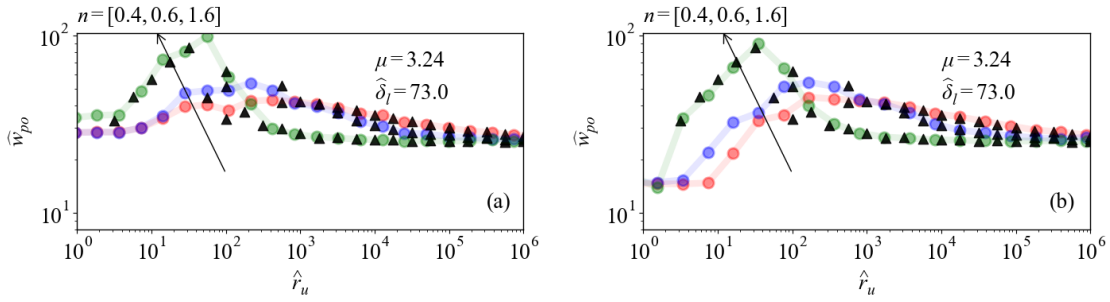

Figure 5.9: Comparison of (a) a purely data-driven ML model (Random Forest) and (b) a physics-augmented ML model (PA-ML Random Forest) in predicting the relationship between normalized work to pull-off and unloading rate. Triangle markers represent the training data, circles denote model predictions. Results are evaluated for $\mu = 3.24$, $\widehat{\delta}_{\text{load}} = 73$, $k = 0.1$, and power-law exponents $n = [0.4, 0.6, 1.6]$. (From Ref. [81])

According to our results, Random Forest performs better than the other algorithms in terms of MSE, R^2. The most notable observation from Table 5.4 is the significant impact of augmentation through the effective surface energy ($\widehat{\Gamma}_{eff}$ based on XPB) on the performance of algorithms in predicting the work to pull-off ($\widehat{w}_{po}$). A comparison between Table 5.4 and Table 5.3 reveals the influence of incorporating this physical parameter as an additional input into the modeling process. The results indicates that augmentation consistently reduces prediction errors and enhances performance, as evidenced by improvements in both MSE and R^2. Additionally, the model sizes of Random Forest reported in Table 5.3 and 5.4 suggest that the integration of XPB improves predictive accuracy.

To visually assess the effect of XPB for guiding the PA-ML model for prediction of work to pull-off, we illustrate the predictions of Random Forest across a wide range of unloading rates and varying values of the power law exponent in Figure 5.9(b). This figure is structured similarly to Figure 5.9(a), where the circles represent the PA-ML predictions, and the triangle markers denote the training data. A comparison between Figures 5.9(a) and 5.9(b) reveals that the PA-ML model provides predictions that are closer to the BEM solutions and demonstrate smoother behavior.

To gain insight into different slices of the material behavior space and to examine the effects of input parameters on the material's behavior, we leveraged our PA-ML model to explore the effect of the Tabor parameter (μ) in Figure 5.10. The results are

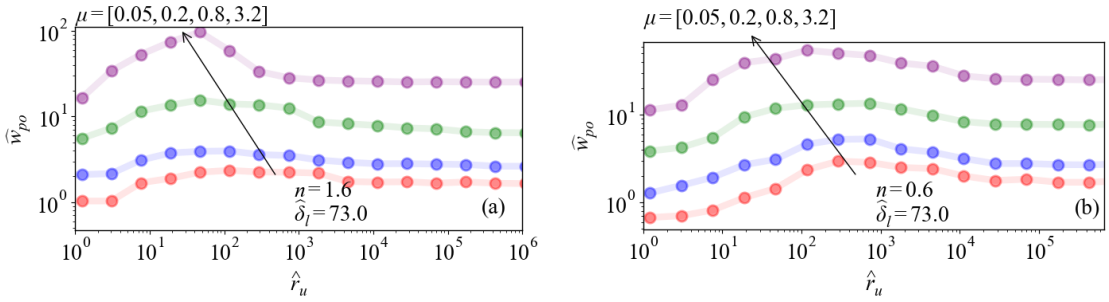

Figure 5.10: PA-ML model (Random Forest): Normalized work to pull-off as a function of unloading rate for different values of the Tabor parameter (μ = [0.05, 0.2, 0.8, 3.2]), at a fixed indentation depth $\widehat{\delta}_l = 73.0$ and material modulus ratio $k = 0.1$. Circular markers represent predictions from the PA-ML model. Results are shown for two power-law exponents: (a) $n = 1.6$ and (b) $n = 0.6$. (From Ref. [81])

presented as a function of unloading rate and two specific values of the material power law exponent ($n = 1.6$) in Figure 5.10(a), as well as for $n = 0.6$ in Figure 5.10(b). The work to pull-off consistently increases as μ increases in both Figure 5.10(a) and Figure 5.10(b). To ensure the validity of the ML predictions, we provide analytical estimations of the upper and lower bounds for the work to pull-off in Appendix VIII and Appendix IX, respectively.

5.5 Toward prediction of adhesion trajectories through neural networks

The surrogate models presented so far predict scalar endpoint quantities, including pull-off force, effective surface energy, work to pull-off. However, many applications require not just endpoints but the *full time-resolved evolution* of the adhesive force during unloading (see Fig. 5.2). Predicting entire trajectories introduces two additional challenges: (i) *unknown and varying end times:* each sample detaches at its own unknown pull-off time, leading to output sequences of different lengths and sparsity (force becomes zero after pull-off); (ii) *extreme temporal resolution requirements:* to capture the fastest detachment events, all trajectories must be discretized with a very fine time step $\Delta t_{\min}$, resulting in an impractically large output dimensionality. To address these issues, we develop a feed-forward neural network model that, rather than predicting every time step, takes as input the displacement protocol features, geometry, and material properties, and predicts a fixed, prescribed number of key points along the unloading curve, thus balancing temporal detail with model efficiency.

Based on our BEM model, we generated a dataset of 8505 samples covering

a broad range of viscoelastic and adhesive behaviors. The power-law exponent n spans from 0.2 (wide-band, rubbery behavior typical of PDMS) to 2.0 (narrow-band response). The Tabor parameter μ ranges from 0.04 (DMT-like) to 3.24 (JKR-like), while the normalized indentation depth $\widehat{\widehat{\delta}}_l$ reaches up to 100. The normalized unloading rate $\widehat{r}_u$ varies from $10^{-1.5}$ (slow, rubbery response) to 10^{12} (fast, glassy response).

5.5.1 Feed-forward neural network

The feedforward neural network (FNN) could be considered as a function $\hat{y} = F(\mathbf{x}; \theta)$ [183], where $\mathbf{x}$ is the input vector and θ represents the model parameters, including all weights and biases across layers. Here, the model is trained using the mean squared error (MSE) loss function, given by

$$J(\theta) = \frac{1}{N} \sum_{i=1}^{N} \left(F(\mathbf{x}^{(i)}; \theta) - y^{(i)} \right)^2$$

where N is the number of training samples, $\mathbf{x}^{(i)}$ is the input, and $y^{(i)}$ is the true label for the i-th sample. The training objective is to find the optimal parameters θ^* that minimize the loss:

$$\theta^* = \arg\min_{\theta} J(\theta)$$

This optimization is typically performed using gradient-based methods. In this work, we use the Adam optimizer. To effectively train the neural network, the dataset is divided into three subsets: training, validation, and testing, in proportions of 70%, 15%, and 15%, respectively. The training set is used to update the network's weights, the validation set assists in hyperparameter tuning and overfitting prevention, and the test set evaluates the model's performance on unseen data to assess its generalization capability. The learning rate, an essential hyperparameter that dictates the step size for weight updates, was fixed at 0.001 throughout the training process.

5.5.2 Segmented trajectory estimation model

A straightforward approach to modeling the force trajectory is to use a sequential model that predicts the force at each time step with a small interval, $\Delta t_{\min}$, determined by the shortest pull-off time in the dataset. However, as the unloading rate varies over several orders of magnitude across the dataset, the corresponding pull-off times also span a wide range. This presents two main challenges: (i) the pull-off (detachment) point is not known a priori for each sample, resulting in output sequences

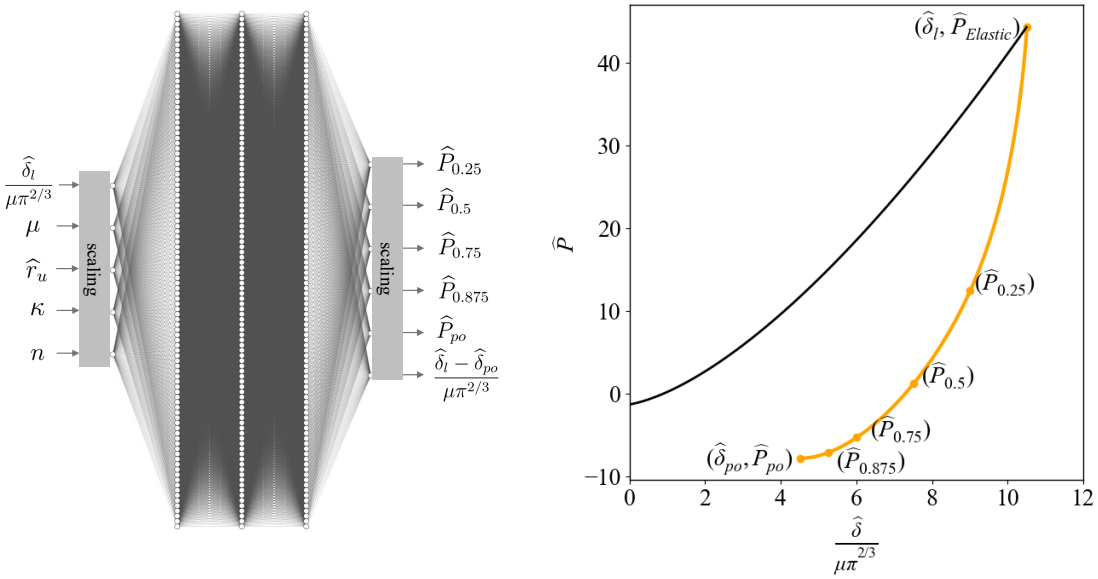

Figure 5.11: Load-displacement curve during the unloading of a Hertzian indenter from a viscoelastic substrate. The solid black line represents the JKR solution (elastic solution), while the orange dots highlight key features extracted from the viscoelastic unloading curve. These dots serve as the primary outputs for the neural network analysis.

of varying lengths; and (ii) to ensure accuracy, all samples must be discretized at the finest temporal resolution, leading to highly sparse outputs and a prohibitively large output dimensionality to accommodate the longest trajectories.

As it is shown in Figure 5.11, we propose a model that does not predict every time step. Instead, it takes input features from the displacement protocol ($\hat{\delta}_l$, and $\hat{r}_u$), geometry (μ), and material properties (k, and n). Then it predicts a fixed number of key points on the force trajectory. These points include the displacement until pull-off ($\hat{\delta}_l - \hat{\delta}_{po}$), where $\hat{\delta}_{po}$ denotes the normalized indentation at the pull-off (detachment) point, and force values at 25% ($\hat{P}_{0.25}$), 50% ($\hat{P}_{0.5}$), 75% ($\hat{P}_{0.75}$), 87.5% ($\hat{P}_{0.875}$), and 100% ($\hat{P}_{po}$) of the trajectory (see Figure 5.11). This method reduces complexity while still capturing essential unloading behavior. Other points can also be added to adjust the level of detail if needed.

5.5.3 Data preprocessing

A critical component of training the deep neural networks is the normalization and scaling of both inputs and outputs. All features and targets were standardized using the training set's mean and variance to ensure consistency and prevent data leakage during evaluation. Additionally, inspired by Maugis [9], indentation depth values were normalized by the Tabor parameter μ to maintain physical consistency

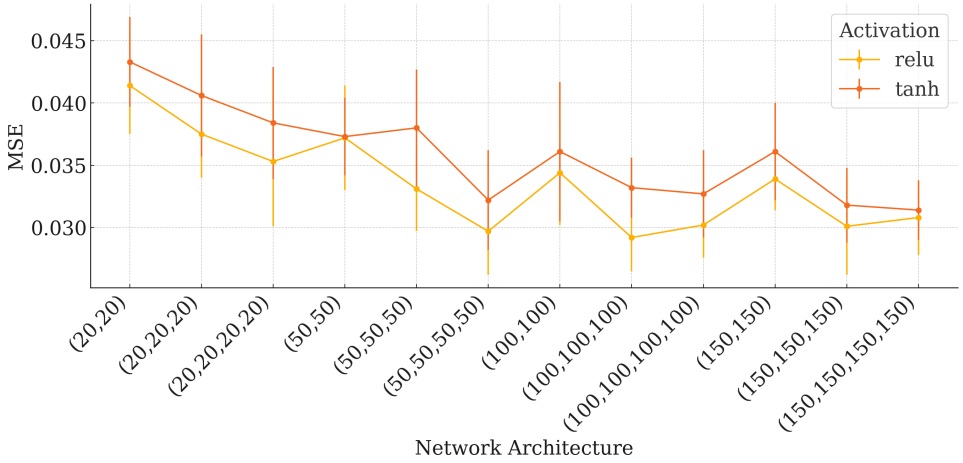

Figure 5.12: Cross-validation MSE by architecture and activation function (From Ref. [81])

with contact mechanics. A modified logarithmic transformation was also applied to parameters such as k, $\widehat{r}_u$, and the output forces to manage wide dynamic ranges and preserve the shape of the loading trajectory.

5.5.4 Results for trajectory prediction

The architecture of the neural network is a critical factor influencing model performance, particularly its ability to learn and generalize from data. In this study, we evaluated several architectures and selected the optimal configuration based on performance metrics. To prevent overfitting and ensure reliable model assessment, we employed k-fold cross-validation and monitored the MSE of training and validation during hyperparameter tuning. We use the MSE and its standard deviation across folds to identify the best combination of layers, neurons per layer, and activation functions as it is shown in Figure 5.12.

To evaluate the performance of our FNN in predicting sequential results, we plotted the load and indentation depth for different scenarios in Figures 5.13. The results are related to the (100,100,100) architecture shown in Figure 5.11. In Figures 5.13, the continuous solid curves represent the sequential solutions obtained through the BEM, while the dots correspond to the predictions from our FNN model. Figures 5.13(a) and 5.13(b) illustrate the relationship between load and indentation depth, whereas Figures 5.13(c) and 5.13(d) depict the evolution of load over time. Specifically, the scenarios in Figures 5.13(a) and 5.13(c) are identical, and the same applies to Figures 5.13(b) and 5.13(d).

We note that the predicted results through FNN are related to the load vs. displacement curve; however, time can be easily derived from the corresponding dis-

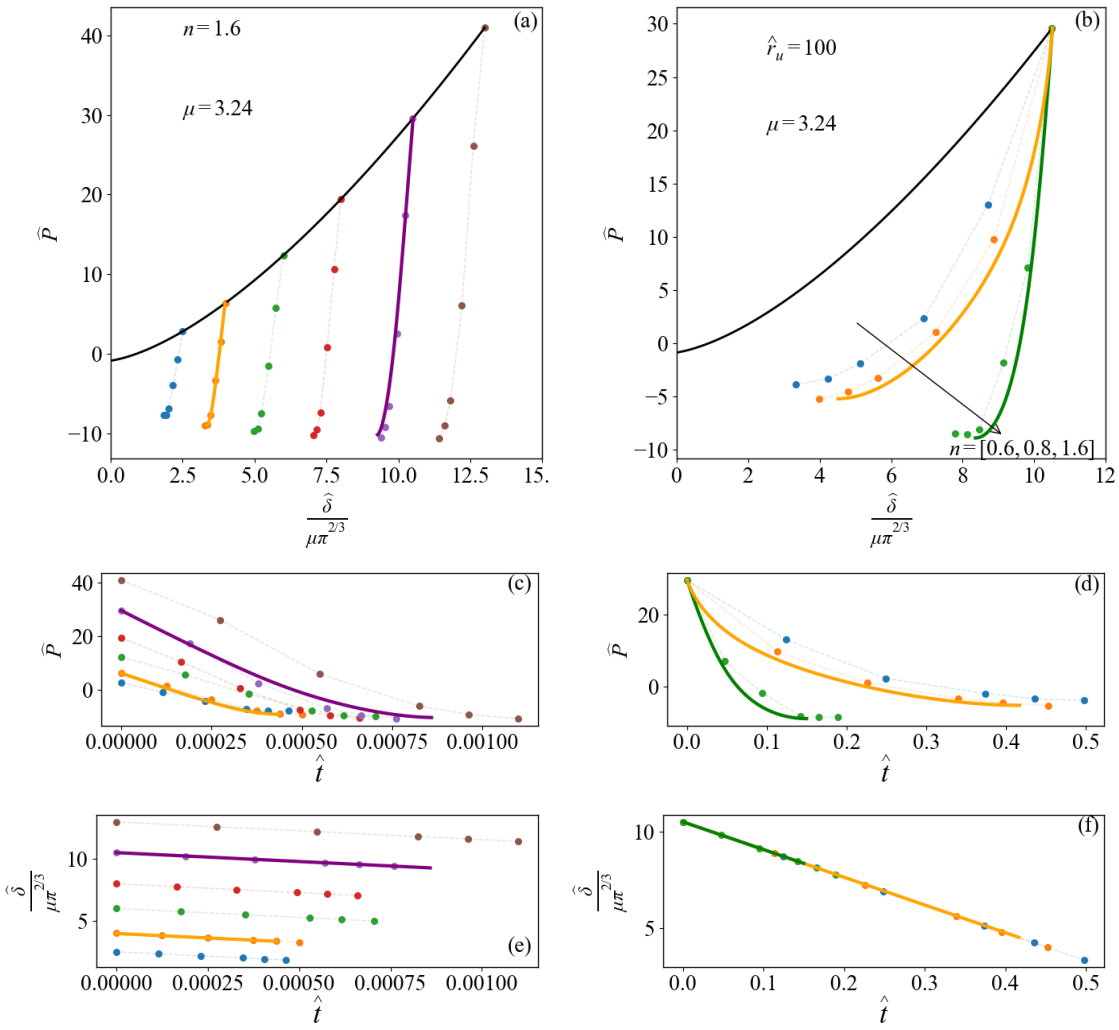

Figure 5.13: Sequential predictions of the FNN model across varying parameters: (a) Unloading trajectories on Load vs. indentation curves for $\widehat{r}_u = 10^5$, $n = 1.6$, $\mu = 3.24$, and indentation depths $\widehat{\delta}_l = [2.5, 4, 6, 8, 10.5, 13]\mu\pi^{2/3}$; (b) Unloading trajectories for $\widehat{r}_u = 10^2$, $\widehat{\delta}_l = 10.5\mu\pi^{2/3}$, $\mu = 3.24$, and power law exponents $n = [0.6, 0.8, 1.6]$; (c) Load vs. time for the same conditions as (a); (d) Load vs. time for the same conditions as (b); (e) Indentation depth vs. time for conditions matching (a) and (c); (f) Indentation depth vs. time for conditions matching (b) and (d). The solid black line represents the JKR solution, colored solid lines denote the BEM results used for training data, and dots indicate FNN predictions.

placement based on the unloading rate, as demonstrated in Figures 5.13(c) and 5.13(d). It is important to emphasize that the sequential results obtained through the FNN are generated instantly, unlike classical numerical solutions, which require continuous computing points along the trajectory one by one. This distinction highlights the efficiency and computational advantage of the FNN approach in predicting sequential behaviors. According to the plots in Figure 5.13, it can be observed that the shortest simulation time in the plots is less than 0.005 (as shown in Figure 5.13(c)), while the longest simulation time in the depicted plots exceeds 0.4 (as seen in Figure 5.13(d)). This indicates a significant difference in the timescales of the simulations. Despite this disproportionality in the dataset, our proposed model is capable of handling such variability, learning from the data, and making proper predictions.

5.6 Summary and conclusions

We introduced two ML-based approaches for predicting the pull-off force and work to pull-off of relaxed viscoelastic adhesive Hertzian contacts as a function of five input parameters of Tabor parameter μ, material power exponent n, modulus ratio k, unloading rate $\widehat{r}_u$, and the inidentation depth $\widehat{\delta}_l$. Based on 8505 samples generated through our BEM numerical framework, the pure data-driven ML models efficiently provide predictions in regions where computational costs are high. Notably, their strong agreement with our previously developed analytical model further validates their reliability and effectiveness. This confirms that the proposed approach could be seen as a bridge between analytical models and numerical methods. Through a systematic comparison, the study demonstrates that ML-based approaches, particularly tree-based methods like Random Forest, excel in predicting tabular data with low MSE and high R^2 values. The integration of ML with physics-based insights, particularly guided by the XPB model, developed by Maghami et al [19], enables the creation of efficient and accurate surrogate models for predicting key adhesion-related quantities, including effective surface energy and work to pull-off, especially where analytical models fail and numerical simulations become costly. Notably, the PA-ML models not only improve prediction accuracy but also, help generalization. Despite the distinct relationship between the work to pull-off quantity and effective surface energy, integrating XPB guidance, which provides the latter in a valid region, enhanced the prediction accuracy of the former overall. The PA-ML framework helped us to reveal interesting insights into the adhesion mechanics of viscoelastic materials. Particularly, the interplay between the Tabor parameter and indentation depth was clarified, showing a transition between DMT-like and JKR-like behaviors

under different conditions. A depth-dependent Tabor effect on adhesion is detected by our PA-ML. For low indentation depths, increasing the Tabor parameter led to a rise in effective surface energy. Conversely, at large indentation depths, low Tabor parameters result in a higher adhesion enhancement (see also Ref. [26]). PA-ML prediction showed that the work-to-pull-off exhibited different behavior from the effective surface energy, following a bell-shaped curve as a function of the unloading rate. The interacting effects of the unloading rate and the power-law exponent were observed, revealing that the work-to-pull-off increases with the power-law exponent at lower unloading rates but decreases at higher unloading rates. Overall, the results demonstrate that the PA-ML framework serves as a valuable intermediary between analytical and numerical methods, addressing limitations in generalization, computational cost, and numerical instability. While analytical models like XPB provide theoretical consistency and numerical methods like BEM offer precision, the PA-ML approach combines the strengths of both to offer interpretable and computationally efficient predictions. The presented framework lays the foundation for further advancements in data-driven approaches to model visco-adhesive contact problems.

The chapter also introduced a data-driven framework for predicting the time-resolved evolution of adhesive forces. Using the same BEM methodology, a comprehensive trajectory dataset of 8505 samples was generated spanning a wide range of material properties, unloading rates, and geometric parameters. To overcome the challenges of unknown pull-off times and extreme temporal resolution, we proposed a segmented trajectory estimation model that predicts a fixed number of physically meaningful key points along the unloading curve rather than every time step. The resulting FNN provides a compact yet informative representation of the unloading process and demonstrates strong performance in capturing non-linear viscoelastic behavior.

Chapter 6

Summary, Conclusions and Future Perspectives

This concluding chapter consolidates the thesis by relating the main analytical, numerical, experimental, and data-driven results back to the original research objectives. It synthesizes the principal contributions, clarifies the validity range and limitations of the proposed framework, and identifies the most relevant directions for future work.

This thesis addressed the prediction of adhesive detachment in soft viscoelastic interfaces, where interfacial adhesion, bulk viscoelastic dissipation, loading history, and geometry are strongly coupled. The scientific question was twofold: how to identify the governing mechanics of rate-dependent detachment, and how to construct predictive tools that remain consistent with those mechanics while reducing computational cost by several orders of magnitude. Four objectives were pursued: (i) to clarify detachment mechanisms analytically through crack-propagation arguments and a four-parameter modified power-law constitutive model; (ii) to resolve adhesive viscoelastic contact numerically through a Boundary Element Method (BEM) framework with Lennard-Jones traction and Boltzmann hereditary integrals; (iii) to quantify the influence of geometry, preload, unloading rate, Tabor parameter, and material spectrum across both flat-punch and Hertzian configurations; and (iv) to develop physics-augmented machine-learning surrogates (Random Forest, XGBoost, feed-forward neural network) that preserve mechanical structure while achieving millisecond-level inference. The objectives were met within the scope of smooth rigid indenters in contact with soft substrates in the linear viscoelastic regime.

6.1 Closure of the Thesis Objectives

Objective 1 (Analytical mechanisms): For flat-punch detachment from finite viscoelastic layers, the analysis established three thickness-dependent regimes (cohesive, intermediate, and half-plane) and showed that geometric confinement bounds the maximum achievable adhesion enhancement to $\widehat{\Delta\gamma}_{\text{eff}}|_{\max} = (\pi/4)(b/a_0)$. For Hertzian contact, the modified power-law constitutive model provided a compact four-parameter broad-band representation with closed-form relaxation, creep, and frequency-response expressions, and its coupling with Persson-Brener fracture mechanics yielded the crack-speed–unloading-rate relation $\widehat{v} = 2.887\,\widehat{r}_{PB}^{\,1.171}$ and reduced expressions linking unloading rate to effective surface energy.

Objective 2 (High-fidelity simulation): The BEM framework resolved adhesive viscoelastic contact with nonlinear traction-separation behavior and viscoelastic constitutive response. For flat-punch contact, the simulations confirmed that pull-off increases with unloading rate up to a cohesive plateau and that loading history has only minor influence (within $\sim$2% variability). For Hertzian contact, the simulations clarified the coupled roles of unloading rate, preload, Tabor parameter, viscoelastic contrast, and spectral broadness, and identified threshold contact conditions required to avoid finite-size limitations.

Objective 3 (Parameter-effect quantification): By combining analytical and nu-

merical results, the thesis determined when semi-infinite predictions remain valid and when geometry imposes strict limits on adhesion amplification. In the Hertzian configuration, the threshold pull-off force was found to scale as $\widehat{P}_{po} = 0.3\,\widehat{a}_{0t}^{2.7}$, and the maximum theoretical amplification associated with the modulus ratio $1/k$ was shown to be often unattainable in practice because of preload and kinematic constraints. Comparison with experiments on PDMS ($R = 5.19\,\mathrm{mm}$, $\Delta\gamma_0 = 0.152\,\mathrm{J/m^2}$, $\mu = 2.05$) confirmed good agreement up to $\sim$100 µm/s.

Objective 4 (Physics-consistent fast prediction): For scalar quantities (pull-off force, effective surface energy, work to pull-off), the physics-augmented Random Forest reduced the mean squared prediction error by 60.3% relative to the best purely data-driven model (XGBoost) and achieved $R^2 \approx 0.9995$, while also improving extrapolation to unseen material exponents. For trajectory-level prediction, a feed-forward neural network (100-100-100 architecture) using six key points on the unloading curve provided compact descriptions of the full adhesive-force evolution. In both cases, inference time was reduced from $\sim 10^3$ s per BEM case to below 5 ms.

6.2 Original Contributions and Main Findings

6.2.1 Cross-cutting synthesis

A unifying result across the thesis is that finite-size effects impose hard limits on adhesion amplification in both contact geometries. In the flat-punch configuration, the layer thickness bounds the pull-off enhancement below the semi-infinite prediction. In the Hertzian configuration, insufficient preload prevents the contact from reaching the threshold size needed for full amplification. In both cases, linear viscoelastic theory describes the mechanics accurately within a well-defined validity window, and beyond that window (most clearly at high unloading rates in the PDMS experiments) additional nonlinear dissipation in the fracture process zone is required.

6.2.2 Contribution 1 (Mechanical): Finite-size effects in viscoelastic adhesion

The results in this thesis demonstrate that geometric confinement is not a secondary correction but a central mechanism governing the attainable pull-off response in viscoelastic detachment. For flat-punch contact, a finite-size extension of Greenwood-type crack-propagation arguments was developed, yielding the upper bound $\widehat{\Delta\gamma}_{\mathrm{eff}}|_{\max} = (\pi/4)(b/a_0)$ and a clear interpretation of the cohesive–intermediate–half-plane regime transitions. For Hertzian contact, the threshold contact radius

below which the maximum amplification is suppressed was quantified, with pull-off scaling as $\widehat{P}_{po} = 0.3\,\widehat{a}_{0t}^{2.7}$.

6.2.3 Contribution 2 (Constitutive and analytical): Modified power-law framework

The thesis introduces the coupling of a four-parameter modified power-law constitutive model with Persson-Brener crack-propagation theory for adhesive contact. This combination is new: while the power-law model and the Persson-Brener framework existed separately, the thesis provides their analytical integration, yielding the scaling relation $\widehat{v} = 2.887\,\widehat{r}_{PB}^{1.171}$ fitted across eight orders of magnitude of unloading rate. The process-zone parameter was determined as $\alpha \approx \pi/9 \approx 0.349$ (independent of k), and the corresponding process-zone length was estimated at $l_0 \approx 30\,\text{nm}$ from low-speed PDMS data.

6.2.4 Contribution 3 (Numerical): BEM exploration and experimental validation

The BEM framework developed in the thesis is, to the author's knowledge, a novel numerical model to resolve adhesive viscoelastic contact with Lennard-Jones traction, and broad-band viscoelasticity response over only five input parameters of viscoelasticity. Across the full parameter space, the simulations established that semi-infinite predictions are recovered only above threshold geometric conditions and that linear viscoelastic theory agrees with PDMS adhesion experiments (borosilicate glass sphere, $R = 5.19\,\text{mm}$) up to $\sim$100 µm/s, beyond which measured pull-off forces exceed linear predictions. At the highest tested rates, the nonlinear fracture-process-zone contribution to effective surface energy was found to be comparable to the bulk linear-viscoelastic contribution.

6.2.5 Contribution 4 (Methodological): Physics-augmented machine learning

The thesis demonstrates, for the first time, that physics-augmented supervised learning through embedding an analytical crack-propagation prediction as an additional input feature, can substantially improve accuracy, interpretability, and extrapolation in viscoelastic adhesion prediction. The physics-augmented Random Forest reduced the mean squared error by 60.3% relative to the best purely data-driven model, and the approach naturally maintained analytical limiting behavior where the embedded descriptor is valid. The extension from scalar prediction to trajectory-level

prediction via a six-key-point feed-forward neural network represents a further novel step, moving from endpoint prediction to compact time-resolved representation of detachment.

6.2.6 Answer to the central scientific question

Taken together, these results answer the central question of the thesis: predictive models of viscoelastic adhesive contact can learn from high-fidelity data guided with mechanics, provided that the analytical and numerical structure of the problem is preserved before being transferred to the learning stage.

6.3 Positioning Within the Broader Field

Within adhesive contact mechanics, the dissertation positions itself between two traditional extremes: analytical models that are physically interpretable but valid only under restrictive assumptions (single relaxation time, semi-infinite geometry, JKR or DMT limit), and high-fidelity numerical simulations that are broadly applicable but computationally expensive ($\sim 10^3$ s per case in the present BEM). Neither extreme alone is adequate for rapid exploration or design over broad parameter ranges.

The work also differs from the increasingly common use of purely data-driven surrogates in mechanics. In contrast to methods that treat the simulation as an opaque data source, the thesis embeds an explicit crack-propagation prediction (the extended Persson-Brener model) as a learned feature, thereby constraining the surrogate to respect known analytical structure. The key advantage of the present approach is that it does not require differentiable physics: the analytical descriptor is computed offline and supplied as an input, which makes it applicable to non-differentiable or legacy simulation codes without modification.

Finally, by extending the framework from scalar output prediction to reduced trajectory prediction, the thesis addresses a gap that most surrogate-modeling studies in contact mechanics have not yet reached. The results are surrogate serving as the fast front-end for design or control applications.

6.4 Limitations, Validity Range, and Critical Reflection

6.4.1 Physical-model limitations

The constitutive description is restricted to linear viscoelasticity. This assumption is adequate over a substantial range of unloading conditions, but the comparison with PDMS experiments indicates that it becomes insufficient when very fast detachment ($r > 100\,\mu m/s$ for the system investigated) activates additional nonlinear dissipation mechanisms in the fracture process zone. The contact problems treated in the thesis are smooth single-asperity configurations involving rigid indenters and normal loading only; roughness, multiasperity interactions, tangential loading, and compliant counter-bodies are outside the present scope. The adhesive interaction was modeled through a Lennard-Jones 3-9 traction law, which is appropriate as a tractable short-range model but cannot represent all possible interfacial chemistries or damage processes.

6.4.2 Data-driven-model limitations

The machine-learning models are trained on a dataset of 8,505 BEM simulations that, while broad in parameter coverage, represents a finite sampling of a five-dimensional input space. No built-in uncertainty quantification is provided: the models return point predictions without confidence bounds, and their reliability outside the training distribution cannot be guaranteed. The feed-forward neural network architecture (100-100-100) was selected by cross-validated hyperparameter search, but alternative architectures or training strategies were not exhaustively explored.

6.4.3 Scope of experimental validation

All experimental comparisons were conducted against a single material system (PDMS 10:1 cross-linked silicone) with a single sphere geometry ($R = 5.19\,mm$) and a single preload ($P_0 = 1.5\,mN$). While the agreement with published data from independent groups supports the physical consistency of the framework, the generalization to other soft materials, geometries, or interfacial chemistries remains to be confirmed experimentally.

6.5 Future Perspectives

Several extensions follow directly from the results of the dissertation, listed in approximate order of priority.

Rough and multiasperity interfaces. The computational advantage of physics-guided surrogates becomes even more important when direct simulations are prohibitively expensive, as is the case for rough or multiasperity contact. Extending the present BEM and surrogate framework to rough surfaces is a natural first step.

Nonlinear constitutive effects and process-zone calibration. The comparison with PDMS experiments already indicates that nonlinear dissipation is required to describe very fast detachment, where linear viscoelasticity alone underestimates measured adhesion enhancement. Combining the current framework with constitutive models capable of capturing large-strain effects, additional dissipative processes, and rate-dependent fracture behavior is a direct continuation of the present work.

Uncertainty quantification. The surrogate models developed in this thesis provide point predictions only. Embedding uncertainty estimates, for example through ensemble methods, conformal prediction, or Bayesian extensions, would allow the user to identify predictions that fall outside the region of reliable inference and to propagate uncertainty to downstream design decisions.

Direct integration of experimental data. The machine-learning models were trained on numerical databases and assessed against experiments indirectly through the underlying mechanics. Including experimental data directly in the learning process, either through transfer learning or multi-fidelity modeling, would improve robustness in regimes where numerical or analytical models lose accuracy.

Real-time design and control. The trajectory-level predictors suggest a concrete route toward real-time prediction and control of soft adhesive interfaces. Once coupled with experimental calibration and broader contact models, the mechanics-guided hierarchy could support online parameter identification and control-oriented optimization in applications such as soft gripping, reversible handling, and adaptive adhesive systems.

6.6 Final Remarks

The main outcome of this dissertation is the establishment of a predictive hierarchy for soft viscoelastic adhesive contact in which analytical models supply physical interpretation, high-fidelity BEM simulations supply quantitative reference data, and physics-augmented machine learning supplies computational efficiency. At the

mechanical level, the thesis clarifies how finite thickness, broad-band viscoelasticity, unloading rate, and contact conditions govern detachment, and identifies the boundaries beyond which classical semi-infinite or linear assumptions fail. At the methodological level, it demonstrates that first-principles modeling and data-driven prediction can be integrated without sacrificing physical consistency, provided that analytical structure is preserved through the modeling chain. The principles underlying this hierarchy, which embed what is known analytically, calibrate what must be resolved numerically, and learn the residual from data, are not specific to adhesion and may be applicable to other problems in computational mechanics where interpretability, fidelity, and speed must be achieved jointly.

Bibliography

[1] G. Giordano, R. B. N. Scharff, M. Carlotti, M. Gagliardi, C. Filippeschi, A. Mondini, A. Papangelo, and B. Mazzolai. Mechanochromic suction cups for local stress detection in soft robotics. *Advanced Intelligent Systems*, 6(12): 2400254, 2024. doi: 10.1002/aisy.202400254.

[2] J. Shintake, V. Cacucciolo, D. Floreano, and H. Shea. Soft robotic grippers. *Advanced Materials*, 30(29):1707035, 2018. doi: 10.1002/adma.201707035.

[3] S. Li, H. Tian, X. Zhu, Y. Fan, B. Nie, C. Wang, Z. He, X. Li, and J. Shao. Gecko-inspired self-sensing adhesive for intelligent adhesion. *Chemical Engineering Journal*, 523:168354, 2025. doi: 10.1016/j.cej.2025.168354.

[4] M. Kamperman, E. Kroner, A. del Campo, R. M. McMeeking, and E. Arzt. Functional adhesive surfaces with "gecko" effect: The concept of contact splitting. *Advanced Engineering Materials*, 12(5):335–348, 2010. doi: 10.1002/adem.201000104.

[5] E. Arzt, H. Quan, R. M. McMeeking, and R. Hensel. Functional surface microstructures inspired by nature—from adhesion and wetting principles to sustainable new devices. *Progress in Materials Science*, 120:100823, 2021. doi: 10.1016/j.pmatsci.2021.100823.

[6] H. Hertz. Ueber die berührung fester elastischer körper. *Journal für die reine und angewandte Mathematik*, 92:156–171, 1882. doi: 10.1515/crll.1882.92.156.

[7] K. L. Johnson. *Contact Mechanics*. Cambridge University Press, Cambridge, 1985.

[8] M. Ciavarella, J. Joe, A. Papangelo, and J. R. Barber. The role of adhesion in contact mechanics. *Journal of the Royal Society Interface*, 16(151):20180738, 2019. doi: 10.1098/rsif.2018.0738.

[9] D. Maugis. Adhesion of spheres: the JKR-DMT transition using a dugdale model. *Journal of Colloid and Interface Science*, 150(1):243–269, 1992. doi: 10.1016/0021-9797(92)90285-T.

[10] V. M. Muller, V. S. Yushchenko, and B. V. Derjaguin. On the influence of molecular forces on the deformation of an elastic sphere and its sticking to a rigid plane. *Journal of Colloid and Interface Science*, 77(1):91–101, 1980. doi: 10.1016/0021-9797(80)90419-1.

[11] R. M. Christensen. *Theory of Viscoelasticity: An Introduction*. Academic Press, Amsterdam, 2012.

[12] J. A. Greenwood. The theory of viscoelastic crack propagation and healing. *Journal of Physics D: Applied Physics*, 37(18):2557–2570, 2004. doi: 10.1088/0022-3727/37/18/011.

[13] B. N. J. Persson and E. A. Brener. Crack propagation in viscoelastic solids. *Physical Review E*, 71(3):036123, 2005. doi: 10.1103/PhysRevE.71.036123.

[14] B. N. J. Persson. Crack propagation in finite-sized viscoelastic solids with application to adhesion. *EPL (Europhysics Letters)*, 119(1):18002, 2017. doi: 10.1209/0295-5075/119/18002.

[15] B. N. J. Persson. A simple model for viscoelastic crack propagation. *European Physical Journal E*, 44(3):3, 2021. doi: 10.1140/epje/s10189-020-00001-w.

[16] L. Afferrante and G. Violano. On the effective surface energy in viscoelastic Hertzian contacts. *Journal of the Mechanics and Physics of Solids*, 158:104669, 2022. doi: 10.1016/j.jmps.2021.104669.

[17] G. Violano and L. Afferrante. Size effects in adhesive contacts of viscoelastic media. *European Journal of Mechanics - A/Solids*, 96:104665, 2022. doi: 10.1016/j.euromechsol.2022.104665.

[18] A. Maghami, M. Tricarico, M. Ciavarella, and A. Papangelo. Viscoelastic amplification of the pull-off stress in the detachment of a rigid flat punch from an adhesive soft viscoelastic layer. *Engineering Fracture Mechanics*, 298:109898, 2024. doi: 10.1016/j.engfracmech.2024.109898.

[19] A. Maghami, Q. Wang, M. Tricarico, M. Ciavarella, Q. Li, and A. Papangelo. Bulk and fracture process zone contribution to the rate-dependent adhesion amplification in viscoelastic broad-band materials. *Journal of the Mechanics and Physics of Solids*, 193:105844, 2024. doi: 10.1016/j.jmps.2024.105844.

[20] A. Tiwari, L. Dorogin, A. I. Bennett, K. D. Schulze, W. G. Sawyer, M. Tahir, G. Heinrich, and B. N. J. Persson. The effect of surface roughness and

viscoelasticity on rubber adhesion. *Soft Matter*, 13(19):3602–3621, 2017. doi: 10.1039/C7SM00177K.

[21] K. R. VanDonselaar, D. A. Bellido-Aguilar, M. Safaripour, H. Kim, J. J. Watkins, A. J. Crosby, D. C. Webster, and A. B. Croll. Silicone elastomers and the Persson–Brener adhesion model. *Journal of Chemical Physics*, 159 (18):184708, 2023. doi: 10.1063/5.0172415.

[22] K. L. Johnson, K. Kendall, and A. D. Roberts. Surface energy and the contact of elastic solids. *Proceedings of the Royal Society of London. A. Mathematical and Physical Sciences*, 324(1558):301–313, 1971. doi: 10.1098/rspa.1971.0141.

[23] B. V. Derjaguin, V. M. Muller, and Y. P. Toporov. Effect of contact deformations on the adhesion of particles. *Journal of Colloid and Interface Science*, 53 (2):314–326, 1975. doi: 10.1016/0021-9797(75)90018-1.

[24] Antonio Papangelo and Michele Ciavarella. A numerical study on roughness-induced adhesion enhancement in a sphere with an axisymmetric sinusoidal waviness using lennard–jones interaction law. *Lubricants*, 8(9):90, 2020. doi: 10.3390/lubricants8090090.

[25] Antonio Papangelo and Michele Ciavarella. Detachment of a rigid flat punch from a viscoelastic material. *Tribology letters*, 71(2):48, 2023. doi: 10.1007/s11249-023-01720-9.

[26] Q. Wang, A. Papangelo, M. Ciavarella, H. Gao, and Q. Li. Rapid detachment of a rigid sphere adhered to a viscoelastic substrate: An upper bound model incorporating Maugis parameter and preload effects. *Journal of the Mechanics and Physics of Solids*, 196:106028, 2025. doi: 10.1016/j.jmps.2025.106028.

[27] A. Papangelo and M. Ciavarella. A Maugis–Dugdale cohesive solution for adhesion of a surface with a dimple. *Journal of the Royal Society Interface*, 14 (127):20160996, 2017. doi: 10.1098/rsif.2016.0996.

[28] C. Linghu, Y. Liu, Y. Y. Tan, J. H. M. Sing, Y. Tang, A. Zhou, X. Wang, D. Li, H. Gao, and K. J. Hsia. Overcoming the adhesion paradox and switchability conflict on rough surfaces with shape-memory polymers. *Proceedings of the National Academy of Sciences of the United States of America*, 120(13): e2221049120, 2023. doi: 10.1073/pnas.2221049120.

[29] C. Linghu, Y. Liu, X. Yang, D. Li, Y. Y. Tan, H. B. M. H. Mohamed, F. B. R. Mohammad, Z. Du, J. Su, Y. Li, et al. Fibrillar adhesives with unprecedented

adhesion strength, switchability and scalability. *National Science Review*, 11 (10):nwae106, 2024. doi: 10.1093/nsr/nwae106.

[30] L. Felicetti, E. Chatelet, A. Latour, P.-H. Cornuault, and F. Massi. Tactile rendering of textures by an electro-active polymer piezoelectric device: mimicking friction-induced vibrations. *Biotribology*, 31:100211, 2022. doi: 10.1016/j.biotri.2022.100211.

[31] F. Forsbach, M. Heß, and A. Papangelo. A two-scale FEM-BAM approach for fingerpad friction under electroadhesion. *Frontiers in Mechanical Engineering*, 8:1074393, 2023. doi: 10.3389/fmech.2022.1074393.

[32] B. Mazzolai, A. Mondini, F. Tramacere, G. Riccomi, A. Sadeghi, G. Giordano, E. Del Dottore, M. Scaccia, M. Zampato, and S. Carminati. Octopus-inspired soft arm with suction cups for enhanced grasping tasks in confined environments. *Advanced Intelligent Systems*, 1(6):1900041, 2019. doi: 10.1002/aisy.201900041.

[33] F. Agnelli, M. Tricarico, and A. Constantinescu. Shape-shifting panel from 3D-printed undulated ribbon lattice. *Extreme Mechanics Letters*, 42:101089, 2021. doi: 10.1016/j.eml.2020.101089.

[34] A. A. Griffith. The phenomena of rupture and flow in solids. *Philosophical Transactions of the Royal Society of London. Series A, Containing Papers of a Mathematical or Physical Character*, 221(582–593):163–198, 1921.

[35] D. Maugis and M. Barquins. Fracture mechanics and the adherence of viscoelastic bodies. *Journal of Physics D: Applied Physics*, 11(14):1989–2023, 1978. doi: 10.1088/0022-3727/11/14/011.

[36] R. S. Bradley. The cohesive force between solid surfaces and the surface energy of solids. *The London, Edinburgh, and Dublin Philosophical Magazine and Journal of Science*, 13(86):853–861, 1932. doi: 10.1080/14786449209461990.

[37] D. Tabor. Surface forces and surface interactions. *Journal of Colloid and Interface Science*, 58(1):2–13, 1977. doi: 10.1016/0021-9797(77)90366-6.

[38] Francisco Pérez-Ràfols and Michele Ciavarella. On the effect of the height distribution function in adhesion of non-gaussian random rough surfaces, and a simple analytical model (BAM). *Tribology International*, 193:109441, 2024. doi: 10.1016/j.triboint.2024.109441.

[39] Francesc Pérez-Ràfols, Jan Steven Van Dokkum, and Lucia Nicola. On the interplay between roughness and viscoelasticity in adhesive hysteresis. *Journal of the Mechanics and Physics of Solids*, 170:105079, 2023. doi: 10.1016/j.jmps.2022.105079.

[40] P. R. Guduru. Detachment of a rigid solid from an elastic wavy surface: Theory. *Journal of the Mechanics and Physics of Solids*, 55(3):445–472, 2007. doi: 10.1016/j.jmps.2006.09.004.

[41] H. Gao, X. Wang, H. Yao, S. Gorb, and E. Arzt. Mechanics of hierarchical adhesion structures of geckos. *Mechanics of Materials*, 37(2–3):275–285, 2005. doi: 10.1016/j.mechmat.2004.03.008.

[42] H. Kesari and A. J. Lew. Effective macroscopic adhesive contact behavior induced by small surface roughness. *Journal of the Mechanics and Physics of Solids*, 59(12):2488–2510, 2011. doi: 10.1016/j.jmps.2011.07.009.

[43] L. Shui, L. Jia, H. Li, J. Guo, Z. Guo, Y. Liu, and X. Chen. Rapid and continuous regulating adhesion strength by mechanical micro-vibration. *Nature Communications*, 11(1):1583, 2020. doi: 10.1038/s41467-020-15447-x.

[44] M. Tricarico, M. Ciavarella, and A. Papangelo. Enhancement of adhesion strength through microvibrations: Modeling and experiments. *Journal of the Mechanics and Physics of Solids*, 196:106020, 2025. doi: 10.1016/j.jmps.2024.106020.

[45] I. Argatov, A. Papangelo, and M. Ciavarella. An asymptotic model of vibroadhesion. *International Journal of Non-Linear Mechanics*, 174:105089, 2025. doi: 10.1016/j.ijnonlinmec.2025.105089.

[46] M. Ciavarella, M. Tricarico, and A. Papangelo. On the dynamic JKR adhesion problem. *Mechanics of Materials*, 202:105252, 2025. doi: 10.1016/j.mechmat.2025.105252.

[47] J. Yi, W. Haouas, M. Gauthier, and K. Rabenorosoa. A PDMS/silicon adhesion control method at millimeter-scale based on microvibration. *Advanced Intelligent Systems*, 7(2):2400394, 2025. doi: 10.1002/aisy.202400394.

[48] A. R. Savkoor and G. A. D. Briggs. The effect of tangential force on the contact of elastic solids in adhesion. *Proceedings of the Royal Society of London. A. Mathematical and Physical Sciences*, 356(1684):103–114, 1977. doi: 10.1098/rspa.1977.0123.

[49] J. F. Waters and P. R. Guduru. Mode-mixity-dependent adhesive contact of a sphere on a plane surface. *Proceedings of the Royal Society A: Mathematical, Physical and Engineering Sciences*, 466(2117):1303–1325, 2010. doi: 10.1098/rspa.2009.0461.

[50] K. L. Johnson. Continuum mechanics modeling of adhesion and friction. *Langmuir*, 12(19):4510–4513, 1996. doi: 10.1021/la950889a.

[51] R. Sahli, G. Pallares, C. Ducottet, I. E. Ben Ali, S. Al Akhrass, M. Guibert, and J. Scheibert. Evolution of real contact area under shear and the value of static friction of soft materials. *Proceedings of the National Academy of Sciences of the United States of America*, 115(3):471–476, 2018. doi: 10.1073/pnas.1706434115.

[52] A. Papangelo and M. Ciavarella. On mixed-mode fracture mechanics models for contact area reduction under shear load in soft materials. *Journal of the Mechanics and Physics of Solids*, 124:159–171, 2019. doi: 10.1016/j.jmps.2018.10.011.

[53] B. N. J. Persson and M. Scaraggi. Theory of adhesion: role of surface roughness. *Journal of Chemical Physics*, 141(12):124701, 2014. doi: 10.1063/1.4895789.

[54] L. Pastewka and M. O. Robbins. Contact between rough surfaces and a criterion for macroscopic adhesion. *Proceedings of the National Academy of Sciences of the United States of America*, 111(9):3298–3303, 2014. doi: 10.1073/pnas.1320846111.

[55] G. Violano, A. Papangelo, and M. Ciavarella. Stickiness of randomly rough surfaces with high fractal dimension: is there a fractal limit? *Tribology International*, 159:106971, 2021. doi: 10.1016/j.triboint.2021.106971.

[56] J. Joe, M. Scaraggi, and J. R. Barber. Effect of fine-scale roughness on the tractions between contacting bodies. *Tribology International*, 111:52–56, 2017. doi: 10.1016/j.triboint.2017.03.001.

[57] M. Santeramo, G. Carbone, S. Krenn, and C. Putignano. A novel energy-based numerical approach for adhesive contact mechanics of rough surfaces. *Journal of the Mechanics and Physics of Solids*, 203:106217, 2025. doi: 10.1016/j.jmps.2025.106217.

[58] M. H. Müser. A dimensionless measure for adhesion and effects of the range of adhesion in contacts of nominally flat surfaces. *Tribology International*, 100:41–47, 2016. doi: 10.1016/j.triboint.2015.11.010.

[59] G. R. Irwin. Analysis of stresses and strains near the end of a crack traversing a plate. *Journal of Applied Mechanics*, 24(3):361–364, 1957. doi: 10.1115/1.4011547.

[60] K. L. Johnson. The adhesion of two elastic bodies with slightly wavy surfaces. *International Journal of Solids and Structures*, 32(3–4):423–430, 1995. doi: 10.1016/0020-7683(94)00111-9.

[61] R. M. McMeeking, L. Ma, and E. Arzt. Bi-stable adhesion of a surface with a dimple. *Advanced Engineering Materials*, 12(5):389–397, 2010. doi: 10.1002/adem.201000091.

[62] I. Argatov, Q. Li, R. Pohrt, and V. L. Popov. Johnson–Kendall–Roberts adhesive contact for a toroidal indenter. *Proceedings of the Royal Society A: Mathematical, Physical and Engineering Sciences*, 472(2191):20160218, 2016. doi: 10.1098/rspa.2016.0218.

[63] H. Gao and H. Yao. Shape insensitive optimal adhesion of nanoscale fibrillar structures. *Proceedings of the National Academy of Sciences of the United States of America*, 101(21):7851–7856, 2004. doi: 10.1073/pnas.0400757101.

[64] A. Papangelo. Adhesion between a power-law indenter and a thin layer coated on a rigid substrate. *Facta Universitatis, Series: Mechanical Engineering*, 16 (1):19–28, 2018. doi: 10.22190/FUME180102008P.

[65] V. L. Popov, R. Pohrt, and Q. Li. Strength of adhesive contacts: Influence of contact geometry and material gradients. *Friction*, 5(3):308–325, 2017. doi: 10.1007/s40544-017-0177-3.

[66] M. Ciavarella. An approximate JKR solution for a general contact, including rough contacts. *Journal of the Mechanics and Physics of Solids*, 114:209–218, 2018. doi: 10.1016/j.jmps.2018.03.005.

[67] J. R. Barber. *Contact Mechanics*. Springer, Cham, 2018.

[68] J. Q. Feng. Contact behavior of spherical elastic particles: a computational study of particle adhesion and deformations. *Colloids and Surfaces A: Physicochemical and Engineering Aspects*, 172(1–3):175–198, 2000. doi: 10.1016/S0927-7757(00)00580-X.

[69] J. A. Greenwood. Adhesion of elastic spheres. *Proceedings of the Royal Society of London. Series A: Mathematical, Physical and Engineering Sciences*, 453 (1961):1277–1297, 1997. doi: 10.1098/rspa.1997.0070.

[70] K. L. Johnson and J. A. Greenwood. An adhesion map for the contact of elastic spheres. *Journal of Colloid and Interface Science*, 192(2):326–333, 1997. doi: 10.1006/jcis.1997.4984.

[71] D. Maugis. Adherence and fracture mechanics. In L. H. Lee, editor, *Adhesive Bonding*, pages 303–335. Springer, Boston, MA, 1991. doi: 10.1007/978-1-4757-9006-1_11.

[72] M. L. Williams. Structural analysis of viscoelastic materials. *AIAA Journal*, 2 (5):785–808, 1964. doi: 10.2514/3.2447.

[73] R. A. Schapery. A theory of crack initiation and growth in viscoelastic media. I. theoretical development. *International Journal of Fracture*, 11(1):141–159, 1975. doi: 10.1007/BF00034721.

[74] R. A. Schapery. A theory of crack initiation and growth in viscoelastic media. II. approximate methods of analysis. *International Journal of Fracture*, 11(3): 369–388, 1975. doi: 10.1007/BF00033526.

[75] J. A. Greenwood and K. L. Johnson. The mechanics of adhesion of viscoelastic solids. *Philosophical Magazine A*, 43(3):697–711, 1981. doi: 10.1080/01418618108240402.

[76] R. A. Schapery. A theory of viscoelastic crack growth: revisited. *International Journal of Fracture*, 233(1):1–16, 2022. doi: 10.1007/s10704-021-00605-z.

[77] G. Carbone, C. Mandriota, and N. Menga. Theory of viscoelastic adhesion and friction. *Extreme Mechanics Letters*, 56:101877, 2022. doi: 10.1016/j.eml.2022.101877.

[78] C. Mandriota, N. Menga, and G. Carbone. Adhesive contact mechanics of viscoelastic materials. *International Journal of Solids and Structures*, 290: 112685, 2024. doi: 10.1016/j.ijsolstr.2024.112685.

[79] G. A. C. Graham. Two extending crack problems in linear viscoelasticity theory. *Quarterly of Applied Mathematics*, 27(4):497–507, 1970.

[80] W. G. Knauss. On the steady propagation of a crack in a viscoelastic sheet: Experiments and analysis. In H. H. Kausch, J. A. Hassell, and R. I. Jaffee, editors, *Deformation and Fracture of High Polymers*, pages 501–541. Springer, Boston, MA, 1973. doi: 10.1007/978-1-4757-1263-6_27.

[81] A. Maghami, M. Stender, and A. Papangelo. Pull-off force prediction in viscoelastic adhesive hertzian contact by physics augmented machine learning. *International Journal of Solids and Structures*, 322:113584, 2025. doi: 10.1016/j.ijsolstr.2025.113584.

[82] M. Ciavarella, G. Cricrì, and R. M. McMeeking. A comparison of crack propagation theories in viscoelastic materials. *Theoretical and Applied Fracture Mechanics*, 116:103113, 2021. doi: 10.1016/j.tafmec.2021.103113.

[83] A. N. Gent and J. Schultz. Effect of wetting liquids on the strength of adhesion of viscoelastic materials. *Journal of Adhesion*, 3(4):281–294, 1972.

[84] M. L. Williams, R. F. Landel, and J. D. Ferry. The temperature dependence of relaxation mechanisms in amorphous polymers and other glass-forming liquids. *Journal of the American Chemical Society*, 77(14):3701–3707, 1955. doi: 10.1021/ja01619a008.

[85] A. N. Gent and R. P. Petrich. Adhesion of viscoelastic materials to rigid substrates. *Proceedings of the Royal Society of London. A. Mathematical and Physical Sciences*, 310(1502):433–448, 1969. doi: 10.1098/rspa.1969.0085.

[86] M. Barquins and D. Maugis. Tackiness of elastomers. *Journal of Adhesion*, 13 (1):53–65, 1981. doi: 10.1080/00218468108073174.

[87] A. N. Gent. Adhesion and strength of viscoelastic solids. is there a relationship between adhesion and bulk properties? *Langmuir*, 12(19):4492–4496, 1996. doi: 10.1021/la950887q.

[88] C. Creton and M. Ciccotti. Fracture and adhesion of soft materials: a review. *Reports on Progress in Physics*, 79(4):046601, 2016. doi: 10.1088/0034-4885/79/4/046601.

[89] M. S. Ahmad-Abad, A. Maghami, M. Ghalishooyan, and A. Shooshtari. A family of minimum residual displacement methods as nonlinear solution schemes for equilibrium path-following in structural mechanics. *Computers & Structures*, 300:107407, 2024. doi: 10.1016/j.compstruc.2024.107407.

[90] F. V. Souza and D. H. Allen. Multiscale modeling of impact on heterogeneous viscoelastic solids containing evolving microcracks. *International Journal for Numerical Methods in Engineering*, 82(4):464–504, 2010. doi: 10.1002/nme.2773.

[91] K. Guo, Z. Yang, C.-H. Yu, and M. J. Buehler. Artificial intelligence and machine learning in design of mechanical materials. *Materials Horizons*, 8(4): 1153–1172, 2021. doi: 10.1039/D0MH01451F.

[92] I. Goodfellow, Y. Bengio, and A. Courville. *Deep Learning*. MIT Press, Cambridge, MA, 2016. `http://www.deeplearningbook.org`.

[93] C. T. Mackay and D. Nowell. Informed machine learning methods for application in engineering: A review. *Proceedings of the Institution of Mechanical Engineers, Part C: Journal of Mechanical Engineering Science*, 237(24):5801–5818, 2023. doi: 10.1177/09544062231164575.

[94] J. Zhu, Y. Xue, and Z. Liu. A transfer learning enhanced physics-informed neural network for parameter identification in soft materials. *Applied Mathematics and Mechanics (English Edition)*, 45(10):1685–1704, 2024. doi: 10.1007/s10483-024-3178-9.

[95] K. Eshkofti and S. M. Hosseini. The modified physics-informed neural network (PINN) method for the thermoelastic wave propagation analysis based on the Moore–Gibson–Thompson theory in porous materials. *Composite Structures*, 348:118485, 2024. doi: 10.1016/j.compstruct.2024.118485.

[96] Svenja Ehlers, Norbert Hoffmann, Tianning Tang, Adrian H. Callaghan, Rui Cao, Enrique M. Padilla, Yuxin Fang, and Merten Stender. Physics-informed neural networks for phase-resolved data assimilation and prediction of nonlinear ocean waves. *Physical Review Fluids*, 10(9):094901, 2025. doi: 10.1103/ytyy-pvys.

[97] Y.-T. Wang, X. Zhang, and X.-S. Liu. Machine learning approaches to rock fracture mechanics problems: Mode-I fracture toughness determination. *Engineering Fracture Mechanics*, 253:107890, 2021. doi: 10.1016/j.engfracmech.2021.107890.

[98] X. Li, X. Zhang, W. Feng, and Q. Wang. Machine learning-based prediction of fracture toughness and path in the presence of micro-defects. *Engineering Fracture Mechanics*, 276:108900, 2022. doi: 10.1016/j.engfracmech.2022.108900.

[99] R. Perera and V. Agrawal. A generalized machine learning framework for brittle crack problems using transfer learning and graph neural networks. *Mechanics of Materials*, 181:104639, 2023. doi: 10.1016/j.mechmat.2023.104639.

[100] C. E. Athanasiou, X. Liu, B. Zhang, T. Cai, C. Ramirez, N. P. Padture, J. Lou, B. W. Sheldon, and H. Gao. Integrated simulation, machine learning, and experimental approach to characterizing fracture instability in indentation pillar-splitting of materials. *Journal of the Mechanics and Physics of Solids*, 170:105092, 2023. doi: 10.1016/j.jmps.2022.105092.

[101] R. Yi, D. Georgiou, X. Liu, and C. E. Athanasiou. Mechanics-informed, model-free symbolic regression framework for solving fracture problems. *Journal of the Mechanics and Physics of Solids*, 194:105916, 2025. doi: 10.1016/j.jmps.2024.105916.

[102] K. Kalliorinne, R. Larsson, F. Pérez-Ràfols, M. Liwicki, and A. Almqvist. Artificial neural network architecture for prediction of contact mechanical response. *Frontiers in Mechanical Engineering*, 6:579825, 2021. doi: 10.3389/fmech.2020.579825.

[103] C. Goodbrake, S. Motiwale, and M. S. Sacks. A neural network finite element method for contact mechanics. *Computer Methods in Applied Mechanics and Engineering*, 419:116671, 2024. doi: 10.1016/j.cma.2023.116671.

[104] S. Motiwale, W. Zhang, R. Feldmeier, and M. S. Sacks. A neural network finite element approach for high speed cardiac mechanics simulations. *Computer Methods in Applied Mechanics and Engineering*, 427:117060, 2024. doi: 10.1016/j.cma.2024.117060.

[105] T. Sahin, M. von Danwitz, and A. Popp. Solving forward and inverse problems of contact mechanics using physics-informed neural networks. *Advanced Modeling and Simulation in Engineering Sciences*, 11(1):11, 2024. doi: 10.1186/s40323-024-00265-3.

[106] T. Sahin, D. Wolff, and A. Popp. Physics-informed neural networks for solving contact problems in three dimensions. In *Advances and Challenges in Computational Mechanics*, pages 419–431. Springer, 2026. doi: 10.1007/978-3-031-93213-7_33.

[107] M. Stender, M. Tiedemann, D. Spieler, D. Schoepflin, N. Hoffmann, and S. Oberst. Deep learning for brake squeal: Brake noise detection, characterization and prediction. *Mechanical Systems and Signal Processing*, 149:107181, 2021. doi: 10.1016/j.ymssp.2020.107181.

[108] C. Geier, S. Hamdi, T. Chancelier, P. Dufrénoy, N. Hoffmann, and M. Stender. Machine learning-based state maps for complex dynamical systems: applications to friction-excited brake system vibrations. *Nonlinear Dynamics*, 111(24): 22137–22151, 2023. doi: 10.1007/s11071-023-08739-6.

[109] B. Sattari Baboukani, Z. Ye, K. G. Reyes, and P. C. Nalam. Prediction of nanoscale friction for two-dimensional materials using a machine learning approach. *Tribology Letters*, 68(2):57, 2020. doi: 10.1007/s11249-020-01294-w.

[110] T. Sahin, J. Bonari, S. Brandstaeter, and A. Popp. Data-driven surrogate modeling techniques to predict the effective contact area of rough surface contact problems. *arXiv preprint arXiv:2504.17354*, 2025.

[111] M. Didonna, M. Stender, A. Papangelo, F. Fontanela, M. Ciavarella, and N. Hoffmann. Reconstruction of governing equations from vibration measurements for geometrically nonlinear systems. *Lubricants*, 7(8):64, 2019. doi: 10.3390/lubricants7080064.

[112] S. Javadi, A. Maghami, and S. M. Hosseini. A deep learning approach based on a data-driven tool for classification and prediction of thermoelastic wave's band structures for phononic crystals. *Mechanics of Advanced Materials and Structures*, 29(27):6612–6625, 2022. doi: 10.1080/15376494.2021.1983088.

[113] L. Kellner, M. Stender, H. Herrnring, S. Ehlers, N. Hoffmann, K. V. Høyland, et al. Establishing a common database of ice experiments and using machine learning to understand and predict ice behavior. *Cold Regions Science and Technology*, 162:56–73, 2019. doi: 10.1016/j.coldregions.2019.03.007.

[114] Y. Kim, C. Yang, Y. Kim, G. X. Gu, and S. Ryu. Designing an adhesive pillar shape with deep learning-based optimization. *ACS Applied Materials & Interfaces*, 12(21):24458–24465, 2020. doi: 10.1021/acsami.0c04123.

[115] D. Son, V. Liimatainen, and M. Sitti. Machine learning-based and experimentally validated optimal adhesive fibril designs. *Small*, 17(39):2102867, 2021. doi: 10.1002/smll.202102867.

[116] A. Luo, H. Zhang, and K. T. Turner. Machine learning-based optimization of the design of composite pillars for dry adhesives. *Extreme Mechanics Letters*, 54:101695, 2022. doi: 10.1016/j.eml.2022.101695.

[117] Y. Kim, J. Yeo, K. Park, A. Destrée, Z. Qin, and S. Ryu. Designing directional adhesive pillars using deep learning-based optimization, 3D printing, and testing. *Mechanics of Materials*, 185:104778, 2023. doi: 10.1016/j.mechmat.2023.104778.

[118] C. B. Dayan, D. Son, A. Aghakhani, Y. Wu, S. O. Demir, and M. Sitti. Machine learning-based shear optimal adhesive microstructures with experimental validation. *Small*, 20(2):2304437, 2024. doi: 10.1002/smll.202304437.

[119] M. Shojaeifard, M. Ferraresso, A. Lucantonio, and M. Bacca. Machine learning-based optimal design of fibrillar adhesives. *Journal of the Royal Society Interface*, 22(223):20240636, 2025. doi: 10.1098/rsif.2024.0636.

[120] J. Yu and S. Ryu. Deep reinforcement learning-based optimization for the shape of an adhesive pillar with enhanced adhesion strength. *Journal of Mechanical Design*, 147(9):091703, 2025. doi: 10.1115/1.4068747.

[121] Bahador Bahrami, Saba Abbaszadeh, Hossein Talebi, Majid R. Ayatollahi, and Mohammad Reza Khosravani. Machine learning prediction of failure load in composite and metallic single-lap adhesive joints. *International Journal of Adhesion and Adhesives*, page 104265, 2026. doi: 10.1016/j.ijadhadh.2026.104265.

[122] A. Papangelo and M. Ciavarella. Detachment of a rigid flat punch from a viscoelastic material. *Tribology Letters*, 71(2):48, 2023. doi: 10.1007/s11249-023-01720-9.

[123] L. Afferrante, G. Violano, and G. Carbone. Exploring the dynamics of viscoelastic adhesion in rough line contacts. *Scientific Reports*, 13(1):15060, 2023. doi: 10.1038/s41598-023-39932-7.

[124] F. Forsbach. A simple semi-analytical method for solving axisymmetric contact problems involving bonded and unbonded layers of arbitrary thickness. *Machines*, 11(4):474, 2023. doi: 10.3390/machines11040474.

[125] B. Peng, X.-Q. Feng, and Q. Li. Decohesion of a rigid flat punch from an elastic layer of finite thickness. *Journal of the Mechanics and Physics of Solids*, 139:103937, 2020. doi: 10.1016/j.jmps.2020.103937.

[126] K. L. Johnson. *Contact Mechanics*. Cambridge University Press, Cambridge, 1985.

[127] J. R. Barber. *Contact Mechanics*. Springer International Publishing, Cham, 2018.

[128] D. Maugis. *Contact, Adhesion and Rupture of Elastic Solids*, volume 130 of *Solid-State Sciences*. Springer, Berlin, 2000.

[129] A. Jagota, S. J. Bennison, and C. A. Smith. Viscoelastic fracture of soft adhesives. *International Journal of Fracture*, 104(2):105–130, 2000.

[130] T. Tang, A. Jagota, M. K. Chaudhury, and C. Y. Hui. Thermal fluctuations limit the adhesive strength of compliant solids. *Journal of Adhesion*, 82(7): 671–696, 2006. doi: 10.1080/00218460600775781.

[131] A. Bonfanti, J. L. Kaplan, G. Charras, and A. Kabla. Fractional viscoelastic models for power-law materials. *Soft Matter*, 16(26):6002–6020, 2020. doi: 10.1039/D0SM00354A.

[132] A. Papangelo and M. Ciavarella. A numerical study on roughness-induced adhesion enhancement in a sphere with an axisymmetric sinusoidal waviness using Lennard-Jones interaction law. *Lubricants*, 8(9):90, 2020. doi: 10.3390/lubricants8090090.

[133] R. H. Bentall and K. L. Johnson. An elastic strip in plane rolling contact. *International Journal of Mechanical Sciences*, 10(8):637–663, 1968. doi: 10.1016/0020-7403(68)90070-2.

[134] R. M. Christensen. *Theory of Viscoelasticity: An Introduction*. Academic Press, Amsterdam, 2012.

[135] L. Afferrante and G. Violano. On the effective surface energy in viscoelastic Hertzian contacts. *Journal of the Mechanics and Physics of Solids*, 158:104669, 2022. doi: 10.1016/j.jmps.2021.104669.

[136] G. Violano and L. Afferrante. On the long and short-range adhesive interactions in viscoelastic contacts. *Tribology Letters*, 70(3):68, 2022. doi: 10.1007/s11249-022-01611-5.

[137] M. Ciavarella, A. Papangelo, and R. McMeeking. Crack propagation at the interface between viscoelastic and elastic materials. *Engineering Fracture Mechanics*, 257:108009, 2021. doi: 10.1016/j.engfracmech.2021.108009.

[138] J. A. Greenwood and K. L. Johnson. The mechanics of adhesion of viscoelastic solids. *Philosophical Magazine A*, 43(3):697–711, 1981.

[139] R. A. Schapery. A theory of crack initiation and growth in viscoelastic media. I. theoretical development. *International Journal of Fracture*, 11(1):141–159, 1975. doi: 10.1007/BF00034721.

[140] R. A. Schapery. A theory of crack initiation and growth in viscoelastic media. II. approximate methods of analysis. *International Journal of Fracture*, 11(3): 369–388, 1975. doi: 10.1007/BF00033526.

[141] R. A. Schapery. A theory of viscoelastic crack growth: revisited. *International Journal of Fracture*, 233(1):1–16, 2022. doi: 10.1007/s10704-021-00605-z.

[142] B. N. J. Persson and E. A. Brener. Crack propagation in viscoelastic solids. *Physical Review E*, 71(3):036123, 2005. doi: 10.1103/PhysRevE.71.036123.

[143] B. N. J. Persson. Crack propagation in finite-sized viscoelastic solids with application to adhesion. *EPL (Europhysics Letters)*, 119(1):18002, 2017. doi: 10.1209/0295-5075/119/18002.

[144] B. N. J. Persson. A simple model for viscoelastic crack propagation. *European Physical Journal E*, 44(3):1, 2021. doi: 10.1140/epje/s10189-020-00001-w.

[145] W. W. Chen, Q. J. Wang, Z. Huan, and X. Luo. Semi-analytical viscoelastic contact modeling of polymer-based materials. *Journal of Tribology*, 133(4): 041404, 2011. doi: 10.1115/1.4004928.

[146] S. Lin, C. D. Londono, D. Zheng, and X. Zhao. An extreme toughening mechanism for soft materials. *Soft Matter*, 18(31):5742–5749, 2022. doi: 10.1039/D2SM00609J.

[147] A. R. Dusane, P. Lenarda, and M. Paggi. Computational modeling of viscoelastic backsheet materials for photovoltaics. *Mechanics of Materials*, 186:104810, 2023. doi: 10.1016/j.mechmat.2023.104810.

[148] Y. Qi, X. Li, S. P. Venkata, X. Yang, T. L. Sun, C.-Y. Hui, J. P. Gong, and R. Long. Mapping deformation and dissipation during fracture of soft viscoelastic solid. *Journal of the Mechanics and Physics of Solids*, 186:105595, 2024. doi: 10.1016/j.jmps.2024.105595.

[149] G. Huang, B. Wang, and H. Lu. Measurements of viscoelastic functions of polymers in the frequency-domain using nanoindentation. *Mechanics of Time-Dependent Materials*, 8(4):345–364, 2004. doi: 10.1007/s11043-004-0440-7.

[150] Y. M. Efremov, W.-H. Wang, S. D. Hardy, R. L. Geahlen, and A. Raman. Measuring nanoscale viscoelastic parameters of cells directly from AFM force-displacement curves. *Scientific Reports*, 7(1):1541, 2017. doi: 10.1038/s41598-017-01784-3.

[151] K. D. Saharuddin, M. H. M. Ariff, I. Bahiuddin, S. A. Mazlan, S. A. A. Aziz, N. Nazmi, A. Y. A. Fatah, and K. Mohmad. Constitutive models for predicting field-dependent viscoelastic behavior of magnetorheological elastomer using machine learning. *Smart Materials and Structures*, 29(8):087001, 2020. doi: 10.1088/1361-665X/ab972d.

[152] A. S. Hosseini, P. Hajikarimi, M. Gandomi, F. M. Nejad, and A. H. Gandomi. Optimized machine learning approaches for the prediction of viscoelastic behavior of modified asphalt binders. *Construction and Building Materials*, 299: 124264, 2021. doi: 10.1016/j.conbuildmat.2021.124264.

[153] G. Violano, A. Chateauminois, and L. Afferrante. A JKR-like solution for viscoelastic adhesive contacts. *Frontiers in Mechanical Engineering*, 7:664486, 2021. doi: 10.3389/fmech.2021.664486.

[154] G. Violano, G. Orlando, G. P. Demelio, and L. Afferrante. Adhesion of viscoelastic media: an assessment of a recent JKR-like solution. In *IOP Conference Series: Materials Science and Engineering*, volume 1214, page 012038, 2022. doi: 10.1088/1757-899X/1214/1/012038.

[155] M. H. Müser and B. N. J. Persson. Crack and pull-off dynamics of adhesive, viscoelastic solids. *EPL (Europhysics Letters)*, 137(3):36004, 2022. doi: 10.1209/0295-5075/ac535c.

[156] B. Lorenz, B. A. Krick, N. Mulakaluri, M. Smolyakova, S. Dieluweit, W. G. Sawyer, and B. N. J. Persson. Adhesion: role of bulk viscoelasticity and surface roughness. *Journal of Physics: Condensed Matter*, 25(22):225004, 2013. doi: 10.1088/0953-8984/25/22/225004.

[157] V. L. Popov. *Contact Mechanics and Friction*. Springer, Berlin, Heidelberg, 2010. doi: 10.1007/978-3-642-10803-7.

[158] A. Bonfanti, J. L. Kaplan, G. Charras, and A. Kabla. Fractional viscoelastic models for power-law materials. *Soft Matter*, 16(26):6002–6020, 2020. doi: 10.1039/D0SM00354A.

[159] R. Sahli, G. Pallares, A. Papangelo, M. Ciavarella, C. Ducottet, N. Ponthus, and J. Scheibert. Shear-induced anisotropy in rough elastomer contact. *Physical Review Letters*, 122(21):214301, 2019. doi: 10.1103/PhysRevLett.122.214301.

[160] C. Oliver, D. Dalmas, and J. Scheibert. Adhesion in soft contacts is minimum beyond a critical shear displacement. *Journal of the Mechanics and Physics of Solids*, 181:105445, 2023. doi: 10.1016/j.jmps.2023.105445.

[161] K. L. Johnson. *Contact Mechanics*. Cambridge University Press, Cambridge, 1985.

[162] A. Petroli, M. Petroli, M. Romagnoli, and M. Geoghegan. Determination of the rate-dependent adhesion of polydimethylsiloxane using an atomic force microscope. *Polymer*, 262:125445, 2022. doi: 10.1016/j.polymer.2022.125445.

[163] T. Pritz. Unbounded complex modulus of viscoelastic materials and the Kramers–Kronig relations. *Journal of Sound and Vibration*, 279(3–5):687–697, 2005.

[164] R. W. Carpick, D. F. Ogletree, and M. Salmeron. A general equation for fitting contact area and friction vs. load measurements. *Journal of Colloid and Interface Science*, 211(2):395–400, 1999. doi: 10.1006/jcis.1998.6027.

[165] P.-G. de Gennes. Soft adhesives. *Langmuir*, 12(19):4497–4500, 1996. doi: 10.1021/la950886y.

[166] F. Saulnier, T. Ondarçuhu, A. Aradian, and E. Raphaël. Adhesion between a viscoelastic material and a solid surface. *Macromolecules*, 37(3):1067–1075, 2004. doi: 10.1021/ma021759t.

[167] W. G. Knauss. A review of fracture in viscoelastic materials. *International Journal of Fracture*, 196(1):99–146, 2015. doi: 10.1007/s10704-015-0058-6.

[168] C.-Y. Hui, B. Zhu, and R. Long. Steady state crack growth in viscoelastic solids: A comparative study. *Journal of the Mechanics and Physics of Solids*, 159:104748, 2022. doi: 10.1016/j.jmps.2021.104748.

[169] A. N. Gent and S.-M. Lai. Interfacial bonding, energy dissipation, and adhesion. *Journal of Polymer Science Part B: Polymer Physics*, 32(8):1543–1555, 1994. doi: 10.1002/polb.1994.090320826.

[170] G. J. Lake and A. G. Thomas. The strength of highly elastic materials. *Proceedings of the Royal Society of London. Series A. Mathematical and Physical Sciences*, 300(1460):108–119, 1967. doi: 10.1098/rspa.1967.0160.

[171] S.-Q. Wang, Z. Fan, C. Gupta, A. Siavoshani, and T. Smith. Fracture behavior of polymers in plastic and elastomeric states. *Macromolecules*, 57(9):3875–3900, 2024. doi: 10.1021/acs.macromol.3c01952.

[172] R. A. Schapery. Correspondence principles and a generalized J integral for large deformation and fracture analysis of viscoelastic media. *International Journal of Fracture*, 25(3):195–223, 1984. doi: 10.1007/BF01140837.

[173] R. A. Schapery. Stable and unstable viscoelastic crack growth: experimental validation of nonlinear theory for rubber. *International Journal of Fracture*, 238(1):1–15, 2022. doi: 10.1007/s10704-022-00639-x.

[174] E. Barthel. The linear viscoelastic fracture theory applies to soft solids better when they are... viscoelastic. *Proceedings of the Royal Society A: Mathematical, Physical and Engineering Sciences*, 480(2288):20230561, 2024. doi: 10.1098/rspa.2023.0561.

[175] O. Akogwu, D. Kwabi, S. Midturi, M. Eleruja, B. Babatope, and W. O. Soboyejo. Large strain deformation and cracking of nano-scale gold films on PDMS substrate. *Materials Science and Engineering: B*, 170(1–3):32–40, 2010. doi: 10.1016/j.mseb.2010.02.023.

[176] Z. P. Bažant and Y.-N. Li. Cohesive crack with rate-dependent opening and viscoelasticity: I. mathematical model and scaling. *International Journal of Fracture*, 86:247–265, 1997. doi: 10.1023/A:1007486221395.

[177] S. R. Lavoie, R. Long, and T. Tang. Rate dependent fracture of a double cantilever beam with combined bulk and interfacial dissipation. *International Journal of Solids and Structures*, 75–76:277–286, 2015. doi: 10.1016/j.ijsolstr.2015.08.020.

[178] M. Musto and G. Alfano. A novel rate-dependent cohesive-zone model combining damage and visco-elasticity. *Computers & Structures*, 118:126–133, 2013. doi: 10.1016/j.compstruc.2012.12.020.

[179] G. Zhao, J. Xu, Y. Feng, J. Tang, Y. Chen, S. Xin, X. Jian, S. Li, S. Zhang, and J. Xu. A rate-dependent cohesive zone model with the effects of interfacial

viscoelasticity and progressive damage. *Engineering Fracture Mechanics*, 248: 107695, 2021. doi: 10.1016/j.engfracmech.2021.107695.

[180] R. A. Schapery. Crack growth in viscoelastic media with large strains: further results and validation of nonlinear theory for rubber. *International Journal of Fracture*, 241(2):121–139, 2023. doi: 10.1007/s10704-023-00696-w.

[181] M. Ciavarella. Improved muller approximate solution of the pull-off of a sphere from a viscoelastic substrate. *Journal of Adhesion Science and Technology*, 35 (20):2175–2183, 2021. doi: 10.1080/01694243.2021.1882766.

[182] M. Ciavarella. An upper bound for viscoelastic pull-off of a sphere with a Maugis-Dugdale model. *Journal of Adhesion*, 98(13):2118–2131, 2022. doi: 10.1080/00218464.2021.1954914.

[183] F. Scarselli and A. C. Tsoi. Universal approximation using feedforward neural networks: A survey of some existing methods, and some new results. *Neural Networks*, 11(1):15–37, 1998. doi: 10.1016/S0893-6080(97)00097-X.

[184] M. Ciavarella, G. Cricrì, and R. McMeeking. A comparison of crack propagation theories in viscoelastic materials. *Theoretical and Applied Fracture Mechanics*, 116:103113, 2021. doi: 10.1016/j.tafmec.2021.103113.

[185] C. Molnar. *Interpretable Machine Learning: A Guide for Making Black Box Models Explainable*. Online book, 3 edition, 2025. Retrieved from `https://christophm.github.io/interpretable-ml-book/`.

[186] T. Chen and C. Guestrin. XGBoost: A scalable tree boosting system. In *Proceedings of the 22nd ACM SIGKDD International Conference on Knowledge Discovery and Data Mining*, pages 785–794. ACM, 2016. doi: 10.1145/2939672.2939785.

[187] G. James, D. Witten, T. Hastie, and R. Tibshirani. *An Introduction to Statistical Learning: With Applications in R*, volume 103. Springer, 2013.

[188] T. Hastie, R. Tibshirani, and J. H. Friedman. *The Elements of Statistical Learning: Data Mining, Inference, and Prediction*. Springer, 2 edition, 2009.

Appendices

Appendix-I. Perfectly bonded layer

For the case of a layer perfectly bonded to the rigid substrate, following Johnson [126], we only need to correct the previous results for the Poisson effect with $\zeta = \frac{(1-\nu)^2}{1-2\nu}$ (this requires $\nu \lesssim 0.45$, [126]), so that we have

$$\delta_{po} = \sqrt{\frac{2b\Delta\gamma}{\zeta E^*}}, \qquad \overline{\sigma}_{po} = \sqrt{\frac{2\zeta E^* \Delta\gamma}{b}} \tag{1}$$

where $\overline{\sigma}_{po}$ equals the cohesive strength of the material for the layer thickness

$$b_0 = \frac{2\zeta E^* \Delta\gamma}{\sigma_0^2} = \frac{4}{\pi}\zeta a_0 \tag{2}$$

Appendix-II. More comparison with viscoelastic crack propagation theories

Using Persson and Brener theory [142] for a single relaxation time material gives an implicit equation for the effective adhesion energy [184]

$$\widehat{\Delta\gamma}_{eff}\left(\widehat{V}_c\right) = \left[1 - (1-k)\,\frac{\widehat{\Delta\gamma}_{eff}}{\beta\widehat{V}_c}\left(\sqrt{1+\left(\frac{\beta\widehat{V}_c}{\widehat{\Delta\gamma}_{eff}}\right)^2} - 1\right)\right]^{-1} \tag{3}$$

being $\beta = 64\Sigma_0/\left(9\sqrt{3}\right)$. Eq. (3) can be extended to finite size systems by accounting that for a very thin layer the maximum enhancement will be reduced to $\widehat{\Delta\gamma}_{eff}\Big|_{\max} = (\pi/4)\,(b/a_0)$, so we propose here a generalization of Eq. (3) in order to take into account finite size systems, i.e. for $b_0 < b < b_{0\infty}$

$$\widehat{\Delta\gamma}_{eff}\left(\widehat{V}_c, \frac{b}{a_0}\right) = \left[1 - \left(1 - \frac{4}{\pi\,(b/a_0)}\right)\frac{\widehat{\Delta\gamma}_{eff}}{\beta\widehat{V}_c}\left(\sqrt{1+\left(\frac{\beta\widehat{V}_c}{\widehat{\Delta\gamma}_{eff}}\right)^2} - 1\right)\right]^{-1} \tag{4}$$

where we have explicitly indicated that the normalized effective surface energy depends not only on the crack speed, but also on the ratio between the layer thickness and the fracture length a_0. A comparison between the numerical results and Eq. (4) is shown in Fig. A.1.

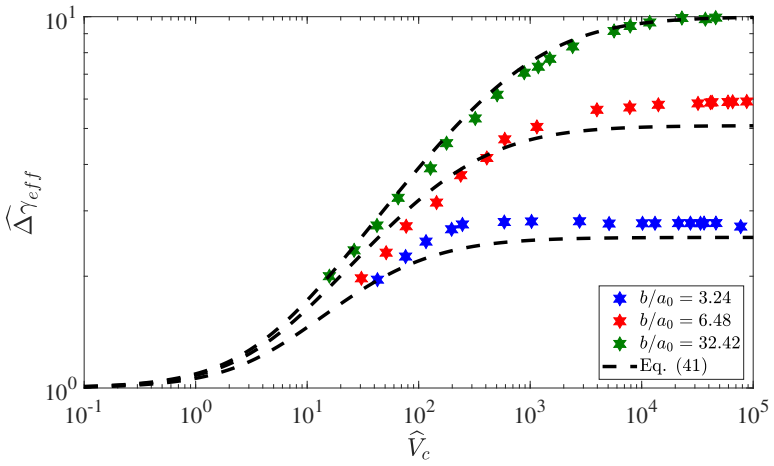

Figure A.1: Normalized effective surface energy as a function of the crack velocity at pull-off for four different values of b/a_0 for a punch with $\widehat{a}/\widehat{a}_0 = 64.85$ unloaded from a fully relaxed viscoelastic layer ($k = 0.1$). Dashed lines are obtained with Eq. (4).

Appendix-III. Modified power law material model

Relaxation function in time and frequency domain

Let us assume to model a viscoelastic material with a continuous distribution $H(\tau)$ of relaxation times, which is the so-called material relaxation spectrum, in parallel with a Hookean spring giving the material stiffness for a long time. This coincides with assuming a Wiechert model (see Fig. A.2) with an infinite number of Maxwell arms. The general relation for the stress $\sigma(t)$ at time t is (Eq. (2.34) in Williams [72])[1]:

$$\sigma(t) = \left\{ E_0 + \int_0^\infty \frac{H(\tau)}{\left[\frac{d}{dt} + 1/\tau\right]\tau} d\tau \frac{d}{dt} \right\} \varepsilon(t) \ , \tag{5}$$

Converting Eq. (5) in the frequency domain, we get:

$$\sigma(\omega) = \left\{ E_0 + \int_0^\infty \frac{H(\tau)\, \boldsymbol{i}\omega}{[\boldsymbol{i}\omega\tau + 1]} d\tau \right\} \varepsilon(\omega) = \overline{E}(\omega)\, \varepsilon(\omega) \ , \tag{6}$$

[1]Notice that we are using the notation according to Williams [72]. In Christensen [11] book the relaxation spectrum is defined as $[H(\tau)]_{Christensen} = [H(\tau)]_{Williams}/\tau$

where, $\boldsymbol{i}$ is the imaginary unit, ω is the angular frequency, and, by definition, $\overline{E}(\omega) = E'(\omega) + \boldsymbol{i}E''(\omega)$ is the complex modulus, hence:

$$\overline{E}(\omega) = E_0 + \int_0^\infty \frac{H(\tau)\,\boldsymbol{i}\omega}{[\boldsymbol{i}\omega\tau + 1]} d\tau \ . \tag{7}$$

In order to fit the experimental data, one can guess a certain form for the relaxation spectrum $H(\tau)$. As suggested by Williams [72], a broad-band approximation of the response of the viscoelastic material can be obtained by adopting for the relaxation spectrum a modified power law:

$$H(\tau) = \left(\frac{E_\infty - E_0}{\Gamma(n)}\right)\left(\frac{\tau_0}{\tau}\right)^n \exp\left(-\frac{\tau_0}{\tau}\right) \ , \tag{8}$$

The complex modulus is $\overline{E}(\omega) = E'(\omega) + \boldsymbol{i}E''(\omega)$ can be written in terms of the relaxation spectrum:

$$\overline{E}(\omega) = E_0 + \int_0^\infty \frac{H(\tau)\,\boldsymbol{i}\omega}{[\boldsymbol{i}\omega\tau + 1]} d\tau \ , \tag{9}$$

$$E'(\omega) = E_0 + \int_0^\infty \frac{H(\tau)\,\omega^2\tau}{[1 + \omega^2\tau^2]} d\tau \ , \tag{10}$$

$$E''(\omega) = \int_0^\infty \frac{H(\tau)\,\omega}{[1 + \omega^2\tau^2]} d\tau \ . \tag{11}$$

By using Eq. (.3) for the relaxation spectrum $H(\tau)$ one obtains

$$\overline{E}(\omega) = E_0 + (E_\infty - E_0)\,\boldsymbol{i}\omega\tau_0 \exp(\boldsymbol{i}\omega\tau_0)\,\mathbf{E}_n(\boldsymbol{i}\omega\tau_0) \ , \tag{12}$$

$$E'(\omega) = E_0 + \frac{(E_\infty - E_0)}{\Gamma(n)} \left\{ \begin{array}{c} \pi(\tau_0\omega)^n \cos\left(n\frac{\pi}{2} + \tau_0\omega\right)\csc(n\pi) + ... \\ ... + (\tau_0\omega)^2 \Gamma(n-2)\,{}_{\mathrm{p}}\mathrm{F}_{\mathrm{q}}\left[1; \left\{\frac{3-n}{2}, 2 - \frac{n}{2}\right\}; -\frac{(\tau_0\omega)^2}{4}\right] \end{array} \right\} \ , \tag{13}$$

$$E''(\omega) = \frac{(E_\infty - E_0)}{\Gamma(n)} \left\{ \begin{array}{c} \pi(\tau_0\omega)^n \sin\left(n\frac{\pi}{2} + \tau_0\omega\right)\csc(n\pi) + ... \\ ... + (\tau_0\omega)\,\Gamma(n-1)\,{}_{\mathrm{p}}\mathrm{F}_{\mathrm{q}}\left[1; \left\{1 - \frac{n}{2}, \frac{3-n}{2}\right\}; -\frac{(\tau_0\omega)^2}{4}\right] \end{array} \right\} \ , \tag{14}$$

where τ_0 is the characteristic time, $n > 0$ is a characteristic exponent, ω is the angular frequency, E_0 is the relaxed elastic modulus, E_∞ is the instantaneous elastic modulus, ${}_{\mathrm{p}}\mathrm{F}_{\mathrm{q}}[a; b; z]$ is the generalized hypergeometric function, $\Gamma(x)$ is the Euler gamma function.

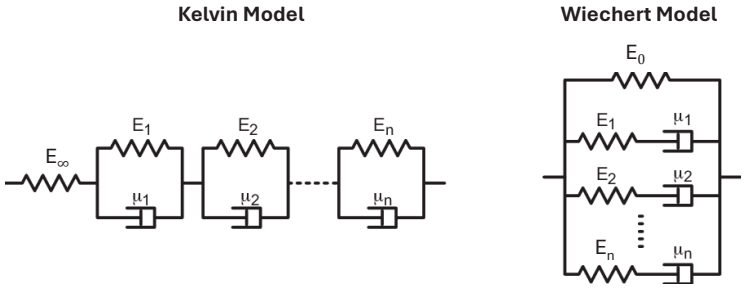

Figure A.2: The Kelvin model (left) and the Wiechert model (right) for the representation of the mechanical behaviour of a viscoelastic material.

Compliance function in time and frequency domain

Let us now consider to model a viscoelastic material with an infinite series of Voigt elements, in series with a Hookean spring giving the material stiffness for short time, the so-called Kelvin model (see Fig. A.2). This coincides with assuming a continuous distribution of retardation times $L(\tau)$, which is the so-called material retardation spectrum. A general relation for the deformation $\varepsilon(t)$ at time t is given by (Eq. (2.42) in Williams [72]):

$$\varepsilon(t) = \left\{ C_\infty + \int_0^\infty \frac{L(\tau)}{\left[\frac{d}{dt} + 1/\tau\right]\tau^2} d\tau \right\} \sigma(t) \ , \tag{15}$$

where $C_\infty = 1/E_\infty$ is the creep compliance in the glassy limit. Converting Eq. (.3) in the frequency domain gives:

$$\varepsilon(\omega) = \left\{ C_\infty + \int_0^\infty \frac{L(\tau)}{[\boldsymbol{i}\omega + 1/\tau]\tau^2} d\tau \right\} \sigma(\omega) = \overline{C}(\omega)\sigma(\omega) \ , \tag{16}$$

where, $\boldsymbol{i}$ is the imaginary unit and, by definition, $\overline{C}(\omega) = C'(\omega) - \boldsymbol{i}C''(\omega)$ is the complex compliance. Hence, we have:

$$\overline{C}(\omega) = C_\infty + \int_0^\infty \frac{L(\tau)}{[\boldsymbol{i}\omega + 1/\tau]} \frac{d\tau}{\tau^2} \ . \tag{17}$$

We note that to match the experimental data, a specific form for the retardation spectrum $L(\tau)$ could be considered. Following Williams [72] suggestion, a broad-band approximation of the viscoelastic material response can be achieved by using a modified power law for the retardation spectrum, such as:

$$L(\tau) = \left(\frac{C_0 - C_\infty}{\Gamma(n)}\right) \left(\frac{\tau}{\tau_0}\right)^n \exp\left(-\frac{\tau}{\tau_0}\right) \ , \tag{18}$$

The complex compliance is defined as follows:

$$\overline{C}(\omega) = C'(\omega) - \boldsymbol{i}C''(\omega) \ , \tag{19}$$

where

$$\overline{C}(\omega) = C_\infty + \int_0^\infty \frac{L(\tau)}{[\boldsymbol{i}\omega + 1/\tau]} \frac{d\tau}{\tau^2} \ , \tag{20}$$

$$C'(\omega) = C_\infty + \int_0^\infty \frac{L(\tau)}{[1+\omega^2\tau^2]} \frac{d\tau}{\tau} \ , \tag{21}$$

$$C''(\omega) = \int_0^\infty \frac{L(\tau)\,\omega}{[1+\omega^2\tau^2]} d\tau \ . \tag{22}$$

By using Eq. (.3) for the retardation spectrum $L(\tau)$ one obtains

$$\overline{C}(\omega) = C_\infty + \frac{(C_0 - C_\infty)}{\boldsymbol{i}\omega\tau_0} \exp\left(-\frac{\boldsymbol{i}}{\omega\tau_0}\right) \mathbf{E}_n\left(-\frac{\boldsymbol{i}}{\omega\tau_0}\right) \tag{23}$$

$$C'(\omega) = C_\infty + \frac{(C_0 - C_\infty)(\tau_0\omega)^{-2-n}}{\Gamma(n)} \left\{ \begin{array}{c} \pi(\tau_0\omega)^2 \cos\left(n\frac{\pi}{2} + \frac{1}{\tau_0\omega}\right) \csc(n\pi) + ... \\ ... + (\tau_0\omega)^n \Gamma(-2+n)_{\mathrm{p}}\mathrm{F}_{\mathrm{q}}\left[1; \left\{\frac{3-n}{2}, 2-\frac{n}{2}\right\}; -\frac{1}{4(\tau_0\omega)^2}\right] \end{array} \right\} \tag{24}$$

$$C''(\omega) = \frac{(C_0 - C_\infty)(\tau_0\omega)^{-1-n}}{\Gamma(n)} \left\{ \begin{array}{c} \pi\tau_0\omega \sin\left(n\frac{\pi}{2} + \frac{1}{\tau_0\omega}\right) \csc(n\pi) + ... \\ ... + (\tau_0\omega)^n \Gamma(-1+n)_{\mathrm{p}}\mathrm{F}_{\mathrm{q}}\left[1; \left\{1-\frac{n}{2}, \frac{3-n}{2}\right\}; -\frac{1}{4(\tau_0\omega)^2}\right] \end{array} \right\} \ , \tag{25}$$

where τ_0 is the characteristic time, $n > 0$ is a characteristic exponent, ω is the angular frequency, $C_0 = 1/E_0$ is the relaxed compliance, $C_\infty = 1/E_\infty$ is the instantaneous compliance, ${}_{\mathrm{p}}\mathrm{F}_{\mathrm{q}}[a; b; z]$ is the generalized hypergeometric function, $\Gamma(x)$ is the Euler gamma function.

Appendix-IV. Details of the PB model for the effective surface energy

According to PB theory the dimensionless effective surface energy for a MPL viscoelastic material model $\widehat{\Gamma}_{eff}$ is obtained as

$$\widehat{\Gamma}_{eff} = \left[1 - (1-k)\, I\left(n, \widehat{v}, \widehat{\Gamma}_{eff}\right)\right]^{-1} \ , \tag{26}$$

where $I(n,\widehat{v},\widehat{\Gamma}_{eff})$ stands for the integral in Eq. (4.20), which can be evaluated in closed form as:

$$I(n,\widehat{v},\widehat{\Gamma}_{\text{eff}}) = \frac{2^{(-3-2n)}\pi^{(-3/2-n)}}{(n-1)\widehat{v}}\left\{-4^{(1+n)}\pi^{(1/2+n)}\left[\widehat{\Gamma}_{\text{eff}}+\right.\right. \tag{27}$$

$$-2(n-1)\pi\widehat{v}\,{}_{\text{p}}\text{F}_{\text{q}}\left[-\frac{1}{2};\left\{\frac{1}{2}-\frac{n}{2},1-\frac{n}{2}\right\};-\left(\frac{\widehat{\Gamma}_{\text{eff}}}{4\pi\widehat{v}}\right)^2\right]\Bigg]+$$

$$+2\pi\left(\frac{\widehat{\Gamma}_{\text{eff}}}{\widehat{v}}\right)^n\left[4\pi\widehat{v}\Gamma\left[1-\frac{n}{2}\right]{}_{\text{p}}\text{F}_{\text{q}}|_{\text{Reg}}\left[\frac{n-1}{2};\left\{\frac{1}{2},\frac{2+n}{2}\right\};-\left(\frac{\widehat{\Gamma}_{\text{eff}}}{4\pi\widehat{v}}\right)^2\right]+\right.$$

$$\left.\left.+\widehat{\Gamma}_{\text{eff}}\Gamma\left[\frac{3}{2}-\frac{n}{2}\right]{}_{\text{p}}\text{F}_{\text{q}}|_{\text{Reg}}\left[\frac{n}{2};\left\{\frac{3}{2},\frac{(3+n)}{2}\right\};-\left(\frac{\widehat{\Gamma}_{\text{eff}}}{4\pi\widehat{v}}\right)^2\right]\right]\right\}, \tag{28}$$

where ${}_{\text{p}}\text{F}_{\text{q}}[a,b,z]$ is the generalized hypergeometric function, ${}_{\text{p}}\text{F}_{\text{q}}|_{\text{Reg}}[a,b,z]$ is the regularized generalized hypergeometric function and $\Gamma[x]$ is the gamma function (we used Wolfram Mathematica© for algebraic manipulation).

To ease the use of Eq. (4.21) we report here, in Fig. A.3, the quantity $\widehat{\Gamma}_{eff}-1$, showing that there exist two power law regimes. The first is a linear scaling where $(\widehat{\Gamma}_{eff}-1)\simeq q_1 V^1$, with the coefficient $q_1=-0.0125+3.136n$ depending on the material exponent "n". The second instead can be written as $(\widehat{\Gamma}_{eff}-1)\simeq q_2 V^{m_2}$, with the $\{q_2,m_2\}$ constants depending on n, which is shown in the inset of Fig. A.3. Notice that an SLS would have $n\approx 1.6$, which provides a scaling of $(\widehat{\Gamma}_{eff}-1)\propto V^{0.5}$, while broad-band materials provide a much lower exponent m_2, as one can see in Fig. A.3 (inset).

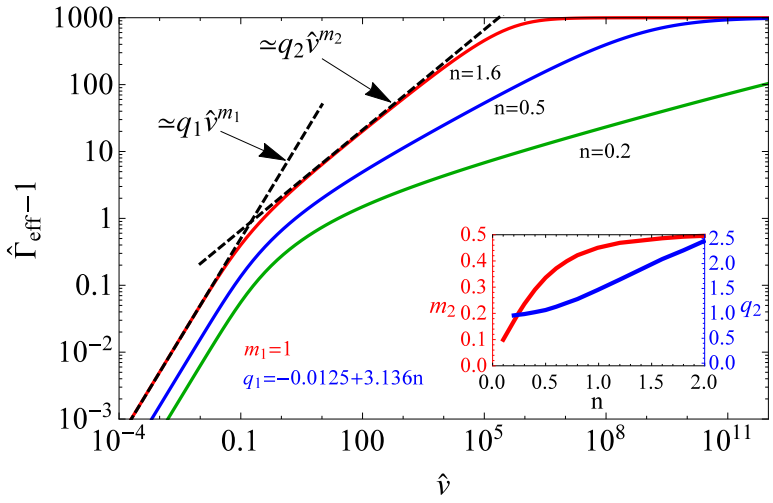

Figure A.3: Fit of the enhancement of the effective surface energy $\widehat{\Gamma}_{eff}-1$ obtained using a MPL material model in PB theory. Two power law scaling have been identified for $\widehat{v}<1$ and for $\widehat{v}>1$, which coefficients are given in the figure and in the inset as a function of the material exponent n.

Appendix-V. Details of the boundary element method implementation as a numerical model

Kernel function

$G(r,s)$ is the so-called Kernel function, defined as:

$$G(r,s) = \begin{cases} \frac{4}{\pi r}\overline{\mathrm{K}}\left(\frac{s}{r}\right), & s < r \\ \frac{4}{\pi s}\overline{\mathrm{K}}\left(\frac{r}{s}\right), & s > r \end{cases} \tag{29}$$

where $\overline{\mathrm{K}}$ denotes the complete elliptic integral of the first kind with modulus k.

In this work, the gap function is solved by applying the Boundary Element Method (BEM) combined with the Newton–Raphson method on $N = M + 1$ equally spaced nodes, where M represents the number of interfacial elements. Equation (4.15) is discretized in both time and space to compute the half-space deflections. A time-marching algorithm with a time step Δt is employed for the temporal discretization. For spatial discretization, the pressure distribution is assumed to have a triangular shape over each element. Specifically, for the j-th element, the pressure p_j is defined at $r = r_j$ and decreases linearly to zero at $r = r_{j-1}$ and $r = r_{j+1}$. This approach is commonly referred to as the *method of overlapping triangles* [24, 25, 161]. Once the number of nodes is fixed, the influence matrix $G_{i,j}$ can be computed so that the deflection $u_z[i]$ of the *elastic* halfspace at the node i can be found by linear superposition

$$u_z[i] = \frac{1}{E_0^*}\sum_{j=1}^{N} G_{i,j}\sigma_j. \tag{30}$$

For the problem of a Hertzian rigid indenter on a viscoelastic surface, one can define the following dimensionless parameters as: $\widehat{h} = (h - h_0)/h_0$, $\widehat{\delta} = \delta/h_0$, $\widehat{r} = r/\beta$, $\widehat{\sigma} = \sigma/(\frac{\Delta\gamma_0}{\mu h_0})$, and $t = \tau\widehat{t}$ where

$$\beta^3 = \frac{R^2\Delta\gamma_0}{E^*}, \quad \mu = \left(\frac{R\Delta\gamma_0^2}{E_0^{*2}h_0^3}\right)^{1/3}, \tag{31}$$

Equations (4.11), (4.12), and (4.15) are expressed in a discretized form in both space and time, where i denotes the spatial index and q represents the temporal index, as follows:

$$\widehat{\sigma}[i,q] = -\frac{8}{3}\mu\left[\frac{1}{(\widehat{h}[i,q]+1)^3} - \frac{1}{(\widehat{h}[i,q]+1)^9}\right], \tag{32}$$

$$\widehat{h}[i,q] = -\widehat{\delta}[q] + \frac{1}{2}\mu\widehat{r}[i]^2 + \widehat{u}_z[i,q] \ , \tag{33}$$

$$\widehat{u}_z[i,q] \approx \mu \sum \widehat{G}_{ij} \sum_{m=0}^{q} \widehat{C}[q-m] \left(\widehat{\sigma}[j,m+1] - \widehat{\sigma}[j,m]\right) \ , \tag{34}$$

where the dimensionless form of the creep compliance function $\widehat{C} = C/C_0$ in (4.9) is:

$$\widehat{C}(\widehat{t}) = 1 - 2\frac{(1-k)}{\Gamma(n)}\widehat{t}^{n/2}\mathrm{K}_n\left(2\sqrt{\widehat{t}}\right) \ . \tag{35}$$

Appendix-VI. Machine Learning Methods

Linear regression

Linear regression is one of the simplest and most widely used statistical methods for modeling the relationship between a dependent variable and one or more independent variables. It assumes a linear relationship between inputs and outputs. Linear regression is particularly effective when the relationship between variables is approximately linear, but it may struggle with non-linear relationships unless transformed appropriately [185].

Regression tree

A regression tree is similar to a decision tree that predicts continuous outputs by recursively partitioning the data space into regions with similar target values. Each split is chosen to minimize variance in the resulting subsets. Regression trees are interpretable but prone to overfitting and can be unstable with small data changes [185].

Random forest

Random Forest is a learning method that constructs multiple decision trees during training and outputs the mode or mean prediction of these trees for classification or regression tasks. This technique enhances predictive accuracy and controls overfitting by averaging out biases from individual trees. Each tree in the forest is built using a random subset of the data and features, which helps capture diverse patterns within the dataset. Random Forest is robust to noise and can handle large datasets

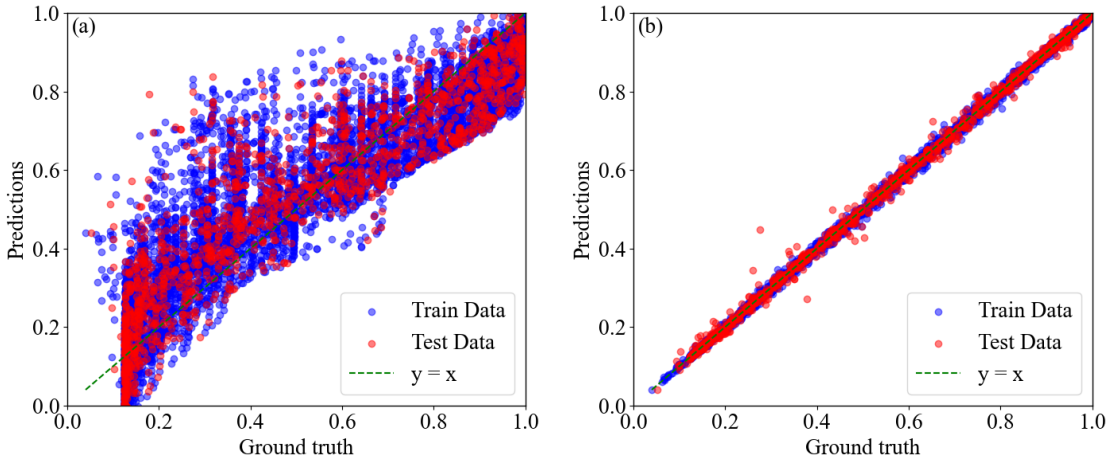

Figure A.4: ML model's performance: (a) The plot illustrates the performance of linear regression model; (b) The plot shows the results of the XGBoost model, which demonstrates stronger performance.

with high dimensionality effectively, making it a popular choice for many practical applications [185].

Extreme Gradient Boosting (XGBoost)

XGBoost is an advanced implementation of gradient boosting that has gained popularity due to its high performance in ML competitions. It builds models sequentially by adding new trees that correct errors made by previous ones, optimizing for both speed and accuracy through techniques like regularization and parallel processing [186]. XGBoost is particularly effective for tabular data because it can handle missing values internally and offers flexibility in model tuning.

Visual comparison of ground truth and predictions

Here, we present two figures that illustrate the performance of different modeling approaches. Figure A.4 focuses on pure data-driven ML model predictions, while Figure A.5 shows the performance of a physics-augmented model. Each figure has two subfigures: the first subfigure depicts the results of linear regression, and the second represents the results from the XGBoost algorithm.

Appendix-VII. Descriptive Statistics of the Dataset

This section provides the descriptive statistics for the dataset. Table A.1 summarizes key statistical measures, including central tendency (mean, median), variability

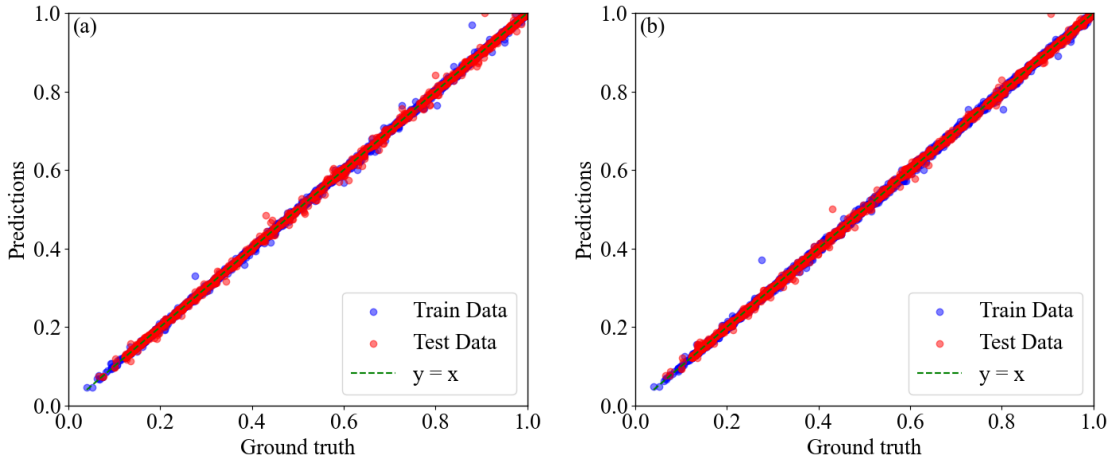

Figure A.5: PA-ML model's performance: (a) The plot shows the performance of Random Forest; (b) The plot illustrates the results of the XGBoost model.

(standard deviation), and extreme values (minimum, maximum) for each parameter.

The variables $\widehat{\delta}_l$, $\widehat{r}_u$, k, $\widehat{\Gamma}_{\text{eff}}$, and $\widehat{w}_{\text{po}}$ were $\log_{10}$-transformed before model training and testing. The minimum and maximum values indicate substantial heterogeneity within the dataset, particularly for $\widehat{r}_u$, which spans multiple orders of magnitude.

Table A.1: Descriptive statistics for the principal parameters in the data set.

Statistic	$\log_{10}(\widehat{\delta}_l)$	μ	$\log_{10}(\widehat{r}_u)$	$\log_{10}(k)$	n
Mean	0.5718	0.7181	4.467	-0.9189	0.8471
Median	0.684	0.3	4.4	-1	0.6
StdDev	0.9359	0.9501	2.75	0.219	0.5635
Min	-2.255	0.04	-1.5	-4	0.2
Max	2.738	3.24	10	-0.301	2

Appendix-VIII. Upper-bound approximation of Hertzian work to pull-off in the glassy Regime

At very high unloading rates, viscoelastic substrates behave as elastic solids characterized by their instantaneous (glassy) modulus. In this regime, adhesive detachment is dominated by elastic energy storage rather than viscoelastic dissipation. While the Hertzian geometry exhibits a continuously varying contact area, the stress distribution near detachment becomes increasingly concentrated toward the edge, resembling the uniform stress field under a flat punch. Therefore, we approximate the unloading behavior of an adhesive Hertzian contact at high rates using the flat punch formulation. In the limit of *very fast unloading*, a viscoelastic substrate responds elastically

with its *glassy modulus* E^*_∞. For a rigid axisymmetric flat punch of radius a detaching from such a substrate, the normal force during unloading is as follows:

$$P(\delta) = 2aE^*_\infty\delta\,. \tag{36}$$

The pull-off load is governed by linear elastic fracture mechanics and given by [25]:

$$P_{\mathrm{po}} = \sqrt{8\pi E^*_\infty \Delta\gamma_0 a^3}\,. \tag{37}$$

Substituting this into the force-displacement relation yields the displacement at pull-off:

$$\delta_{\mathrm{po}} = \frac{P_{\mathrm{po}}}{2aE^*_\infty} = \frac{\sqrt{8\pi E^*_\infty \Delta\gamma_0 a^3}}{2aE^*_\infty}\,. \tag{38}$$

The work required to pull-off the punch is defined as the area under the unloading curve:

$$w_{\mathrm{po}} = \int_0^{\delta_{\mathrm{po}}} 2aE^*_\infty\delta\,d\delta = aE^*_\infty\delta^2_{\mathrm{po}}\,, \tag{39}$$

Substituting for δ_{po} leads to the simplified expression:

$$w_{\mathrm{po}} = 2\pi a^2\Delta\gamma_0\,, \tag{40}$$

where it is the work to pull-off related to an axisymmetric flat punch, and for a Hertzian indenter, one can consider it with $a \approx a_{po}$. Considering the contact radius as $a = \widehat{a}(\pi R^2\Delta\gamma_0/E^*_0)^{1/3}$, one can obtain the following relation:

$$w_{\mathrm{po}} = 2\pi\widehat{a}^2_{\mathrm{po}}(\pi R^2\Delta\gamma_0/E^*_0)^{2/3}\Delta\gamma_0\,. \tag{41}$$

Normalizing by the characteristic energy scale $1.5\pi\Delta\gamma_0 Rh_0$, the dimensionless work becomes:

$$\widehat{w}_{\mathrm{po}} = \frac{w_{\mathrm{po}}}{1.5\pi\Delta\gamma_0 Rh_0} = \frac{4}{3}\widehat{a}^2_{\mathrm{po}}\pi^{2/3}\frac{R^{1/3}\Delta\gamma_0^{2/3}}{E_0^{2/3}h_0}, \tag{42}$$

Considering the Tabor parameter, we have the following upper bound approximation:

$$(\widehat{w}_{\mathrm{po}})_{\mathrm{up}} = \frac{4}{3}\widehat{a}^2_{\mathrm{po}}\pi^{2/3}\mu. \tag{43}$$

Figure A.6 compares the PA-ML predictions and analytically estimated upper-bound of glassy behavior for normalized work to pull-off from 43 across different Tabor parameters.

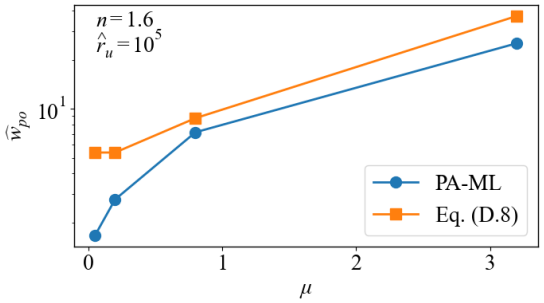

Figure A.6: Comparison between the predicted normalized work to pull-off ($\widehat{w}_{po}$) from the PA-ML model (XGBoost) and the upper bound of glassy behavior values obtained from equation (43), for different values of the Tabor parameter $\mu = [0.05, 0.2, 0.8, 3.2]$ (which correspond to $\widehat{a}_{\text{po}} = [6.1377, 3.0689, 1.9564, 2.0139]$). The predictions correspond to a fixed normalized indentation depth $\widehat{\delta}_l = 73.0$, material modulus ratio $k = 0.1$, and normalized unloading rate $\widehat{r}_u = 10^5$ and $n = 1.6$. Circular markers indicate PA-ML predictions, and square markers correspond to values from equation 43.

Appendix-IX. Lower-bound approximation of work to pull-off in JKR rubbery regime

The Johnson-Kendall-Roberts (JKR) [22] theory is an analytical model describing the mechanics of adhesive elastic contact. It extends Hertzian contact theory by considering surface energy, making it particularly applicable to soft materials and scenarios where adhesion plays a significant role. Here to have consistent relations with our numerical results as well as the ML solution, we consider $a = \widehat{a}(\pi R^2 \Delta\gamma_0 / E_0^*)^{1/3}$, and $P = \widehat{P}(1.5\pi\Delta\gamma_0 R h_0)$. Hence, the JKR solution for the dimensionless load and indentation are given by:

$$\widehat{P} = 2\widehat{a}^3 - 1.5\sqrt{8\widehat{a}^3}\,, \tag{44}$$

$$\frac{\widehat{\delta}}{\mu\pi^{2/3}} = \widehat{a}^2 - \sqrt{2\widehat{a}}\,. \tag{45}$$

The work to pull-off is $\widehat{w}_{\text{po}} = |\int_{\widehat{\delta}_{\text{on}}}^{\widehat{\delta}_{\text{po}}} \widehat{P}(\delta, t)\, d\widehat{\delta}| = \frac{w_{po}}{1.5\pi\Delta\gamma_0 R h_0}$, where $\widehat{\delta}_{\text{on}}$ is the displacement at which the normal force first becomes zero during unloading, and $\widehat{\delta}_{\text{po}}$ denotes the displacement at pull-off. Therefore, the work to pull-off is obtained as follows:

$$\widehat{w}_{\text{po}} = 0.80182\mu\pi^{2/3}\,. \tag{46}$$

As shown in Figure A.7, the PA-ML model results in the glassy and rubbery regimes are bounded by the rubbery lower limit derived from Eq. (46) and the glassy upper limit given by Eq. (43).

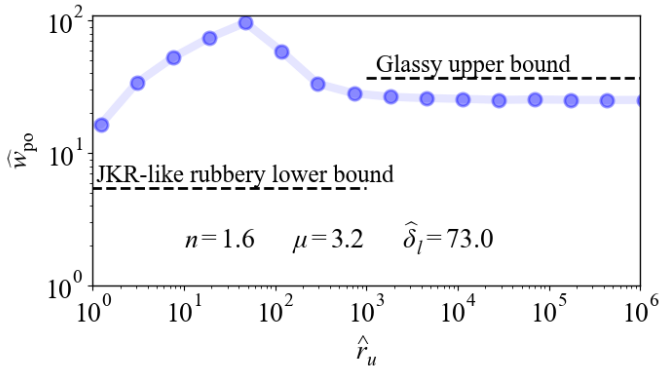

Figure A.7: PA-ML prediction of normalized work to pull-off ($\widehat{w}_{\mathrm{po}}$) as a function of the normalized unloading rate ($\widehat{r}_u$) for $\mu = 3.2$ and $n = 1.6$, at a fixed indentation depth $\widehat{\delta}_l = 73.0$ and modulus ratio $k = 0.1$. The blue curve represents the PA-ML model prediction. A horizontal dashed line marks the *JKR-like rubbery lower bound* ($\widehat{w}_{\mathrm{po}} = 5.50376$ obtained through (46)), which applies in the low-rate regime. Another dashed line indicates the *glassy upper bound* ($\widehat{w}_{\mathrm{po}} = 37.1203$ obtained through (43)), relevant at higher unloading rates ($\widehat{r}_u \gtrsim 10^3$).

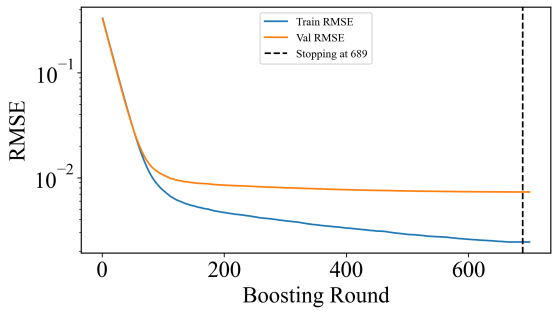

Figure A.8: XGboost learning curve

Appendix-X. Hyperparameter tuning

For XGBoost, we note that boosting algorithms can overfit if the number of boosting iterations (trees) is too large. To mitigate this, we employed a validation strategy. We held out a 15% validation set. During training, we performed a manual grid search over the learning rate (shrinkage parameter, λ) and tree depth (interaction depth, d). For each combination, we utilized the native `xgb.train` API with early stopping, monitoring the per-round RMSE on the validation set. Our plotting of train versus validation RMSE over boosting rounds empirically confirmed that validation error decreased, and then the boosting round stopped at 689, as it is shown for the PA-ML model in Figure A.8. Early stopping is a common technique to select the optimal number of trees in boosting to prevent overfitting [187, 188].

Regarding Random Forest, the dynamics of overfitting, particularly concerning the number of trees (ntree or B), differ significantly from boosting methods. Random Forests are inherently robust against overfitting as the number of trees increases. Unlike boosting, adding more trees to a random forest typically does not lead to overfitting; instead, the generalization error converges to a certain value, often reaching a plateau in performance. The primary reason for limiting the number of trees in RF is usually computational cost, not a risk of overfitting [187, 188]. The learning curve of Random Forest as the number of trees grows for PA-ML model is shown in Figure A.9.

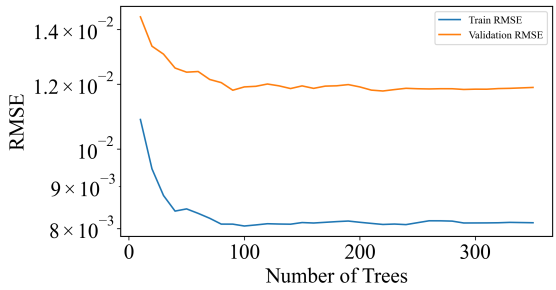

Figure A.9: Random forest learning curve